

SPECTROSCOPIC INTERROGATION OF METAL LIGATION AND
PHOTOACTIVE PROPERTIES IN METAL-ORGANIC FRAMEWORKS

By

Lauren Hanna

A dissertation submitted to the

Graduate School-Newark

Rutgers, the State University of New Jersey

In partial fulfillment of the requirements

For the degree of

Doctor of Philosophy

Graduate Program in Chemistry

Written under the direction of

Professor Jenny Lockard

And approved by

Newark, New Jersey

October, 2020

©2020

LAUREN HANNA

ALL RIGHTS RESERVED

ABSTRACT OF THE DISSERTATION

SPECTROSCOPIC INTERROGRATION OF METAL LIGATION AND
PHOTOACTIVE PROPERTIES IN METAL-ORGANIC FRAMEWORKS

By LAUREN HANNA

Dissertation Director:

Dr. Jenny Lockard

Metal-organic frameworks (MOFs), a class of crystalline hybrid materials, have been studied for a variety of applications ranging from gas sorption to photocatalysis. While the topic of most MOF research focuses on the application of the material, it is important to first understand the structure-function relationship. The adsorption-based functionalities of porous metal-organic framework (MOF) materials that lead to applications such as catalysis and gas separation rely on specific host–guest interactions often involving open metal sites within the nodes of the framework. These interactions are difficult to probe on the molecular level and consequently poorly understood. Spectroscopic methods provide the necessary molecular level information on local metal

coordination and electronic structure. In this thesis, steady-state and time resolved optical, x-ray, and vibrational spectroscopic methods are all used to gain molecular level insight, and sometimes a conjunction of techniques are needed to provide a comprehensive answer. Namely, valence-to-core X-ray emission spectroscopy has proven to be exceptionally sensitive to ligand identity, however, for a complete understanding of ligand identity and the nature of the interaction within a given framework, results were complimented with other spectroscopic methods such as Raman spectroscopy and X-ray absorption spectroscopy. Additionally, element specific techniques like X-ray spectroscopic methods, specifically X-ray transient absorption spectroscopy offer element specific excited state information that eludes assignment via convention methods. A brief summary of each chapter is provided below.

Chapter 1 Introduces relevant background information for research topics in this thesis. The overview begins with an introduction to metal-organic frameworks and their host-guest interactions, followed by an introduction to photoactivity in MOFs. Finally, the chapter ends with a summary of spectroscopic techniques used in this thesis, such as Raman spectroscopy, X-ray emission spectroscopy, X-ray absorption spectroscopy, Optical transient absorption spectroscopy, and X-ray transient absorption spectroscopy

Chapter 2 A series of trinuclear iron μ_3 -oxo-based MOFs were investigated under different metal-coordinating guest environments (water, pyridine, propylene, and guest-free) using a multipronged spectroscopy approach, including valence-to-core X-ray emission spectroscopy (vtc-XES) along with conventional XAS and vibrational

spectroscopy, in an effort to characterize their local metal site coordination environments, including ligand identity. Closely related iron μ_3 -oxo reference complexes with known coordination are characterized as well for comparison to evaluate the ligand diagnostic nature of the combined spectroscopy approach. Density functional theory calculations aid the vtc-XES band assignments and provide insights into the molecular orbital parentage of the vtc transitions. This series of MOFs and complexes illustrates the advantages and limitations of using this combination of complementary techniques for distinguishing subtle differences in framework metal node coordination environments.

Chapter 3 The long-lived excited state of a MOF with such vague optical properties, MIL-100(Fe), composed of Fe_3 - μ_3 -oxo clusters and trimesic acid linkers, was investigated using Fe K-edge X-ray transient absorption (XTA) spectroscopy to unambiguously determine its ligand-to-metal charge-transfer character. Spectra confirm the long-lived nature of the charge-separated excited state. Several trinuclear iron μ_3 -oxo carboxylate complexes, which model the trinuclear cores of the MOF structure, are measured for comparison using both steady-state X-ray absorption spectroscopy and XTA to further support this assignment and corresponding decay time. The MOF is prepared as a colloidal nanoparticle suspension for these measurements, so both its fabrication and particle size analysis are presented as well.

Chapter 4 The development of a synthetic procedure for MIL-125-NH₂ doped with different transition metals is discussed. The corresponding characterization of the doped MOFs using X-ray diffraction, X-ray absorption spectroscopy, and UV/VIS

Diffuse Reflectance provide structural insight including the geometry, coordination environment, and oxidation state of the heterometal.

Chapter 5 A new Fe-doped MOF is characterized using extended x-ray absorption fine structure (EXAFS) and XRD. The impact of the Fe-dopant on the ligand-to-cluster charge transfer (LCCT) in metal-organic framework MIL-125-NH₂ was examined using time resolved spectroscopic methods. While optical transient absorption spectroscopy reveals a long-lived excited state of the doped MOF compared to the undoped MOF, the assignment of the species was ambiguous. Therefore, Fe K-edge XTA revealed a transient Fe(II) species upon excitation into the LCCT. The long-lived participation of the Fe center on the excited state confirmed that the Fe dopant acts as a trap site, preventing charge recombination.

Dedicated to my family

For your unwavering support and love through this journey

ACKNOWLEDGEMENT

First and foremost, I would like to extend my deepest gratitude to my advisor, Dr. Lockard, for her endless support and patience. I have grown so much under your guidance. Thank you for everything you've taught me, both in academia and in life.

I would like to thank the members of my committee, Dr. Piotrowiak, Dr. Pavanello, and Dr. Sun for their guidance and support during my study.

I would like to thank the National Science Foundation for their support under Grant No. DMR-1455127.

I would like to thank my husband, Casey Hanna, for his constant support and love throughout this process. From you, I learned what the true meaning of unconditional support is.

I would like to thank all the Chemistry Department faculty members, all of which have provided me with endless help and guidance.

I would like to especially thank Dr. Pavel Kucheryavy who was an incredible role model. It was a gift to be able to learn from you.

I would like to thank my dear friend and groupmate, Nicole Lahanas for her level headedness and insight that helped guide me through even the darkest times. I could not have done this without you.

I would like to thank my fellow doctoral students and post-doctorals, most of whom helped me along the way and provided me with a sense of community while at Rutgers.

I would like to thank all the staff members who made every effort to help me through the years.

I would like to thank and honor my mother, Anne Noyes, the person who was the main pillar who pushed me to complete my doctoral degree; without her, I would not have strived to the level I did.

I would also like to thank the continued support from my family, James Noyes, Caitlyn Noyes, and Jim Noyes, who listened and supported me throughout this process.

Last, I would like to thank my family members, Tammy Hanna, Vernon Hanna, and Samantha Hanna, for providing me a safe place to land.

This thesis is partially based upon research conducted at C1 station at CHESS which is supported by the National Science Foundation and beamlines 11-IDD and 9-BM at the Advanced Photon Source, a U.S. Department of Energy (DOE) Office of Science User Facility operated for the DOE Office of Science by Argonne National Laboratory and Beamlines 6-BM and 8-ID of the National Synchrotron Light Source II, a U.S. Department of Energy (DOE) Office of Science User Facility operated for the DOE Office of Science by Brookhaven National Laboratory.

Chapter 2 of this dissertation is a version of the manuscript as it appears in *Journal of Chemical Physics*, 2019, 150(17), 174707.

Chapter 3 of this dissertation is a version of the manuscript as it appears in *Journal of Physical Chemistry C*, 2017, 121(25), 13570.

TABLE OF CONTENTS

ABSTRACT OF THE DISSERTATION	iii
DEDICATION	vii
ACKNOWLEDGEMENTS	viii
TABLE OF CONTENTS	x
LIST OF ABBREVIATIONS	xiii
LIST OF TABLES	xvi
LIST OF FIGURES	xvii
Chapter 1. Introduction	1
1. Metal-Organic Frameworks	1
1.2 MOF Applications	1
1.3 MOF Characterization: Conventional Techniques	6
1.4 Steady-State Electronically and Structurally Sensitive Spectroscopy Techniques	7
1.4.1 Raman Spectroscopy	8
1.4.2 UV-visible Diffuse Reflectance Spectroscopy	10
1.4.3 X-Ray Absorption Spectroscopy	11
1.4.4 X-Ray Emission Spectroscopy	14
1.5 Time-Resolved Electronically and Structurally Sensitive Spectroscopy Techniques	17
1.5.1 Optical Transient Absorption Spectroscopy	17
1.6 X-Ray Transient Absorption Spectroscopy	18
Chapter 2. Spectroscopic characterization of metal ligation in trinuclear iron- μ_3 -oxo-based complexes and metal-organic frameworks	27
2.1 Introduction	27
2.2 Experimental and Computational Methods	30
2.2.1 Materials and Synthesis	30
2.2.1.1 Materials	31
2.2.1.2 Synthesis	31
2.2.2 Characterization	31
2.2.3 Raman spectroscopy	32
2.2.4 X-ray absorption spectroscopy	33

2.2.5 X-ray emission spectroscopy	34
2.2.6 Computational methods	35
2.2.6.1 DFT Calculations	35
2.3 Results and Discussion	35
2.3.1 MOF guest molecule introduction and bulk characterization	36
2.3.1.1 Raman spectroscopy	38
2.3.1.2 X-ray absorption spectroscopy	42
2.3.1.3 X-ray emission spectroscopy	48
2.4 Conclusion	56
2.5 References	58
Chapter 3. Long-Lived Photoinduced Charge Separation in a Trinuclear Iron- μ_3 -oxo- based Metal–Organic Framework	65
3.1 Introduction.....	65
3.2 Experimental Methods	67
3.2.1 Materials and Synthesis	67
3.2.2 Characterization	69
3.2.3 Spectroscopic Methods	70
3.2.3.1 Optical Absorption Spectroscopy	70
3.2.3.2 Femtosecond Optical Transient Absorption Spectroscopy	70
3.2.3.3. X-ray Absorption Spectroscopy	71
3.2.3.4 X-ray Transient Absorption Spectroscopy	71
3.3 Results	73
3.3.1 MIL-100(Fe) Nanoparticle Synthesis and Characterization	73
3.3.1.1 Powder X-Ray Diffraction	74
3.3.1.2 Transmission Mode Scanning Electron Microscopy (STEM)	76
3.3.1.3 Dynamic Light Scattering (DLS)	77
3.3.2 Optical Absorption Spectroscopy	78
3.3.3 Ultrafast Optical Transient Absorption Spectroscopy	81
3.3.4 Steady-State X-ray Absorption Spectroscopy	82
3.3.4 X-ray Transient Absorption Spectroscopy	84
3.4 Discussion	88
3.5 References	93

Chapter 4: Synthetic methods and characterization of transition metal doped MIL-125-NH ₂ metal-organic frameworks.....	97
4.1 Introduction.....	97
4.2 Experimental Methods	102
4.2.1 Materials and Synthesis	102
4.2.1.1 Materials	102
4.2.1.1 Synthesis	102
4.2.2 Characterization and Methods	103
4.2.2.1 Characterization	103
4.2.2.2 X-ray absorption Spectroscopy	103
4.3 Results and Discussion	104
4.3.1 XRD	104
4.3.2 X-Ray Absorption Spectroscopy	108
4.3.3 Optical Electronic Absorption Spectroscopy	120
4.4 Conclusion	122
4.5 References	124
Chapter 5: Direct evidence for heterometal incorporation and its participation in the photoinduced charge separated excited state of MIL125-NH ₂	127
5.1 Introduction	127
5.2 Experimental Methods	130
5.2.1 Synthesis and Materials	130
5.2.1.1 Materials	130
5.2.1.2 Synthesis	130
5.2.2 Characterization	131
5.2.3 Optical Transient Absorption Spectroscopy	132
5.2.4 Steady State X-Ray Absorption Spectroscopy	132
5.2.5 X-Ray Transient Absorption Spectroscopy	133
5.3 Results and Discussion	134
5.3.1 Synthesis and Characterization	134
5.3.2 Optical Electronic Absorption Spectroscopy	135
5.3.3 Steady State X-ray Absorption Spectroscopy	137
5.3.4 Femtosecond Optical Transient Absorption Spectroscopy	142

5.3.5 Fe K-edge X-Ray Transient Absorption Spectroscopy	145
5.4 Conclusion	148
5.5 References	150

ABBREVIATIONS

Act	Activated
AS	As Synthesized
BDC	1,4-benzenedicarboxylic acid
BDC-NH ₂	2-aminobenzenedicarboxylic acid
CTMAB	Cetyltrimethylammoniumbromide
CUS	Coordinatively Unsaturated Site
DFT	Density Functional Theory
DLS	Dynamic Light Scattering
DR	Diffuse Reflectance
EXAFS	Extended X-ray Absorption Fine Structure
FWHM	Full Width Half Maximum
HOCO	Highest Occupied Crystal Orbital
HOMO	Highest Occupied Molecular Orbital
IR	Infrared

LCCT	Ligand-to-cluster charge transfer
LMCT	Ligand-to-metal charge transfer
LUCO	Lowest Unoccupied Crystal Orbital
LUMO	Lowest Unoccupied Molecular Orbital
MIL	Materials Institute Lavoisier
MOF	Metal-Organic Framework
NMR	Nuclear Magnetic Resonance
OA	Oleylamine
OTA	Optical Transient Absorption
Prop	Propylene
PXRD	Powder X-Ray Diffraction
Py	Pyridine
SBU	Secondary Building Units
SNR	Signal-to-Noise Ratio
SXRD	Single Crystal X-Ray Diffraction
TDDFT	Time-Dependent Density Functional Theory
TGA	Thermogravimetric Analysis
UV-vis	Ultraviolet-visible

vtc-XES	Valence-to-Core X-Ray Emission Spectroscopy
XANES	X-ray Absorption Near Edge Structure
XAS	X-ray Absorption Spectroscopy
XES	X-ray Emission Spectroscopy
XRD	X-ray Diffraction
XTA	X-Ray Transient Absorption
ZIF	Zeolitic imidazolate framework

LIST OF TABLES

Table 2.1 EXAFS Fitting Parameters and comparison with crystallographic data for Fe ₃ OBzPy	46
Table 2.2 EXAFS Fitting Parameters and comparison with crystallographic data for Fe ₃ OBz	47
Table 2.3 vtc-XES Error Analysis	56
Table 3.1 DLS Results for MIL-100(Fe)-OA	77
Table 3.2 DLS Results for MIL-100(Fe) treated with KF	77
Table 3.3 Summary of particle sized determined DLS, XRD, and STEM.	78
Table 3.4 OTA Exponential Lifetime Fitting Results for Fe ₃ O-BzPy at 530 nm	82
Table 5.1 EXAFS Fitting Parameters and comparison with crystallographic data for MIL-125-NH ₂ (Ti,Fe)	141
Table 5.2 Fitting Results of Optical Transient Absorption 585 nm kinetics	145
Table 5.3 Fitting Parameters for the XTA Kinetics monitored at 7.123 keV for MIL-125-NH ₂ (Ti,Fe)	148

LIST OF FIGURES

Figure 1.1 Schematic representation of construction, activation (solvent removal), and subsequent guest introduction to a MOF	2
Figure 1.2 Structures of four representative zeolites; faujasite or zeolites X, Y; zeolite ZSM-12; zeolite ZSM-5 or silicalite-1; zeolite Theta-1 or ZSM-22	4
Figure 1.3 Diagram of transitions probed in Raman and IR spectroscopy	10
Figure 1.4 Representative Mn K-edge XANES and EXAFS spectra	14
Figure 1.5 Fe K β -XES spectrum for [Fe(III)Cl ₄] ¹⁻	16
Figure 1.6 Schematic representation of the optical transient absorption spectroscopy experiment and an energy level diagram depicting some of the common transitions probed	18
Figure 1.7 XTA setup at Beamline 11ID-D, APS	19
Figure 2.1 MIL-100(Fe) structure showing activation and guest introduction and trinuclear iron reference complexes Fe ₃ OBz and Fe ₃ OBzPy	30
Figure 2.2 PXRD Pattern of MIL100(Fe) Simulated, MIL100(Fe), MIL100(Fe)-Act, and MIL100(Fe)-Py	37
Figure 2.3 FT-IR Spectra of (top): MIL100(Fe) and MIL100(Fe)-Py and (bottom): Fe ₃ OBz and Fe ₃ OBzPy	37
Figure 2.4 Raman spectra of (top) Fe ₃ OBz and Fe ₃ OBzPy and (bottom) MIL100(Fe) and MIL100Fe-Py	39
Figure 2.5 Raman spectra (obtained using 420 nm excitation through in situ measurement) highlighting the propylene modes	41
Figure 2.6 XANES spectra with magnified pre-edge regions (top) and EXAFS spectra (bottom) of reference complexes Fe ₃ OBz and Fe ₃ OBzPy, and MOFs MIL100(Fe), MIL100(Fe)-Py, MIL100(Fe)-Act, and MIL100(Fe)-Prop	43
Figure 2.7 XANES spectra and first derivative spectra of reference complexes Fe ₃ OBz and Fe ₃ OBzPy, and MOFs MIL100(Fe), MIL100(Fe)-Py, MIL100(Fe)-Act, and MIL100(Fe)-Prop	44
Figure 2.8 : Fe K-edge EXAFS spectra of Fe ₃ OBzPy and fit.....	46
Figure 2.9 Fe K-edge EXAFS spectra of Fe ₃ OBz and fit	47
Figure 2.10 Experimental and theoretical K β vtc-XES spectra of Fe ₃ OBz and Fe ₃ OBzPy, and MIL100(Fe) and MIL100(Fe)-Py	50
Figure 2.11 Energy level diagrams for Fe ₃ OBz and Fe ₃ OBzPy overlaid with the corresponding theoretical spectra	51

Figure 2.12 Calculated vtc-XES spectrum of MIL100(Fe) localized on each individual iron site to generate the average overall spectrum.....	52
Figure 2.13 Calculated vtc-XES spectrum of MIL100(Fe)Py localized on each individual iron site to generate the average overall spectrum.....	53
Figure 2.14 Experimental vtc-XES spectra of MIL100(Fe), MIL100(Fe)-Py, and MIL100(Fe)-Prop each overlaid with MIL100(Fe)-Act	55
Figure 3.1 Structure of MIL-100(Fe) and reference complexes	67
Figure 3.2 PXRD of MIL-100(Fe), Simulated, KF Treated, Oleylamine Treated, Oleylamine sample after XTA experiment	74
Figure 3.3 Simulated and experimental PXRD patterns for Fe ₃ O-BzPy reference complex	74
Figure 3.4 : FT-IR Spectra of MIL100(Fe) and MIL100(Fe)-Py and Fe ₃ OBz and Fe ₃ OBzPy	75
Figure 3.5 STEM Images of MIL-100(Fe)-KF and MIL-100(Fe)-OA	76
Figure 3.6 Transmission UV–vis absorption of MIL-100(Fe)-OA, Fe ₃ O-Bz, and Fe ₃ O-BzPy	79
Figure 3.7 Transmission UV/VIS spectra of a suspension of MIL-100(Fe)-OA in ethanol and MIL-100(Fe)-KF Treated	80
Figure 3.8 Diffuse reflectance spectra of MIL-100(Fe)-OA, Fe ₃ O-Bz, and Fe ₃ O-BzPy .	80
Figure 3.9 Diffuse Reflectance Spectra of Fe ₃ O-Ac and MVFe ₃ O-Ac	81
Figure 3.10 Optical transient absorption spectra collected at different time delays, up to 1 ns and kinetics probed at 530 nm of the Fe ₃ O-BzPy reference complex	82
Figure 3.11 Steady State XAS and derivative spectra of MIL-100(Fe) and reference Complexes Fe ₃ O-BzPy, Fe ₃ O-Bz, MVFe ₃ O-Ac, and Fe ₃ O-Ac	83
Figure 3.12 Steady-state XANES spectra of Fe ₃ O–Ac and MVFe ₃ O–Ac and “Pre-time zero” and “time zero” XTA spectra for MIL-100(Fe)-OA	84
Figure 3.13 “time-zero” and “pre-time zero” XTA spectra of MIL-100(Fe)-KF	85
Figure 3.14 “Time zero” XTA difference spectra of MIL-100(Fe)-OA and Fe ₃ O-BzPy.	85
Figure 3.15 XTA difference spectra obtained at multiple time delays for MIL100(Fe)-OA	86
Figure 3.16 XTA difference spectra obtained at multiple time delays for Fe ₃ O-BzPy ...	86

Figure 3.17 Sample stability assessment for XTA measurements: X-ray-induced changes	87
Figure 3.18 Sample stability assessment for XTA measurements: laser-induced changes	88
Figure 4.1 Structure of MIL-125-NH ₂ , highlighting the octameric core containing the dopant (V, Mn, Fe, or Cu).....	100
Figure 4.2 Powder X-ray diffraction of MIL-125 simulated (gray), MIL-125-NH ₂ (Ti) (black), MIL-125-NH ₂ (Ti,V) (green), MIL-125-NH ₂ (Ti,Mn) (navy), MIL-125-NH ₂ (Ti,Fe) (purple), and MIL-125-NH ₂ (Ti,Cu)	105
Figure 4.3 Powder X-ray diffraction of MIL-125 simulated, TiO ₂ anatase, TiO ₂ rutile, V ₂ O ₃ , and MIL-125-NH ₂ (Ti,V)	105
Figure 4.4 Powder X-ray diffraction of MIL-125 simulated, TiO ₂ anatase, TiO ₂ rutile, MnO, and MIL-125-NH ₂ (Ti,Mn)	106
Figure 4.5 Powder X-ray diffraction of MIL-125 simulated, TiO ₂ anatase, TiO ₂ rutile, Fe ₃ O ₄ , and MIL-125-NH ₂ (Ti,Fe)	106
Figure 4.6 Powder X-ray diffraction of MIL-125 simulated, TiO ₂ anatase, TiO ₂ rutile, CuO, and MIL-125-NH ₂ (Ti,Cu)	107
Figure 4.7 Powder X-ray diffraction of MIL-125 simulated, TiO ₂ anatase, TiO ₂ rutile, CuO, and CuCl ₂ soaked MIL-125-NH ₂	107
Figure 4.8 Powder X-ray diffraction of MIL-125 simulated, TiO ₂ anatase, TiO ₂ rutile, Fe ₂ O ₃ , and FeCl ₃ soaked MIL-125-NH ₂	108
Figure 4.9 Ti K-edge XAS of MIL-125-NH ₂ (Ti), TiO ₂ anatase, and TiO ₂ rutile	109
Figure 4.10 Experimental EXAFS of MIL-125-NH ₂ with calculated scattering paths plotted in R space.....	110
Figure 4.11 Ti K-edge XAS of MIL-125-NH ₂ , V-doped MIL-125-NH ₂ , Mn-doped MIL-125-NH ₂ , Fe-doped MIL-125-NH ₂ , and Cu-doped MIL-125-NH ₂	112
Figure 4.12 Ti K-edge EXAFS of MIL-125-NH ₂ , Mn-doped MIL-125-NH ₂ , Fe-doped MIL-125-NH ₂ , and Cu-doped MIL-125-NH ₂	113
Figure 4.13 Cu K-edge XANES and EXAFS plotted in R space of CuO, CuCl ₂ , Cu foil, MIL-125-NH ₂ (Ti,Cu), and CuCl ₂ soaked MIL-125-NH ₂	115
Figure 4.14 Fe K-edge XANES and EXAFS plotted in R space of Fe ₂ O ₃ , FeCl ₃ , Fe foil, MIL-125-NH ₂ (Ti,Fe), and FeCl ₃ soaked MIL-125-NH ₂	116
Figure 4.15 Mn K-edge XANES and EXAFS plotted in R space of MnO, MnCl ₂ , Mn foil, and MIL-125-NH ₂ (Ti,Mn)	117

Figure 4.16 V K-edge XANES and EXAFS plotted in R space of VCl ₃ , V foil, and MIL-125-NH ₂ (Ti,V)	118
Figure 4.17 Experimental EXAFS spectra plotted in R space of MIL-125-NH ₂ (Ti), MIL-125-NH ₂ (Ti,Mn), MIL-125-NH ₂ (Ti,Fe), and MIL-125-NH ₂ (Ti,Cu)	120
Figure 4.18 UV/VIS Diffuse Reflectance spectra of MIL-125-NH ₂ (Ti), 2-aminoterephthalic acid (gray), MIL-125-NH ₂ (Ti,V), MIL-125-NH ₂ (Ti,Mn), MIL-125-NH ₂ (Ti,Fe), and MIL-125-NH ₂ (Ti,Cu)	121
Figure 5.1 Structure of MIL-125-NH ₂ , highlighting the octameric core containing the Fe(III) dopant	130
Figure 5.2 PXRD of MIL-125 simulated, MIL-125-NH ₂ (Ti), MIL-125-NH ₂ (Ti,Fe) ..	135
Figure 5.3 UV/VIS Spectra of MIL-125-NH ₂ (Ti) and MIL-125-NH ₂ (Ti,Fe) suspended in DMF and 2-aminoterephthalic acid in CH ₃ CN	136
Figure 5.4 Diffuse reflectance spectra of 2-aminoterephthalic acid, MIL-125-NH ₂ (Ti) and MIL-125-NH ₂ (Ti,Fe)	137
Figure 5.5 Experimental Fe K-Edge XAS and EXAFS plotted in R space of MIL-125-NH ₂ (Ti,Fe), Fe ₂ O ₃ , FeCl ₃ , and Fe foil	138
Figure 5.6 Local coordination environment of MIL-NH ₂ (Ti,Fe)	139
Figure 5.7 MIL-125-NH ₂ (Ti,Fe) EXAFS and corresponding EXAFS fit with both magnitude and real spectrum	141
Figure 5.8 Optical transient absorption kinetics of the BDC-NH ₂ linker, MIL-125-NH ₂ (Ti), and MIL-125-NH ₂ (Ti,Fe) collected at 585 nm and the corresponding transient absorption spectra collected at pre-time zero and 1 ± 0.5 ps.	144
Figure 5.9 “laser on” and “laser off” Fe K-Edge XTA spectra of MIL-125-NH ₂ (Ti,Fe) and the difference spectra between the “laser off” and “laser on” spectra	146
Figure 5.10 Extended XTA Kinetics monitored at 7.123 keV of 1Fe/cluster doped MIL-125-NH ₂	147

CHAPTER 1: INTRODUCTION

Metal-organic frameworks (MOFs) are a class of materials that are permanently porous and crystalline in nature. Due to the tunability and variety of their structure, they have a variety of applications, ranging from gas adsorption, (photo-)catalysis, gas storage, and gas separation. However, for intelligent application of these materials, a strong fundamental understanding of the structure-function relationship of MOFs is needed. This thesis focuses on two main functions of MOFs, guest molecule adsorption at a thermally generated open metal site and visible light photoactivity. In Chapter 2, the ability to spectroscopically detect different guest species within a trinuclear Fe(III) μ_3 -oxo-based MOF is explored using valence-to-core X-ray emission and other complementary spectroscopy methods. Chapter 3 investigates the photoactivity of this framework and elucidates the nature of its exceptionally long excited state lifetime compared to an isolated reference complex. Chapter 4 introduces the synthesis and the characterization of a series of transition metal doped Ti-oxo cluster-based MOFs. Last, Chapter 5 presents a deeper investigation of the Fe-doped version of this MOF by revealing the nature and kinetics of the excited state using X-ray transient absorption spectroscopy (XTA) and the role of the Fe dopant in extending the excited state lifetime is explored.

1.1 Metal-Organic Frameworks

1.1.1 MOF Applications

Metal-Organic Frameworks (MOFs) are porous hybrid materials composed of self-assembled metal ions or clusters connected through coordination bonds with organic or organometallic linkers.¹⁻⁵ As illustrated in Figure 1.1, the ordered arrangement of these

components is dictated by the solvothermal synthetic conditions and the identity, stoichiometry and functionalization of the organic linkers. After framework formation, crystallinity is retained upon solvent removal, typically through a mild thermal activation step. This hallmark of MOF materials renders the porous architectures accessible to other potential guest species during subsequent treatment. Unlike zeolites, whose framework structures are limited by metal coordination geometries and small ambidentate linker ions, MOFs offer a large variety of microporous architectures through the choice and functionalization of the organic linkers. Moreover, some frameworks are amenable to post-synthetic modification as another handle to further alter the node or linker sites. The resulting diversity in chemical makeup and tunable pore size and shape of MOFs can be exploited for potential adsorption-based applications such as gas separation and storage,⁶⁻¹³ heterogeneous catalysis¹⁴⁻¹⁶ and photocatalysis,¹⁷⁻¹⁹ electrochemical- and optical-based sensing²⁰⁻²⁵ and others.^{3-4, 26-28}

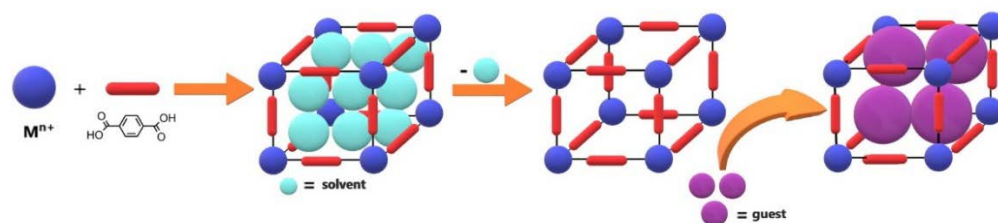


Figure 1.1 Schematic representation of construction, activation (solvent removal), and subsequent guest introduction to a MOF. Terephthalic acid linker example shown.

A MOF's ability to selective adsorb guest species can be influenced by various mechanisms. Specifically, guest species can be adsorbed through an empty pore, an unoccupied metal site, or through interactions with the linker. Selective uptake of species through an activated, or evacuated pore, mainly occurs due to a kinetic or size and shape

limited mechanism. The molecular sieving effect arises when molecules of a certain size and shape enter the pores of the MOF, whereas other species of different size and shape are prohibited. The molecular sieving effect can be achieved by controlling pore size, typically by modification of the steric hindrance or length of the linker.²⁹ Kinetic separation, different from the molecular sieving effect, is based on limiting pore interpenetration by diffusion.¹⁰ The rate of diffusion depends greatly on the size and shape properties of the adsorbate and the pore size of the MOF. However, one of the most widely studied methods of guest incorporation within a framework occurs directly at the metal site. Stable and rigid metal-organic frameworks can generate coordinatively unsaturated sites (CUS) removal of labile terminally bound solvent molecules by vacuum assisted heating, also known as activation. Typically, the CUS is located at the metal node, but there has been some instances of incorporating unsaturated metal sites at the linker.³⁰

Another ubiquitous application of MOFs is for their photocatalytic activity. The use of MOFs for photoactive applications was inspired by the disadvantages faced by conventional photoactive inorganic semiconductors. Photocatalysis is an ever-growing field of research, fueled by the world's need for greener and more sustainable sources of energy. The term photocatalysis, in the field of semiconductors, refers to the acceleration of a chemical reaction as a result of photocatalyst absorbing light with the appropriate energy to overcome the band gap between the conduction and valence band. Ultimately, this process results in photo-inducing the separation of an electron and hole³¹. The use of semiconductor oxides as photocatalysts can be traced by to the twentieth century, however, the true origination is still unknown. One notable experiment was conducted by

Fujishima and Honda, photoelectrolyzing water with a TiO_2 anode against a platinum cathode³¹⁻³³. These early findings sparked the cutting-edge research of the use of semiconductors for photocatalysis.

Of the studied semiconductor-based photocatalysts, TiO_2 was the most promising due to its low toxicity, stability, and relatively high quantum yield upon charge separation³⁴.

However, despite the many documented uses of TiO_2 as a photocatalyst³⁵, the semiconductor suffers from a few limitations. One of the most detrimental disadvantages for implementation is its large band gap, which is approximately 3.2 eV for anatase TiO_2 .

This limits the application of TiO_2 wavelengths less than 400 nm, therefore absorbing only about 5% of natural light³⁶. This realization has shifted the focus of the research in

the past decade to modifying TiO_2 to absorb more visible light. To improve the photocatalytic activity, several approaches have been researched, some of the most notable are doping with metals or non-metals or dye sensitization³⁶.

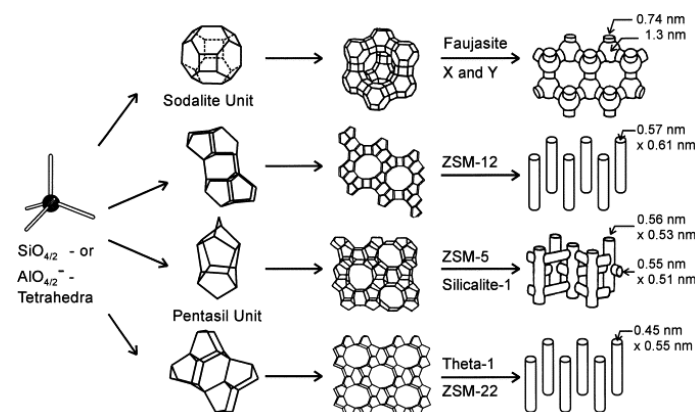


Figure 1.2 Structures of four representative zeolites; faujasite or zeolites X, Y; zeolite ZSM-12; zeolite ZSM-5 or silicalite-1; zeolite Theta-1 or ZSM-22³⁷

Parallel to TiO_2 research, porous solid-state materials have gained attention for their potential application as photocatalysts. Increasing the dimensionality from 2D to 3D of

the photocatalyst allowed for confinement of the intermediate within the pores, therefore, zeolites were some of the first 3D, porous materials to be investigated for their application as potential photocatalysts. Shown in Figure 1.3, zeolites are aluminosilicates with a porous, three-dimensional structure³⁴. Due to the elemental composition of zeolites, they are invisible to UV and visible light. However, incorporation of chromophores inside their pores allows photochemical reactions to take place in a confined manner¹⁸.

While zeolites presented an improvement over molecular-based photocatalysts, there still was a need for a more photo-responsive material. Therefore, application of MOFs as photocatalysts were a logical next progression of research in implementing porous, 3D materials for photocatalysis. Unlike zeolites, MOFs have more versatility in the choice of linker and metal node making these materials capable of absorbing UV and visible light. In MOFs, the most common linkers are aromatic carboxylates which serve as the antenna for absorbing photons¹⁸. A charge-separated state can be induced by linker excitation, generating a charge transfer between the linker and metal cluster, known as a linker-to-cluster charge transfer (LCCT). One ongoing debated topic has been whether MOFs can be labeled as semiconductors or insulators. Inorganic semiconductors are typically characterized as having delocalized orbitals, allowing for a band-like treatment of their orbitals. In the literature, the photo-conductivity of MOFs has not been regularly reported or reported with poor mobilities, compared to conjugated polymers which typically have a charge mobility on the order of $10^{-3} \text{ cm}^2 \text{ V}^{-1} \text{ s}^{-1}$ or higher³⁸⁻³⁹. Due to the fact the clusters and linkers are too far apart to allow for electron hopping, and the

spacing between linkers is too great for efficient orbital overlap, MOFs can be widely categorized as insulators⁴⁰.

Despite MOFs being classified as insulators, the optical responsiveness can be tuned by modification at the linker or metal node sites. It is highly desirable to have organic linkers that absorb in the visible region because one targeted electronic transition for photocatalytic materials is the ligand-to-metal charge transfer (LMCT). Additionally, the porous nature of MOFs make them ideal photocatalysts. Just as the metal nodes and linkers can serve as photocatalytic sites, the pores can be another center of photoredox activity. A guest species of a specific size can be encapsulated into the pores of the MOF and due to the proximity of the substrate and MOF surface, energy and electron transfer can occur⁴¹. Therefore, unlike traditional (nonporous) semiconductor photocatalysts, MOFs do not have the requirement of long-range charge mobility due to ability to facilitate a close range photocatalyst-substrate interaction. Additionally, the size requirement of the substrate, in order to fit inside the pore, also creates a size-selectivity of the MOF photocatalyst.

1.2 MOF Characterization: Conventional Techniques

Conventional MOF characterization techniques probe bulk properties, such as average particle size, surface area, pore size, and long range order. Specifically, long-range order is typically measured using X-ray diffraction (XRD), either by single crystal XRD (SXRD) or powder XRD (PXRD). Of the diffraction techniques, SXRD is the most informative for MOFs. Structure refinement can provide a wealth of knowledge, such as structure identification, determination of unit cell, crystallinity, and even presence and loss of guest species within the MOF.⁴²⁻⁴⁴ However, SXRD is not always possible

because preparing quality single crystals can be incredibly difficult to prepare in some instances. Even more challenging is obtaining a single crystal after thermal or guest treatment of the MOF because treatment may affect the overall crystallinity of the sample. As a result, powder X-ray diffraction (PXRD) is a viable alternative to SXRD when only microcrystalline powder materials are available. PXRD can provide similar structural information on the long range order and phase of a MOF.⁴⁵

The thermal stability of a MOF can be assessed using a technique known as Thermogravimetric Analysis (TGA). A thermogravimetric analyzer, or the instrument in which TGA is conducted on, measures the mass of the sample as the temperature is increased as a function of time. For MOF samples, this method can provide valuable information about the stability of the framework, as well as, changes in mass due to loss of guest or solvent molecules.⁴⁶ The loss of mass can therefore be correlated to the porosity of the MOF. This serves as a complimentary method to gas isotherm, in which the volume of gas uptake in an activated, or evacuated MOF, is recorded as a function of gas pressure. The accessible pore volume and surface area of the activated MOF, can then be calculated.⁴³

1.3 Steady-State Electronically and Structurally Sensitive Spectroscopy Techniques

The above techniques provide information on MOF long range order and porosity, however, these methods do not provide local molecular level coordination or electronic structure information. Spectroscopy methods, on the other hand can provide this level of detail. Infrared (IR) spectroscopy, methods for example, involving the direct transition between vibrational energy levels induced by the absorption of infrared light, can give qualitative insight on dipole allowed vibrational modes within a MOF. IR spectroscopy is

ubiquitous as a general characterization method for molecules and materials⁴⁷⁻⁴⁸ The observation of distinctive mode frequencies is often used to identify the presence of certain functional groups, however, due to congested spectra and subtle shifts observed between similarly coordinating atoms, this method is not useful for applications such as unambiguous guest species identification.

Solid state NMR can be useful and has been used for some MOF materials⁴⁹⁻⁵¹. However, it is incompatible with many systems due to the presence of paramagnetic cores. Given this, many other techniques have been proven to be structurally and electronically sensitive to changes in the MOF environment due to guest introduction, such as Raman spectroscopy, X-ray absorption and emission spectroscopy, and UV-visible diffuse reflectance spectroscopy.

1.3.1 Raman Spectroscopy

Raman spectroscopy involves detection of photons that are inelastically scattered by the sample upon irradiation with single frequency laser light whose energy is typically much higher than that of a direct vibrational transition (usually in the visible to NIR energy range).⁵² Vibrational modes that produce a change in polarizability of the molecule or material are Raman active. Raman scattering intensity, I_R , is directly proportional to the square of the induced dipole moment, μ_{ind} , which in turn depends on both the perturbing electric field strength, E and the polarizability, α associated with a given vibration. This overall governing relationship can be expressed by the follow equations

$$\mu_{ind} = \alpha E \quad (1)$$

$$I_R^{1/2} \propto [\alpha]_{v,v'} \equiv \langle v' | \alpha | v \rangle \propto \left(\frac{\delta \alpha}{\delta Q} \right)_0 \quad (2)$$

where $[\alpha]_{v,v'}$ is the polarization transition moment and $(\delta\alpha/\delta Q)_0$ represents the change in polarizability due to vibrational mode, Q. The ability to collect high resolution vibrational spectra that extend into the low frequency range is an advantage over traditional FTIR spectroscopy for some systems. Raman spectroscopy is especially useful for the study of metal containing materials due to the facile screening of lower frequency modes, such as metal-ligand stretches, that are sensitive to local metal coordination environment. Linker-localized mode changes can reveal participation of the organic ligand under various host-guest environments and low frequency lattice vibrations can help establish the role of MOF flexibility. Moreover, when the energy of excitation is closely matched with that of either a surface plasmon band or an electronic transition within the material, vibrational modes can experience large intensity enhancements. These resonance effects can be exploited for purposes ranging from simple signal amplification for measurement of low concentration materials to deeper level electronic structure interrogations.

Raman spectroscopy has been applied to many MOF systems for characterization of host-guest interactions⁵³⁻⁷⁸. Since its early applications in exploring gas adsorption mechanisms in MOFs,⁷⁹ Raman spectroscopy continues to provide in depth structural information on MOF materials and their derivatives under a range of host-guest conditions and external stimuli. These insights can be obtained through both *ex situ* and *in situ* means and are often complemented by IR spectroscopy characterization.

This spectroscopic method has been proven to be a useful technique in MOF research. Specifically, its utility has been in identifying guest species within a framework, while also revealing structural implications due to the presence of the guest. Some of the early Raman spectroscopy studies involved interrogation of MOFs upon activation or

removal of labile solvent molecules within the pores occupying metal node coordination sites or bound through interaction with linker functionality.^{56, 67, 71} Gas adsorption processes, in particular those involving carbon dioxide, comprise an important application area for MOFs and have been explored extensively by Raman spectroscopy.^{55, 59-65, 68, 74, 77}

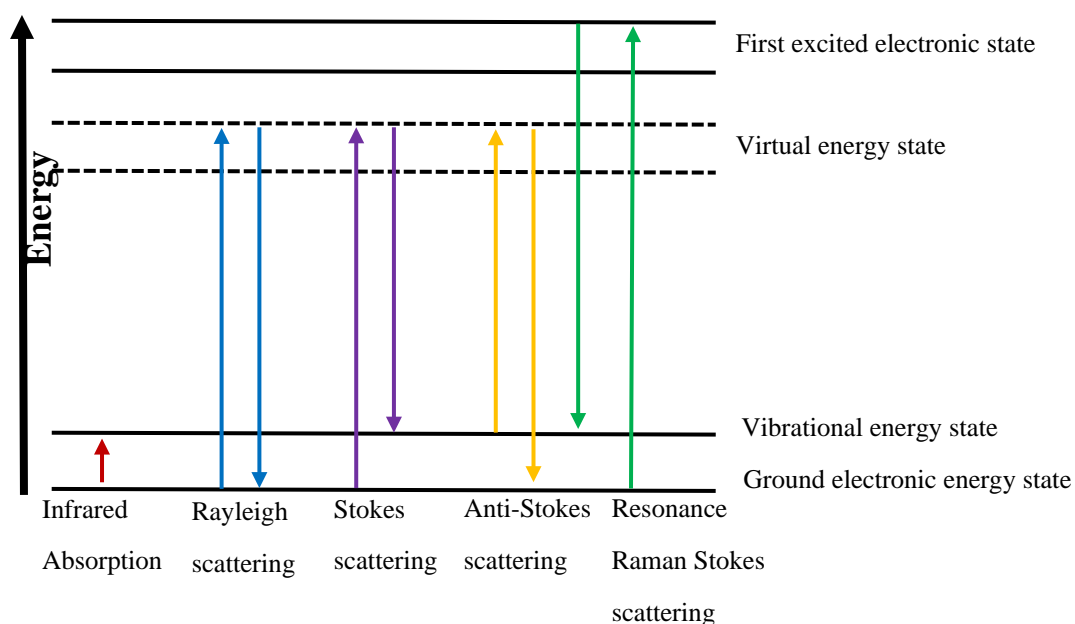


Figure 1.3 Diagram of transitions probed in Raman and IR spectroscopy

1.3.2 UV-visible Diffuse Reflectance Spectroscopy

Optical electronic absorption spectroscopy probes ground to excited state valence electron transitions induced by the absorption of UV-visible-NIR light and therefore offers a direct means of probing the electronic energy levels and bonding characteristics of molecules and materials.⁸⁰⁻⁸¹ Transition metal-based complexes and coordination polymers (including MOFs) typically absorb in a conveniently accessible optical energy

range. Moreover, an established theoretical framework based on ligand field interactions exists to interpret their spectra.

As is common for many solid state materials, diffuse reflectance (DR) methods⁸¹⁻⁸² are usually employed to measure ground state absorption spectra of MOF systems. In analogy to optical transmission methods, where the transmittance, or ratio of intensities of transmitted to incident light, is measured, DR involves the measurement of remittance, R_∞ , or the ratio of reflected to incident light. (the ∞ subscript here denotes effectively “infinite” sample thickness.) Plotting $\log(1/R_\infty)$ versus incident photon energy yields “apparent” absorption spectra. Like Beers’ law in transmission spectroscopy, the Kubulka-Munk function linearly relates concentration with the reflectance values of a diffusely reflecting sample:

$$F(R_\infty) = \frac{(1-R_\infty)^2}{2R_\infty} = \frac{2.303\epsilon C}{S} \quad (3)$$

where ϵ is the absorptivity, C is the concentration and S is two times the scattering coefficient. Since S is not always known or easily measured and analyte concentration is difficult to define for extended solid state materials, DR spectra are usually expressed in terms of the remittance using so called Kubelka-Munk units $[(1 - R_\infty)^2/2R_\infty]$.

1.3.3 X-Ray Absorption Spectroscopy

X-ray absorption spectroscopy (XAS) involves monitoring specific core electron excitation processes.⁸³⁻⁸⁸ Each element has distinct ionization energies associated with the removal of the different core electrons, giving rise to characteristic absorption edges. The hard X-ray edges are typically divided into two main regions; the X-ray Absorption Near

Edge Structure (XANES) and the Extended X-ray Absorption Fine Structure (EXAFS) regions. The XANES region is characterized by a rising edge that shifts in energy due to screening effects that depend on the valence electrons and therefore provides information on the absorbing element's oxidation state. Pre-edge features arising from formally dipole forbidden bound transitions reflect coordination geometry through their relative energy and intensities. The EXAFS region contains oscillating intensity features associated with the ejected core electron and its interaction with the surroundings, after having absorbed sufficient photon energy to overcome its ionization energy. The interference of the photoelectron with the electron density of the neighboring atoms leads to constructive or destructive interference depending on the incident photon energy. These oscillations can be interpreted to provide information on the type and distance of the nearest neighboring atoms in the immediate vicinity (typically $< 4\text{\AA}$), which in turn can be used to understand the local structure of the absorbing atom.

The theoretical framework for this spectroscopy method is well established. The EXAFS oscillations well above the absorption edge, defined as $\chi(E)$, are extracted by removing the background and normalizing to the edge jump according to:

$$\chi(E) = \frac{\mu(E) - \mu_0(E)}{\Delta\mu_0(E)} \quad (5)$$

where $\mu(E)$ is the measured absorption coefficient, $\mu_0(E)$ is the smooth background function associated with adsorption by an isolated atom and $\Delta\mu_0(E)$ is the measured absorption edge jump. The X-ray energy of the photoelectron is usually converted to wavenumber, k with units of $1/\text{distance}$ according to:

$$k = \sqrt{\frac{2m_e(E - E_0)}{\hbar^2}} \quad (6)$$

where m_e is the electron mass and E_0 is the absorption edge energy. The set of frequencies contributing to the oscillations in $\chi(k)$ arise from the different neighboring coordination shells. These contributions can be described, parameterized and modeled according to the EXAFS equation:

$$\chi(k) = \sum_j \frac{N_j f_j(k) e^{-2k^2 \sigma_j^2}}{k R_j^2} \sin[2k R_j + \delta_j(k)] \quad (7)$$

where $f_j(k)$ and $\delta_j(k)$ are the scattering amplitude and phase shift, respectively, associated with neighboring atoms in shell j , N_j is the degeneracy of the scattering path, R_j is the scattering distance, and σ_j^2 is its disorder. Like the other spectroscopic methods, XAS is compatible with both solid state sample formats and the introduction of various *in situ* sample environments. Data are collected in either a transmission mode setup using ion chamber detectors or total fluorescence yield using a range of X-ray fluorescence detectors depending on various factors such as absorbing element concentration.

The interpretation of both the XANES and EXAFS spectral regions allows the simultaneous evaluation of element specific metal oxidation state, coordination geometry and short range distance information about the absorbing atom. The method is also amenable to *in situ* measurements of solid state materials under a variety of gas or solution environments. These characteristics make XAS ideally suited for probing specific sites (eg metal sites at node or linker positions) within the frameworks. Unsurprisingly then, the use

of XAS techniques to characterize MOF materials and their response to external stimuli and host-guest environment has exploded over the last decade⁸⁹⁻⁹².

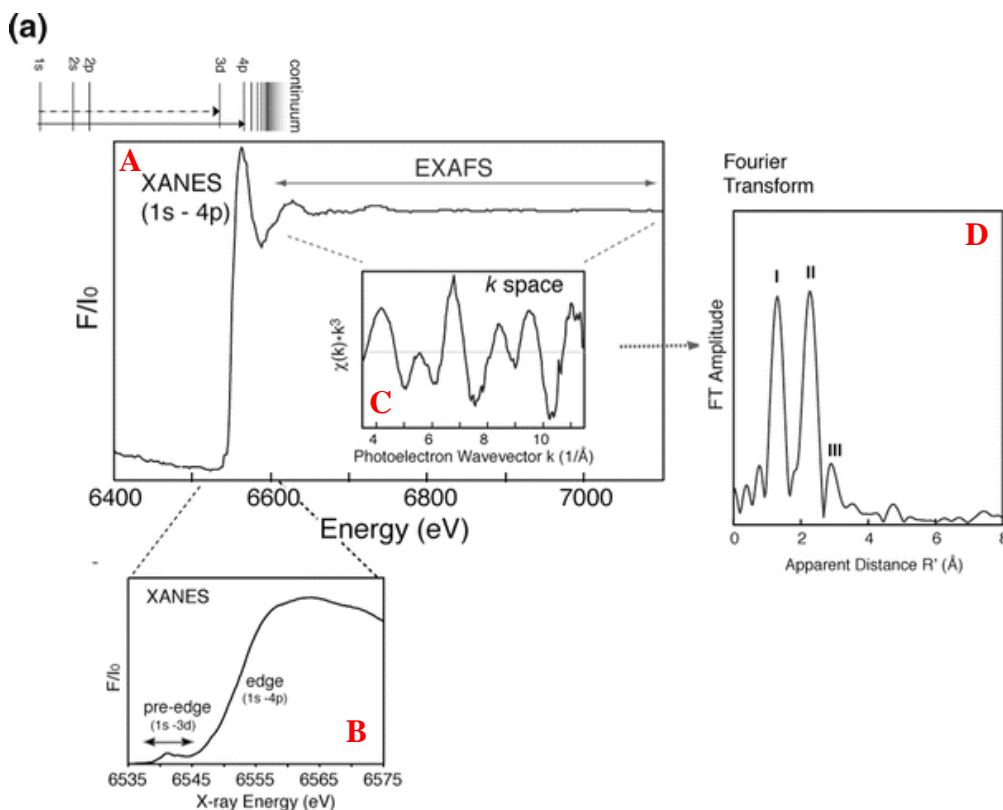


Figure 1.4 The Mn K-edge XANES and EXAFS spectra. A: the X-ray absorption spectra showing the XANES and EXAFS regions of the spectrum. The energy levels are indicated at the top. B: Mn K-edge XANES and C: the k -space EXAFS spectrum. D: The Fourier transform of the k -space EXAFS data⁹³.

1.3.4 X-Ray Emission Spectroscopy

X-ray emission spectroscopy (XES) measures the radiative process of filling the electron core hole, created through an X-ray absorption event, with a higher orbital electron. Like the X-ray absorption edges with which they are associated, X-ray emission lines are element specific. Furthermore, while XAS probes unfilled orbitals through core

electron transitions, XES provides information about the occupied orbitals of the absorbing element. The theoretical and experimental frameworks of XES methods are well established. This thesis focuses on third row transition metal K-edge emission lines. XES associated with these edges is also amenable to measuring solid state materials under a variety of gas or solution environments since hard X-rays (both exciting and emitted) are involved. Briefly, while $K\alpha$ emission involves $2p \rightarrow 1s$ transitions, $K\beta$ main line X-ray emission, which is typically separated by several hundred electron volts, is associated with the $3p \rightarrow 1s$ transition. For the latter, the exchange interaction between the $3p$ core hole and partially filled $3d$ orbitals in the final state results in two main features, $K\beta_{1,3}$ and $K\beta'$, which are sensitive to the number of unpaired electrons and therefore the spin and oxidation state of the absorbing metal. In general, a decrease in $K\beta'$ intensity and in energy splitting between the two features occurs with reduced spin at the metal. When the decay of valence orbital electrons (typically $3d$ mixed with $3p$ character) is involved, their participation in metal bonding interactions through ligand ns and np orbital mixing renders the resulting $K\beta$ satellite features, denoted $K\beta_{2,5}$ and $K\beta''$, exceptionally sensitive to the coordinated ligand environment.

XES can be measured with either non-resonant or resonant X-rays used to generate the initial core hole. In “non-resonant” XES, the excitation X-ray energy used to induce the core electron transitions is well above the Fermi level and the resulting emission lines described above are independent of this incident photon energy. While still in the early stages of application to MOFs, several XES-based studies on these materials have recently been reported. One notable use of XES is for ligand identification, even for similar coordinating atoms. DeBeer, et. al. used vtc-XES in conjunction with DFT

calculations to identify coordinating atoms in iron complexes. Experimentally, two ferrous, high spin octahedrally coordinated complexes show significant differences in the $K\beta_{2,5}$ feature despite the coordination environments being very similar. Upon closer examination using DFT calculations to confirm the orbital parentage of the complexes, the authors were able to assign the underlying transitions that contribute intensity and shape of the $K\beta_{2,5}$ region⁹⁴. This highlighted the sensitivity of vtc-XES for ligand identification, even for like coordinating atoms.

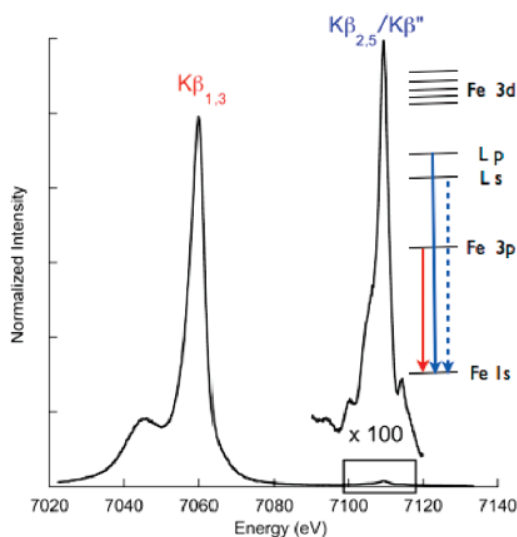


Figure 1.5 Fe $K\beta$ -XES spectrum for $[\text{Fe(III)Cl}_4]^{1-}$. The box highlights the valence to core region of the spectrum. The energy level diagram shows the transitions involved in the $K\beta_{1,3}$ and vtc-XES regions.⁹³

1.4 Time-Resolved Electronically and Structurally Sensitive Spectroscopy

Techniques

1.4.1 Optical Transient Absorption Spectroscopy

Optical transient absorption (OTA) spectroscopy techniques comprise a set of pump-probe methods used to gain information on excited state electronic structure and dynamics.⁹⁵⁻⁹⁷ In general, these methods entail promoting some fraction of the molecules or material being measured to an electronically excited state via an excitation (or pump) pulse followed by subsequent exposure to a relatively weak narrow or broadband probe pulse after some relative time delay, τ . Depending on the target time range of the experiment, pulsed light sources for these measurements vary from flash lamps to femtosecond laser systems with repetition rates ranging from single shot to MHz. Detecting the transmitted probe in the presence and absence of the pump pulse is processed as a difference absorption signal (ΔA). The different signal is generated at each time delay to produce a ΔA profile as a function of τ (for two color experiments), ie $\Delta A(\tau)$ or τ and wavelength λ , i.e., $\Delta A(\lambda, \tau)$, for broadband probe detection. The time resolution of this transient technique can range from sub-100fs to microseconds or longer and is primarily dictated by the pump and probe pulse durations. OTA can be collected via diffuse reflectance or transmission mode, with the latter being the more common format. In this case, for solid state materials such as MOFs, polymer matrices, liquid suspensions of nanoparticle samples or thin films are commonly used to minimize the contributions of elastic scattering to the signal.

Optical transient absorption spectroscopy has been used in the literature to investigate the nature of an excited state within a MOF. One study detected a long lived

photogenerated species within an Fe(III)-based MOF, MIL-88B. Monitoring the spectrum and the different kinetic traces indicated a long-lived ground state bleach assigned to a delayed charge recombination due to the trapping of holes upon excitation into the LMCT band. The authors were able to conclude that the presence of the long-lived species confirms that the metal clusters in the MOF are electronically connected to each other allowing for charge migration among them ⁹⁸.

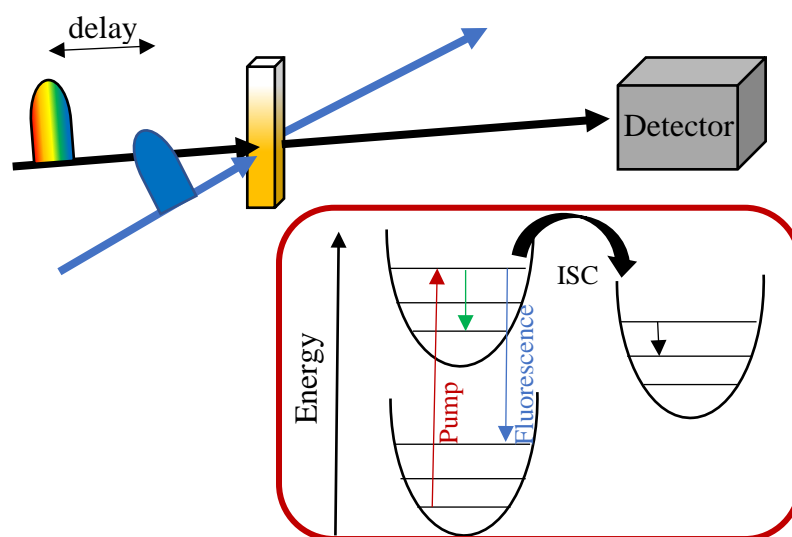


Figure 1.6 Schematic representation of the optical transient absorption spectroscopy experiment and an energy level diagram depicting some of the common transitions probed.

1.5 X-Ray Transient Absorption Spectroscopy

For many photoactive MOF systems, it is often desirable to probe the transient changes in electronic structure and coordination environment of the metal sites following optical photo-excitation that commonly involves some charge transfer event. In many cases, where

OTA characterization is insufficient or inconclusive due to a lack of definitive spectral signatures, these changes can be probed by complementary synchrotron X-ray transient absorption (XTA) spectroscopy.⁹⁹⁻¹⁰⁰ As shown in Figure 1.9, this element specific technique involves synchronized laser-pump X-ray probe measurements to track excited-state geometric and electronic changes of metal-based systems in the picosecond to nanosecond time domain. Having become an important tool for investigating the photochemistry of several types of, primarily molecular, metal-based complexes,¹⁰¹⁻¹⁰³ XTA has recently been applied to several MOF systems as well.¹⁰⁴⁻¹⁰⁷

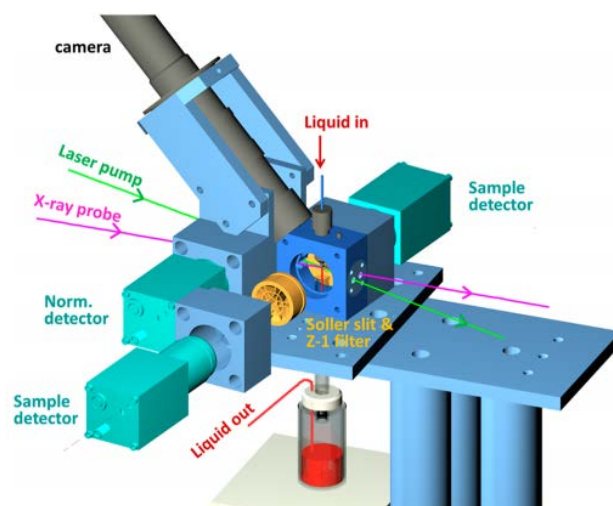


Figure 1.7 XTA setup at Beamline 11ID-D, APS¹⁰¹.

1.6 References

1. Furukawa, H.; Cordova, K. E.; O’Keeffe, M.; Yaghi, O. M., The Chemistry and Applications of Metal–Organic Frameworks. *Science* **2013**, *341* (6149), 1230444.
2. Kole, G. K.; Vittal, J. J., Solid-state reactivity and structural transformations involving coordination polymers. *Chemical Society Reviews* **2013**, *42* (4), 1755-1775.
3. Foo, M. L.; Matsuda, R.; Kitagawa, S., Functional Hybrid Porous Coordination Polymers. *Chemistry of Materials* **2014**, *26* (1), 310-322.
4. Wang, C.; Liu, D.; Lin, W., Metal–Organic Frameworks as A Tunable Platform for Designing Functional Molecular Materials. *Journal of the American Chemical Society* **2013**, *135* (36), 13222-13234.
5. Yuan, S.; Feng, L.; Wang, K.; Pang, J.; Bosch, M.; Lollar, C.; Sun, Y.; Qin, J.; Yang, X.; Zhang, P.; Wang, Q.; Zou, L.; Zhang, Y.; Zhang, L.; Fang, Y.; Li, J.; Zhou, H.-C., Stable Metal–Organic Frameworks: Design, Synthesis, and Applications. *Advanced Materials* **2018**, *30* (37), 1704303.
6. Yang, X.; Xu, Q., Bimetallic Metal–Organic Frameworks for Gas Storage and Separation. *Crystal Growth & Design* **2017**, *17* (4), 1450-1455.
7. Sumida, K.; Rogow, D. L.; Mason, J. A.; McDonald, T. M.; Bloch, E. D.; Herm, Z. R.; Bae, T.-H.; Long, J. R., Carbon Dioxide Capture in Metal–Organic Frameworks. *Chemical Reviews* **2012**, *112* (2), 724-781.
8. Li, J.-R.; Ma, Y.; McCarthy, M. C.; Sculley, J.; Yu, J.; Jeong, H.-K.; Balbuena, P. B.; Zhou, H.-C., Carbon dioxide capture-related gas adsorption and separation in metal-organic frameworks. *Coordination Chemistry Reviews* **2011**, *255* (15–16), 1791-1823.
9. Murray, L. J.; Dinca, M.; Long, J. R., Hydrogen Storage in Metal–Organic Frameworks. *Chemical Society Reviews* **2009**, *38* (5), 1294-1314.
10. Li, J.-R.; Kuppler, R. J.; Zhou, H.-C., Selective gas adsorption and separation in metal–organic frameworks. *Chemical Society Reviews* **2009**, *38* (5), 1477-1504.
11. Zhao, X.; Wang, Y.; Li, D.-S.; Bu, X.; Feng, P., Metal–Organic Frameworks for Separation. *Advanced Materials* **2018**, *30* (37), 1705189.
12. Shekha, O.; Chernikova, V.; Belmabkhout, Y.; Eddaoudi, M., Metal–Organic Framework Membranes: From Fabrication to Gas Separation. *Crystals* **2018**, *8* (11).
13. Wang, H.; Li, J., General strategies for effective capture and separation of noble gases by metal–organic frameworks. *Dalton Transactions* **2018**, *47* (12), 4027-4031.
14. Drake, T.; Ji, P.; Lin, W., Site Isolation in Metal–Organic Frameworks Enables Novel Transition Metal Catalysis. *Accounts of Chemical Research* **2018**, *51* (9), 2129-2138.
15. Wu, C.-D.; Zhao, M., Incorporation of Molecular Catalysts in Metal–Organic Frameworks for Highly Efficient Heterogeneous Catalysis. *Advanced Materials* **2017**, *29* (14), 1605446.
16. Dhakshinamoorthy, A.; Asiri Abdullah, M.; Garcia, H., Metal–Organic Frameworks as Catalysts for Oxidation Reactions. *Chemistry – A European Journal* **2016**, *22* (24), 8012-8024.
17. Zhang, T.; Lin, W., Metal–Organic Frameworks for Artificial Photosynthesis and Photocatalysis. *Chemical Society Reviews* **2014**, 5982-5993.

18. Dhakshinamoorthy, A.; Asiri, A. M.; García, H., Metal–Organic Framework (MOF) Compounds: Photocatalysts for Redox Reactions and Solar Fuel Production. *Angewandte Chemie International Edition* **2016**, 55 (18), 5414-5445.
19. Zhang, T.; Jin, Y.; Shi, Y.; Li, M.; Li, J.; Duan, C., Modulating photoelectronic performance of metal–organic frameworks for premium photocatalysis. *Coordination Chemistry Reviews* **2019**, 380, 201-229.
20. Cui, Y.; Yue, Y.; Qian, G.; Chen, B., Luminescent Functional Metal–Organic Frameworks. *Chemical Reviews* **2012**, 112 (2), 1126.
21. Hu, Z.; Deibert, B. J.; Li, J., Luminescent metal-organic frameworks for chemical sensing and explosive detection. *Chemical Society Reviews* **2014**, 43 (16), 5815-5840.
22. Fang, X.; Zong, B.; Mao, S., Metal–Organic Framework-Based Sensors for Environmental Contaminant Sensing. *Nano-Micro Letters* **2018**, 10 (4), 64.
23. Dolgoplova, E. A.; Rice, A. M.; Martin, C. R.; Shustova, N. B., Photochemistry and photophysics of MOFs: steps towards MOF-based sensing enhancements. *Chemical Society Reviews* **2018**, 47 (13), 4710-4728.
24. Zhang, Y.; Yuan, S.; Day, G.; Wang, X.; Yang, X.; Zhou, H.-C., Luminescent sensors based on metal-organic frameworks. *Coordination Chemistry Reviews* **2018**, 354, 28-45.
25. Wu, S.; Min, H.; Shi, W.; Cheng, P., Multicenter Metal–Organic Framework-Based Ratiometric Fluorescent Sensors. *Advanced Materials* **2019**, 0 (0), 1805871.
26. Stassen, I.; Burtch, N.; Talin, A.; Falcaro, P.; Allendorf, M.; Ameloot, R., An Updated Roadmap for the Integration of Metal–Organic Frameworks with Electronic Devices and Chemical Sensors. *Chemical Society Reviews* **2017**, 46 (11), 3185-3241.
27. Hendon, C. H.; Rieth, A. J.; Korzyński, M. D.; Dincă, M., Grand Challenges and Future Opportunities for Metal–Organic Frameworks. *ACS Central Science* **2017**, 3 (6), 554-563.
28. Cui, Y.; Li, B.; He, H.; Zhou, W.; Chen, B.; Qian, G., Metal–Organic Frameworks as Platforms for Functional Materials. *Accounts of Chemical Research* **2016**, 49 (3), 483-493.
29. Ma, S., Gas adsorption applications of porous metal–organic frameworks. In *Pure and Applied Chemistry*, 2009; Vol. 81, p 2235.
30. Dincă, M.; Long, J. R., Hydrogen Storage in Microporous Metal–Organic Frameworks with Exposed Metal Sites. *Angewandte Chemie International Edition* **2008**, 47 (36), 6766-6779.
31. Etacheri, V.; Di Valentin, C.; Schneider, J.; Bahnemann, D.; Pillai, S. C., Visible-light activation of TiO₂ photocatalysts: Advances in theory and experiments. *Journal of Photochemistry and Photobiology C: Photochemistry Reviews* **2015**, 25, 1-29.
32. Fujishima, A.; Honda, K., Electrochemical Photolysis of Water at a Semiconductor Electrode. *Nature* **1972**, 238 (5358), 37-38.
33. Gaya, U. I., *Heterogeneous Photocatalysis Using Inorganic Semiconductor Solids*. 1st ed. 2014. ed.; Springer Netherlands: Dordrecht, 2014.
34. Hernández-Alonso, M. D.; Fresno, F.; Suárez, S.; Coronado, J. M., Development of alternative photocatalysts to TiO₂: Challenges and opportunities. *Energy & Environmental Science* **2009**, 2 (12), 1231-1257.

35. Hashimoto, K.; Irie, H.; Fujishima, A., TiO₂ Photocatalysis: A Historical Overview and Future Prospects. *Japanese Journal of Applied Physics* **2005**, *44* (12), 8269-8285.
36. Dong, H.; Zeng, G.; Tang, L.; Fan, C.; Zhang, C.; He, X.; He, Y., An overview on limitations of TiO₂-based particles for photocatalytic degradation of organic pollutants and the corresponding countermeasures. *Water Research* **2015**, *79*, 128-146.
37. Weitkamp, J., Zeolites and catalysis. *Solid State Ionics* **2000**, *131* (1), 175-188.
38. Saeki, A.; Koizumi, Y.; Aida, T.; Seki, S., Comprehensive Approach to Intrinsic Charge Carrier Mobility in Conjugated Organic Molecules, Macromolecules, and Supramolecular Architectures. *Accounts of Chemical Research* **2012**, *45* (8), 1193-1202.
39. Savenije, T. J.; Ferguson, A. J.; Kopidakis, N.; Rumbles, G., Revealing the Dynamics of Charge Carriers in Polymer:Fullerene Blends Using Photoinduced Time-Resolved Microwave Conductivity. *The Journal of Physical Chemistry C* **2013**, *117* (46), 24085-24103.
40. Nasalevich, M. A.; van der Veen, M.; Kapteijn, F.; Gascon, J., Metal-organic frameworks as heterogeneous photocatalysts: advantages and challenges. *CrystEngComm* **2014**, *16* (23), 4919-4926.
41. Zeng, L.; Guo, X.; He, C.; Duan, C., Metal-Organic Frameworks: Versatile Materials for Heterogeneous Photocatalysis. *ACS Catalysis* **2016**, *6* (11), 7935-7947.
42. Dietzel, P. D. C.; Johnsen, R. E.; Fjellvåg, H.; Bordiga, S.; Groppo, E.; Chavan, S.; Blom, R., Adsorption properties and structure of CO₂ adsorbed on open coordination sites of metal-organic framework Ni₂(dhtp) from gas adsorption, IR spectroscopy and X-ray diffraction. *Chemical Communications* **2008**, (41), 5125-5127.
43. Dietzel, P. D. C.; Panella, B.; Hirscher, M.; Blom, R.; Fjellvåg, H., Hydrogen adsorption in a nickel based coordination polymer with open metal sites in the cylindrical cavities of the desolvated framework. *Chemical Communications* **2006**, (9), 959-961.
44. Putnis, A., Diffraction and Imaging. In *An Introduction to Mineral Sciences*, Cambridge University Press: United Kingdom, 1992; pp 41-80.
45. Harris, K. D. M.; Tremayne, M.; Kariuki, B. M., Contemporary Advances in the Use of Powder X-Ray Diffraction for Structure Determination. *Angewandte Chemie International Edition* **2001**, *40* (9), 1626-1651.
46. Prime, R. B. B., Harvey E.; Vyazovkin, Sergey; Gallagher, Patrick K.; Riga, Alan, Thermogravimetric Analysis (TGA). In *Thermal Analysis of Polymers*, 2008; pp 241-317.
47. Duerst, R. W.; Duerst, M. D.; Stebbings, W. L., Transmission Infrared Spectroscopy. In *Modern Techniques in Applied Molecular Spectroscopy*, Mirabella, F. M., Ed. John Wiley & Sons, Inc.: New York, 1998.
48. McHale, J. L., *Molecular Spectroscopy*. Prentice-Hall, Inc.: Upper Saddle River, NJ, 1999.
49. Hoffmann, H. C.; Debowski, M.; Müller, P.; Paasch, S.; Senkovska, I.; Kaskel, S.; Brunner, E., Solid-State NMR Spectroscopy of Metal-Organic Framework Compounds (MOFs). *Materials* **2012**, *5* (12), 2537-2572.
50. Sutrisno, A.; Huang, Y., Solid-state NMR: A powerful tool for characterization of metal-organic frameworks. *Solid State Nuclear Magnetic Resonance* **2013**, *49-50*, 1-11.
51. Wong, Y. T. A.; Martins, V.; Lucier, B. E. G.; Huang, Y., Solid-State NMR Spectroscopy: A Powerful Technique to Directly Study Small Gas Molecules Adsorbed

in Metal–Organic Frameworks. *Chemistry – A European Journal* **2019**, 25 (8), 1848-1853.

52. Singha, A.; Dhar, P.; Roy, A., A nondestructive tool for nanomaterials: Raman and photoluminescence spectroscopy. *American Journal of Physics* **2005**, 73 (3), 224-233.

53. Banerjee, D.; Chen, X.; Lobanov, S. S.; Plonka, A. M.; Chan, X.; Daly, J. A.; Kim, T.; Thallapally, P. K.; Parise, J. B., Iodine adsorption in metal organic frameworks in the presence of humidity. *ACS Applied Materials & Interfaces* **2018**, 10 (13), 10622-10626.

54. Chen, C.; Cai, L.-X.; Tan, B.; Zhang, Y.-J.; Yang, X.-D.; Zhang, J., Ammonia detection by using flexible Lewis acidic sites in luminescent porous frameworks constructed from a bipyridinium derivative. *Chemical Communications* **2015**, 51 (38), 8189-8192.

55. Chen, Y.; Wang, H.; Li, J.; Lockard, J. V., In Situ Spectroscopy Studies of CO₂ Adsorption in a Dually Functionalized Microporous Metal–Organic Framework. *Journal of Materials Chemistry A* **2015**, 3 (9), 4945-4953.

56. Chen, Y.; Zhang, J.; Li, J.; Lockard, J. V., Monitoring the Activation of a Flexible Metal–Organic Framework Using Structurally Sensitive Spectroscopy Techniques. *The Journal of Physical Chemistry C* **2013**, 117 (39), 20068-20077.

57. Goldman, M.; Huang, Y., Conformational analysis of 1,2-dichloroethane adsorbed in metal-organic frameworks. *Vibrational Spectroscopy* **2018**, 95, 68-74.

58. Jiang, D.; Urakawa, A.; Yulikov, M.; Mallat, T.; Jeschke, G.; Baiker, A., Size selectivity of a copper metal-organic framework and origin of catalytic activity in epoxide alcoholysis. *Chemistry - A European Journal* **2009**, 15 (45), 12255-62.

59. Jiang, S.; Hu, Y.; Chen, S.; Huang, Y.; Song, Y., Elucidation of the Structural Origins and Contrasting Guest-Host Interactions in CO₂-Loaded CdSDB and PbSDB Metal–Organic Frameworks at High Pressures. *Chemistry - A European Journal* **2018**, 24 (72), 19280-19288.

60. Kanoo, P.; Reddy, S. K.; Kumari, G.; Haldar, R.; Narayana, C.; Balasubramanian, S.; Maji, T. K., Unusual room temperature CO₂ uptake in a fluoro-functionalized MOF: insight from Raman spectroscopy and theoretical studies. *Chemical Communications* **2012**, 48 (68), 8487-8489.

61. Kim, J.; Oliver, A. G.; Neumann, G. T.; Hicks, J. C., Zn-MOFs Containing Pyridine and Bi-pyridine Carboxylate Organic Linkers and Open Zn²⁺ Sites. *European Journal of Inorganic Chemistry* **2015**, 2015 (18), 3011-3018.

62. Kumari, G.; Jayaramulu, K.; Maji, T. K.; Narayana, C., Temperature Induced Structural Transformations and Gas Adsorption in the Zeolitic Imidazolate Framework ZIF-8: A Raman Study. *The Journal of Physical Chemistry A* **2013**, 117 (43), 11006-11012.

63. Kumari, G.; Patil, N. R.; Bhadram, V. S.; Haldar, R.; Bonakala, S.; Maji, T. K.; Narayana, C., Understanding guest and pressure-induced porosity through structural transition in flexible interpenetrated MOF by Raman spectroscopy. *Journal of Raman Spectroscopy* **2016**, 47 (2), 149-155.

64. Liu, H.; Zhao, Y.; Zhang, Z.; Nijem, N.; Chabal, Y. J.; Peng, X.; Zeng, H.; Li, J., Ligand Functionalization and Its Effect on CO₂ Adsorption in Microporous Metal–Organic Frameworks. *Chemistry - An Asian Journal* **2013**, 8 (4), 778-785.

65. Liu, H.; Zhao, Y.; Zhang, Z.; Nijem, N.; Chabal, Y. J.; Zeng, H.; Li, J., The Effect of Methyl Functionalization on Microporous Metal-Organic Frameworks' Capacity and Binding Energy for Carbon Dioxide Adsorption. *Advanced Functional Materials* **2011**, *21* (24), 4754-4762.
66. Lobanov, S. S.; Daly, J. A.; Goncharov, A. F.; Chan, X.; Ghose, S. K.; Zhong, H.; Ehm, L.; Kim, T.; Parise, J. B., Iodine in metal-organic frameworks at high pressure. *The Journal of Physical Chemistry A* **2018**, *122* (29), 6109-6117.
67. Miller, S. R.; Pearce, G. M.; Wright, P. A.; Bonino, F.; Chavan, S.; Bordiga, S.; Margiolaki, I.; Guillou, N.; Ferey, G.; Bourrelly, S.; Llewellyn, P. L., Structural Transformations and Adsorption of Fuel-Related Gases of a Structurally Responsive Nickel Phosphonate Metal-Organic Framework, Ni-STA-12. *Journal of the American Chemical Society* **2008**, *130* (47), 15967-15981.
68. Nijem, N.; Thissen, P.; Yao, Y.; Longo, R. C.; Roodenko, K.; Wu, H.; Zhao, Y.; Cho, K.; Li, J.; Langreth, D. C.; Chabal, Y. J., Understanding the Preferential Adsorption of CO₂ over N₂ in a Flexible Metal–Organic Framework. *Journal of the American Chemical Society* **2011**, *133* (32), 12849-12857.
69. Nijem, N.; Wu, H.; Canepa, P.; Marti, A.; Balkus, K. J.; Thonhauser, T.; Li, J.; Chabal, Y. J., Tuning the Gate Opening Pressure of Metal–Organic Frameworks (MOFs) for the Selective Separation of Hydrocarbons. *Journal of the American Chemical Society* **2012**, *134* (37), 15201-15204.
70. Panella, B.; Hirscher, M., Raman studies of hydrogen adsorbed on nanostructured porous materials. *Phys. Chem. Chem. Phys.* **2008**, *10* (20), 2910-2917.
71. Prestipino, C.; Regli, L.; Vitillo, J. G.; Bonino, F.; Damin, A.; Lamberti, C.; Zecchina, A.; Solari, P. L.; Kongshaug, K. O.; Bordiga, S., Local Structure of Framework Cu(II) in HKUST-1 Metallorganic Framework: Spectroscopic Characterization upon Activation and Interaction with Adsorbates. *Chemistry of Materials* **2006**, *18* (5), 1337-1346.
72. Siberio-Pérez, D. Y.; Wong-Foy, A. G.; Yaghi, O. M.; Matzger, A. J., Raman Spectroscopic Investigation of CH₄ and N₂ Adsorption in Metal–Organic Frameworks. *Chemistry of Materials* **2007**, *19* (15), 3681-3685.
73. Souto, M.; Romero, J.; Calbo, J.; Vitorica-Yrezabal, I. J.; Zafra, J. L.; Casado, J.; Orti, E.; Walsh, A.; Minguez Espallargas, G., Breathing-Dependent Redox Activity in a Tetrathiafulvalene-Based Metal-Organic Framework. *Journal of the American Chemical Society* **2018**, *140* (33), 10562-10569.
74. Strauss, I.; Mundstock, A.; Hinrichs, D.; Himstedt, R.; Knebel, A.; Reinhardt, C.; Dorfs, D.; Caro, J., The Interaction of Guest Molecules with Co-MOF-74: A Vis/NIR and Raman Approach. *Angewandte Chemie International Edition* **2018**, *57* (25), 7434-7439.
75. Szilagy, P. A.; Rogers, D. M.; Zaiser, I.; Callini, E.; Turner, S.; Borgschulte, A.; Züttel, A.; Geerlings, H.; Hirscher, M.; Dam, B., Functionalised metal-organic frameworks: a novel approach to stabilising single metal atoms. *J. Mater. Chem. A* **2017**, *5* (30), 15559-15566.
76. Tan, K.; Nijem, N.; Canepa, P.; Gong, Q.; Li, J.; Thonhauser, T.; Chabal, Y. J., Stability and Hydrolyzation of Metal Organic Frameworks with Paddle-Wheel SBUs upon Hydration. *Chemistry of Materials* **2012**, *24* (16), 3153-3167.

77. Yao, Y.; Nijem, N.; Li, J.; Chabal, Y. J.; Langreth, D. C.; Thonhauser, T., Analyzing the Frequency Shift of Physiaisorbed CO₂ in Metal Organic Framework Materials. *Physical Review B* **2012**, 85 (6), 064302.
78. Zeng, M.-H.; Yin, Z.; Tan, Y.-X.; Zhang, W.-X.; He, Y.-P.; Kurmoo, M., Nanoporous Cobalt(II) MOF Exhibiting Four Magnetic Ground States and Changes in Gas Sorption upon Post-Synthetic Modification. *J. Am. Chem. Soc.* **2014**, 136 (12), 4680-4688.
79. Nijem, N.; Chabal, Y., Adsorbate Interactions in Metal Organic Frameworks Studied by Vibrational Spectroscopy. *Comments on Inorganic Chemistry* **2014**, 34 (3-4), 78-102.
80. Martra, G.; Gianotti, E.; Coluccia, S., The Application of UV-Visible-NIR Spectroscopy to Oxides. In *Metal Oxide Catalysis*, Jackson, S. D.; Hargreaves, J. S., Eds. 2009; pp 51-94.
81. Schoonheydt, R. A., UV-VIS-NIR spectroscopy and microscopy of heterogeneous catalysts. *Chemical Society Reviews* **2010**, 39 (12), 5051-5066.
82. Torrent, J., Diffuse Reflectance Spectroscopy of Iron Oxides. In *Encyclopedia of Surface and Colloid Science*, 3rd ed.; Somasundaran, P., Ed. 2016; pp 1731–1739.
83. Sinfelt, J. H.; Meitzner, G. D., X-ray absorption edge studies of the electronic structure of metal catalysts. *Accounts of Chemical Research* **1993**, 26 (1), 1-6.
84. Bertagnolli, H.; Ertel, T. S., X-Ray Absorption Spectroscopy of Amorphous Solids, Liquids, and Catalytic and Biochemical Systems—Capabilities and Limitations. *Angewandte Chemie International Edition* **1994**, 33 (1), 45-66.
85. Filipponi, A., EXAFS for liquids. *Journal of Physics: Condensed Matter* **2001**, 13 (7), R23-R60.
86. Frenkel, A. I.; Yevick, A.; Cooper, C.; Vasic, R., Modeling the Structure and Composition of Nanoparticles by Extended X-Ray Absorption Fine-Structure Spectroscopy. *Annual Review of Analytical Chemistry* **2011**, 4 (1), 23-39.
87. Frenkel, A. I., Applications of extended X-ray absorption fine-structure spectroscopy to studies of bimetallic nanoparticle catalysts. *Chemical Society Reviews* **2012**, 41 (24), 8163-8178.
88. Bordiga, S.; Groppo, E.; Agostini, G.; van Bokhoven, J. A.; Lamberti, C., Reactivity of Surface Species in Heterogeneous Catalysts Probed by In Situ X-ray Absorption Techniques. *Chemical Reviews* **2013**, 113 (3), 1736-1850.
89. Soldatov, M. A.; Martini, A.; Bugaev, A. L.; Pankin, I.; Medvedev, P. V.; Guda, A. A.; Aboraia, A. M.; Podkovyrina, Y. S.; Budnyk, A. P.; Soldatov, A. A.; Lamberti, C., The insights from X-ray absorption spectroscopy into the local atomic structure and chemical bonding of Metal–organic frameworks. *Polyhedron* **2018**, 155, 232-253.
90. van Bokhoven, J. A.; Lamberti, C. In *State-of-the-Art X-Ray Spectroscopy in Catalysis*, Wiley-VCH Verlag GmbH & Co. KGaA: 2017; pp 1029-1054.
91. Senkovska, I.; Bon, V. In *In Situ X-ray Diffraction and XAS Methods*, Wiley-VCH Verlag GmbH & Co. KGaA: 2016; pp 691-727.
92. Bordiga, S.; Bonino, F.; Lillerud, K. P.; Lamberti, C., X-ray absorption spectroscopies: useful tools to understand metallorganic frameworks structure and reactivity. *Chemical Society Reviews* **2010**, 39 (12), 4885-4927.
93. Yano, J.; Yachandra, V. K., X-ray absorption spectroscopy. *Photosynthesis Research* **2009**, 102 (2), 241.

94. Lee, N. P.; Taras, Bergmann, Uwe; Neese, Frank; DeBeer, Serena, Probing Valence Orbital Composition with Iron K α X-ray Emission Spectroscopy. *Journal of American Chemical Society* **2010**, *132*, 9715–9727.
95. Keyes, T. E.; Forster, R. J.; Blackledge, C., Time resolved spectroscopy of inorganic complexes. In *Spectroscopic Properties of Inorganic and Organometallic Compounds: Techniques, Materials and Applications, Volume 41*, The Royal Society of Chemistry: 2010; Vol. 41, pp 211-261.
96. Tkachenko, N. V., *Optical Spectroscopy: Methods and Instrumentations*. Elsevier Science: 2006.
97. Chuang, C.-H.; Burda, C., Contribution of Femtosecond Laser Spectroscopy to the Development of Advanced Optoelectronic Nanomaterials. *The Journal of Physical Chemistry Letters* **2012**, *3* (14), 1921-1927.
98. Laurier, K. G. M.; Fron, E.; Atienzar, P.; Kennes, K.; Garcia, H.; Van der Auweraer, M.; De Vos, D. E.; Hofkens, J.; Roelofs, M. B. J., Delayed electron–hole pair recombination in iron(III)-oxo metal–organic frameworks. *Physical Chemistry Chemical Physics* **2014**, *16* (11), 5044-5047.
99. Chen, L. X.; Zhang, X.; Lockard, J. V.; Stickrath, A. B.; Attenkofer, K.; Jennings, G.; Liu, D.-J., Excited-state molecular structures captured by X-ray transient absorption spectroscopy: a decade and beyond. *Acta Crystallographica Section A* **2010**, *66* (2), 240-251.
100. Bressler, C.; Chergui, M., Ultrafast X-ray Absorption Spectroscopy. *Chemical Reviews* **2004**, *104* (4), 1781-1812.
101. Chen, L. X.; Zhang, X., Photochemical Processes Revealed by X-ray Transient Absorption Spectroscopy. *The Journal of Physical Chemistry Letters* **2013**, *4* (22), 4000-4013.
102. Shelby, M. L.; Mara, M. W.; Chen, L. X., New Insight into Metalloporphyrin Excited State Structures and Axial Ligand Binding from X-ray Transient Absorption Spectroscopic Studies. *Coordination Chemistry Reviews* **2014**, *277–278*, 291-299.
103. Smolentsev, G.; Sundström, V., Time-resolved X-ray Absorption Spectroscopy for the Study of Molecular Systems Relevant for Artificial Photosynthesis. *Coordination Chemistry Reviews* **2015**, *304–305*, 117-132.
104. Pattengale, B.; Yang, S.; Ludwig, J.; Huang, Z.; Zhang, X.; Huang, J., Exceptionally Long-Lived Charge Separated State in Zeolitic Imidazolate Framework: Implication for Photocatalytic Applications. *Journal of the American Chemical Society* **2016**, *138* (26), 8072-8075.
105. Hanna, L.; Kucheryavy, P.; Liu, C.; Zhang, X.; Lockard, J. V., Long-Lived Photoinduced Charge Separation in a Trinuclear Iron- μ_3 -oxo-based Metal–Organic Framework. *The Journal of Physical Chemistry C* **2017**, *121* (25), 13570-13576.
106. Pattengale, B.; SantaLucia, D. J.; Yang, S.; Hu, W.; Liu, C.; Zhang, X.; Berry, J. F.; Huang, J., Direct Observation of Node-to-Node Communication in Zeolitic Imidazolate Frameworks. *Journal of the American Chemical Society* **2018**, *140* (37), 11573-11576.
107. Yang, S.; Fan, D.; Hu, W.; Pattengale, B.; Liu, C.; Zhang, X.; Huang, J., Elucidating Charge Separation Dynamics in a Hybrid Metal–Organic Framework Photocatalyst for Light-Driven H₂ Evolution. *The Journal of Physical Chemistry C* **2018**, *122* (6), 3305-3311.

Chapter 2. Spectroscopic characterization of metal ligation in trinuclear iron- μ_3 -oxo-based complexes and metal-organic frameworks

2.1 Introduction

Metal organic frameworks (MOFs) are hybrid solid state materials composed of metal-containing inorganic clusters connected by organic linker components. Their porous nature, ability to self-assemble, and versatile chemical composition and structure make them ideal for potential applications in gas separation, sensing, heterogeneous catalysis, and others.¹⁻⁷ In many cases, open metal sites within the frameworks, first exposed by thermal removal of labile solvent molecules, provide the primary docking sites for the adsorption of guest molecules within the pores. Understanding the nature of these specific interactions and unambiguous identification of bound species is paramount to the future development and application of these materials for adsorption-based applications.

Characterization of MOF materials through spectroscopy can provide these much-needed molecular-level insights. Vibrational spectroscopy methods, namely, FTIR and Raman spectroscopy, are commonly used to establish the presence and interaction of guest species with the host framework through the appearance of their characteristic mode frequencies.⁸⁻¹² Moreover, changes in MOF-based vibrational modes upon activation and guest introduction can indicate how framework structures themselves are altered in the process.^{9, 12-15} Interpreting these changes can be a challenge, particularly for MOF-localized modes that are difficult to assign. Even with unambiguous vibrational mode assignments, MOF host–guest interactions are best corroborated through characterization by other complementary structurally sensitive spectroscopy methods.

On account of its element specificity, hard X-ray absorption spectroscopy (XAS) provides valuable electronic and neighboring atom information about the metal coordination sites and their potential changes under different guest environments. In addition to evaluating postsynthetic framework metalation by confirming metal coordination environments,¹⁶⁻²² this method has been used to probe changes in MOF metal site geometry, and oxidation state upon framework activation^{13, 23-25} and inclusion of guest species relevant to gas adsorption,^{8, 26-27} and catalysis.^{18, 28-30} Despite this broad application however, the method is relatively insensitive to neighboring atoms of similar atomic number and requires time-dependent density functional theory (TDDFT) calculations that can be exceedingly difficult to perform for the multimetallic cluster or infinite chain node structures commonly found in MOF architectures. These two factors limit the utility of XAS alone and require supplemental characterization for more in-depth evaluation of MOF host/guest chemistry.

This chapter explores the use of X-ray emission spectroscopy (XES) as a complementary method to XAS, for characterizing the local coordination environment of the metal sites in MOF materials under different host/guest conditions. While XAS probes unfilled orbitals accessed through core electron transitions, XES provides information about the occupied orbitals by monitoring core hole filling processes. When the decay process involves valence orbital electrons (with metal p in addition to d character), which participate most in metal bonding interactions through ligand ns and np orbital mixing, the resulting emission lines become exceptionally sensitive to electronic structure differences of the coordinated ligands. The ligand sensitivity of this valence-to-core (vtc) XES method has been recognized for some time.³¹⁻³⁷ It has been used to study

a variety of systems, from transition metal-based coordination complexes with biological and chemical catalysis relevance^{36, 38-45} to enzymes⁴⁶⁻⁴⁸ to metal-substituted zeolites.⁴⁹⁻⁵² Many of these studies have illustrated how DFT computational methods can be used to calculate vtc-XES with sufficient accuracy to provide meaningful transition assignments. This offers a substantial advantage over XAS modeling, which typically requires more complicated TDDFT calculations that can be inaccurate or difficult to interpret, particularly for multimetallic species.

Intriguing preliminary data were presented several years ago demonstrating the feasibility of using vtc-XES spectroscopy to characterize MOF materials.⁵³ This chapter presents the first in depth nonresonant vtc-XES study of a MOF system and several key molecular model complexes to illustrate its sensitivity to guest species interactions at framework metal sites and therefore its complementarity with conventional XAS and vibrational spectroscopy characterization of this material. The iron(III)-based MOF, MIL100(Fe), composed of Fe₃-μ₃-oxo clusters connected in a porous 3D network through trimesic acid linkers as illustrated in Figure 2.1, is chosen for this study because of its trinuclear metal-oxo nodal structure that is both ubiquitous across many types of MOF topologies⁵⁴⁻⁵⁸ and easily modeled by molecular Fe₃-μ₃-oxo-based complexes. This well-characterized framework has been explored for applications that rely on the Lewis acidity of its open metal sites, such as catalysis⁵⁹⁻⁶² and hydrocarbon gas separation.⁶³⁻⁶⁴ Here, following the removal of the initial solvent (water) guest environment through thermal activation, we introduce representative guest molecules (pyridine or propylene) into the framework to model the host–guest interactions behind these adsorption-based applications. These systems are then measured by both Fe K-edge XAS and Kβ XES,

along with vibrational spectroscopy methods, which further confirm the presence of guest species in the frameworks. This study demonstrates the utility and limitations of the combined spectroscopy approach for probing different metal ligand environments in MOF materials that would be typically difficult to distinguish by conventional XAS or vibrational characterization alone. Iron (III) benzoate reference complexes, which have known axial ligands, serve as molecular analogs for the trinuclear cores within the framework under guest treatment conditions. These complexes are measured as well to help establish the spectral trends associated with different ligand environments. The vtc-XES spectra are interpreted with the aid of DFT calculations that provide insight on the molecular orbital parentage of the transitions involved.

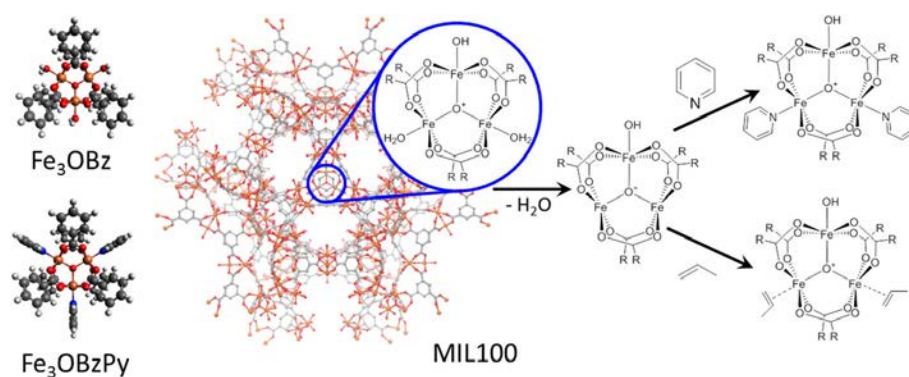


Figure 2.1 (Left) μ_3 -oxo trinuclear iron core of reference complexes Fe_3OBz and Fe_3OBzPy . (Right) Hydrated $\text{MIL100}(\text{Fe})$ structure with highlighted trinuclear nodes depicting hydrated and activated $\text{MIL100}(\text{Fe})$ -Act forms and proposed structures upon treatment with pyridine, $\text{MIL100}(\text{Fe})$ -Py, or propylene, $\text{MIL100}(\text{Fe})$ -Prop, guest environments.

2.2 Experimental and Computational Methods

2.2.1 Materials and Synthesis

2.2.1.1 Materials

All solvents and starting materials, $\text{Fe}(\text{NO}_3)_3 \cdot 9\text{H}_2\text{O}$, 1,3,5-benzenetricarboxylic acid, sodium hydroxide, $\text{FeCl}_3 \cdot 6\text{H}_2\text{O}$, $\text{FeCl}_2 \cdot 4\text{H}_2\text{O}$, and benzoic acid, were used without further purification, with the exception of pyridine (99%+), which was dried over molecular sieves prior to use. $\text{MIL100}(\text{Fe})$ ⁵⁹ and the iron(III) benzoate (Fe_3OBz) and iron(III) benzoate pyridine (Fe_3OBzPy) reference complexes⁶⁵ were synthesized according to literature precedent. All solvents and starting materials, $\text{Fe}(\text{NO}_3)_3 \cdot 9\text{H}_2\text{O}$, 1,3,5-benzenetricarboxylic acid, sodium hydroxide, $\text{FeCl}_3 \cdot 6\text{H}_2\text{O}$, $\text{FeCl}_2 \cdot 4\text{H}_2\text{O}$, and benzoic acid, were used without further purification, with the exception of pyridine (99%+), which was dried over molecular sieves prior to use.

2.2.1.2 Synthesis

$\text{MIL100}(\text{Fe})$ ⁶² and the iron (III) benzoate (Fe_3OBz) and iron (III) benzoate pyridine (Fe_3OBzPy) reference complexes⁶⁵ were synthesized according to literature precedent. The treated MOF samples, activated MIL-100 and MIL-100 with pyridine, were prepared according to literature.⁶⁴ 100 mg of as synthesized (AS) MIL-100 was heated to 150°C under inert conditions on a Schlenk line for 12 hours. The sample was then transferred to a glove box. After drying over activated molecular sieves for 2 hours, pyridine was injected into a portion of activated MIL-100 under inert conditions and stirred overnight. The sample was isolated via vacuum filtration under ambient conditions.

2.2.2 Characterization

Powder XRD patterns were recorded using a Bruker D8 ADVANCE ECO Diffractometer. Attenuated total reflectance infrared spectra were collected for solid samples at room temperature using Nicolette 6700 FT-IR spectrometer. Each spectrum was recorded as an average of 64 scans.

2.2.3 Raman spectroscopy

Raman spectra were collected at room temperature with a triple monochromator and a 1340×100 pixel liquid nitrogen-cooled CCD detector (Princeton Instruments) using 420 nm laser excitation generated from the second harmonic of the fundamental output of a picosecond Ti:sapphire laser oscillator (Tsunami, Spectra-Physics) or 532 nm excitation from a single-frequency diode laser (Spectra-Physics), each with ~ 5 mW power. For *ex situ* measurements, samples were prepared in pellet form by mixing each complex or MOF sample with KNO_3 standard in a 4:1 mass ratio. *In situ* Raman spectra were collected using a home-built controlled gas environment chamber. The chamber contains a rotating platform that allows sample spinning upon irradiation. A heater is located on the mounting surface of this spinning platform for controlling bulk sample temperature during the experiment. Samples were suspended in CCl_4 and deposited on a metal frit that is then attached to the spinning heater inside the environment chamber. The temperature of the deposited sample was monitored throughout the experiment by an IR temperature probe. To activate, the sample was heated in the chamber to 150°C for 2 h under dynamic vacuum. Spectra were measured once the sample was exposed to ambient pressure dry nitrogen and cooled to room temperature. The nitrogen environment was exchanged with propylene gas for a minimum of 30 min before spectra were collected. The sample was then re-exposed to water vapor in the air by opening the chamber and

allowing the sample to equilibrate for 2 h before the spectrum was collected. All Raman data were collected on spinning samples to avoid laser damage by minimizing its residence time.

2.2.4 X-ray absorption spectroscopy

X-ray absorption data were collected at the Fe K-edge (7111.2 eV) in transmission mode at Beamline 6BM at NSLS II using a 3-pole wiggler source and an optical system composed of a paraboloid collimating mirror, Si(111) face monochromator, a toroidal focusing mirror, and a flat harmonic rejection mirror. The monochromatized beam was generated with a 2×1 mm spot size and a resolving power of $1.3 \times 10^{-4} \Delta E/E$. The incident (I_0), transmitted (I_t), and reference (I_r) beam intensities were all measured by 15 cm ionization chambers filled with 100% N₂ gas. Iron foil was used as the reference for energy calibration. For the reference complexes, a mixture of ~15 mg sample was thoroughly ground with 150 mg of boron nitride, to achieve one absorption length. For the MOF samples, 30 mg of MOF sample and ~150 mg of boron nitride were used for dilution. All data were collected at room temperature. Three spectra were collected, each with 20 min acquisition time, and averaged for each sample. To test sample stability with respect to X-ray damage, a minimum of three sequential fast X-ray absorption near-edge structure (XANES) scans were first collected on the same spot of each sample, revealing negligible changes. Moreover, no evidence of X-ray damage was observed upon longer sample irradiation times associated with the full EXAFS data collection.

EXAFS data were processed and analyzed using the Demeter program package.⁶⁶ Fourier Transform spectra were obtained using k^2 weighting and a $\chi(k)$ range from 2 to 12

\AA^{-1} Fitting was performed in R space over the range of 1 to 3.5 \AA using models derived from the reported crystal structures for Fe_3OBz and Fe_3OBzPy .^{65, 67} The fits to the experimental data are shown in Figure 2.8 and 2.9.

2.2.5 X-ray emission spectroscopy

Nonresonant Fe $\text{K}\beta$ XES spectra were collected at the C1 beamline of CHESS with an incident X-ray energy of 8 keV generated from a WB_4C multilayer monochromator and a beam size of 1×1 mm. X-ray emission was collected using five spherically bent Ge(620) analyzer crystals aligned in the Rowland circle geometry and focused to a Pilatus 1000k detector.⁶⁸ A helium-filled bag was placed between the analyzer crystals and detector to maximize the collection efficiency of the emission. The XES spectrometer was calibrated using Fe_2O_3 standard. Samples were tightly packed in 0.7 mm thick aluminum holders with 3×6 mm window and sealed with a Kapton tape. Fe vtc and mainline $\text{K}\beta$ emission spectra were collected between 7070 and 7130 eV with 84 points and 7017 and 7085 eV with 121 points, respectively. Sample stability was first evaluated by collecting sequential XES spectra (mainline and vtc regions) on a given sample spot. No systematic spectral changes were observed within the first several scans. Out of an abundance of caution, however, all samples were translated in the beam to a fresh spot between scans and collected at a temperature of 10 K using a closed cycle helium gas cryostat. Multiple MOF samples, separately prepared from different batches of each guest environment treatment, were measured to ensure reproducibility and discount the possibility of batch-dependent spectral differences. At least 36 vtc-XES and 2 mainline $\text{K}\beta$ spectra were collected for each sample for averaging with an acquisition

time of approximately 8 min per vtc spectrum and 12 min per mainline spectrum. The averaged spectra for each sample were normalized to unit area over the vtc region.

2.2.6 Computational methods

2.2.6.1 DFT Calculations

DFT calculations were conducted using the ORCA 4.0.1 software package⁶⁹⁻⁷⁰ and geometries derived from the crystal structures of Fe₃OBz,⁶⁷ Fe₃OBzPy,⁶⁵ and MIL100(Fe).⁶⁰ Since no crystal structure is reported for MIL100(Fe)-Py, the trinuclear iron-oxo cluster geometry was obtained from the MIL100(Fe) structure and modified to include pyridine axial ligands with the same Fe—pyridine distance as in the Fe₃OBzPy complex. XES calculations were performed using BP86 functional and def2-TZVP basis set⁷¹⁻⁷² for all atoms except iron, which had a CP(PPP) basis set. The selected level of theory, functional, and basis set combination was used following a procedure similar to that reported by DeBeer *et al.*⁴² and was first calibrated using ferricyanide as a benchmark. Moreover, the model complexes, with known structures, also serve as a check on the validity of the method for reproducing the spectral trends observed experimentally. Following literature precedent,^{42,73} a constant energy shift of 179.4 eV and Gaussian broadening (FWHM = 3.5 eV) was applied to each transition to generate the total calculated spectra that upon averaging (*vide infra*) mimics the energy and width of the experimental spectra. Single point calculations, using the same functional and basis sets, were conducted to generate the molecular orbitals, which were rendered using Chemcraft 1.8.⁷⁴

2.3 Results and Discussion

2.3.1 MOF guest molecule introduction and bulk characterization

As illustrated in Figure 2.1, each iron atom in the trinuclear cluster has a pore-facing coordination site occupied by either a water molecule or a hydroxyl group. Relatively mild vacuum-assisted thermal ($100\text{ }^{\circ}\text{C} < T < 150\text{ }^{\circ}\text{C}$) activation conditions remove unbound and axially coordinated water molecules from the pores, theoretically leaving each cluster of the activated framework, MIL100(Fe)-Act, with two open metal sites and a residual metal-bound hydroxyl group. Subsequent introduction of other species (pyridine and propylene) to the activated framework, MIL100(Fe)-Py and MIL100(Fe)-Prop, leads to guest interaction at the available metal sites, with strength of coordination depending on the binding affinity of the guest. Compared to water and pyridine, propylene is expected to interact much more weakly with the iron sites. Consequently, while MIL100(Fe) and MIL100(Fe)-Py are stable under air atmosphere, the propylene-loaded framework was isolated under pure propylene gas atmosphere for spectroscopy characterization. Moreover, MIL100(Fe)-Act was measured under dry nitrogen to avoid water recoordination of the metal sites from moisture in the air. The confirmation and retention of crystallinity upon synthesis, activation, and guest treatment is provided by powder X-ray diffraction, shown in Figure 2.2.

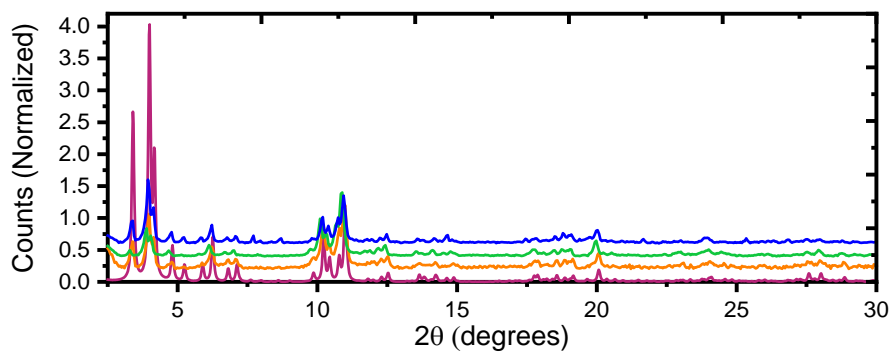


Figure 2.2: PXRD Pattern of MIL100(Fe) Simulated (Magenta), MIL100(Fe) (orange), MIL100(Fe)-Act (green), and MIL100(Fe)-Py (blue)

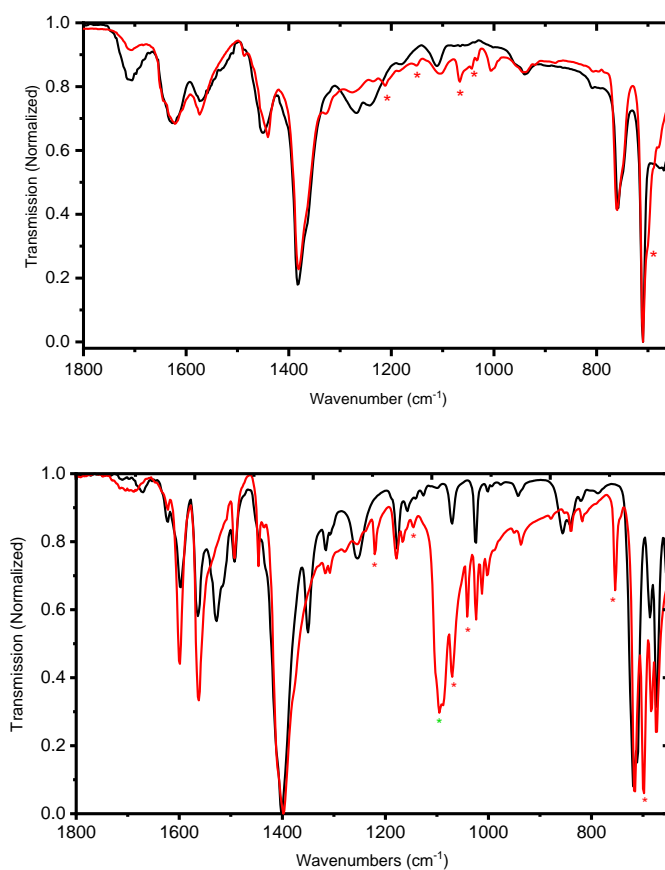


Figure 2.3: FT-IR Spectra of (top): MIL100(Fe) (black) and MIL100(Fe)-Py (red) and (bottom): Fe₃OBz (black) and Fe₃OBzPy (red) with characteristic pyridine modes^{62, 75} marked with red asterisks, perchlorate modes marked with green asterisk

2.3.1.1 Raman spectroscopy

Vibrational mode characterization of the MIL100(Fe) frameworks under the different treatments described above is used to corroborate the presence of certain guest species in the MOFs and, in some cases, provide evidence for their interaction with the open metal sites. Comparison of Raman spectra collected for MIL100(Fe) and MIL100(Fe)-Py (Figure 2.4) reveals the appearance of characteristic pyridine modes at 650, 1014, and 1043 cm^{-1} for the pyridine-loaded framework, signaling the presence of this guest environment in the MOF. The analogous spectral comparison for the model complexes, also presented in Figure 2.4, shows these pyridine-localized modes at nearly identical frequencies for the Fe_3OBzPy complex. An additional pyridine mode is observed in this spectrum at 1221 cm^{-1} but is obscured by framework linker localized modes in the MIL100(Fe)-Py spectrum. The pyridine ring stretching modes with A_1 symmetry that occur at around 1014 and 1043 cm^{-1} in the spectra of both pyridine-coordinated species are significantly shifted to higher frequencies compared to those of free pyridine. This frequency shift has been well documented for other pyridine coordination complexes⁷⁶⁻⁷⁷ and is attributed to coupling with the Fe—N stretching mode that is introduced upon pyridine coordination at the metal site.⁷⁷

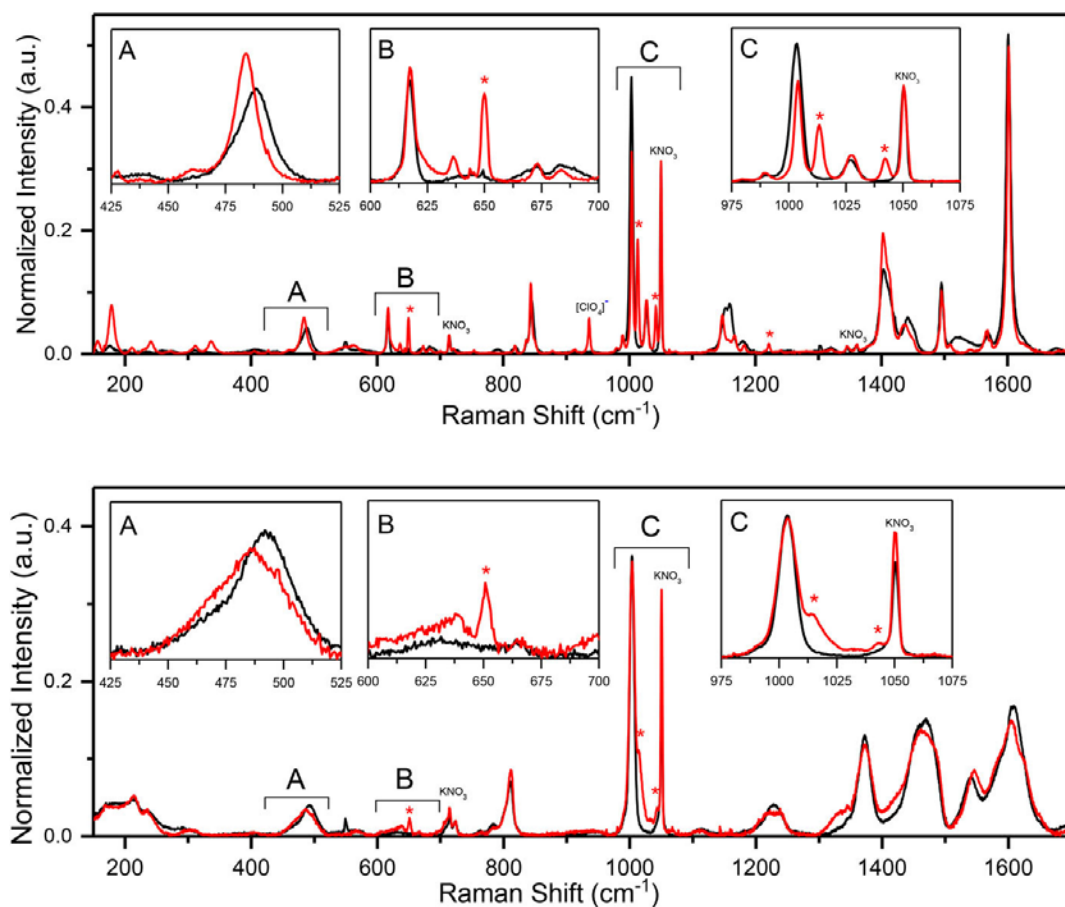


Figure 2.4 Raman spectra of (top) Fe₃OBz (black) and Fe₃OBzPy (red) and (bottom) MIL100(Fe) (black) and MIL100Fe-Py (red). Magnified spectral regions are shown in the inset spectra. KNO₃ (standard) and [ClO₄][−] (Fe₃OBzPy counterion) modes are labeled accordingly. Asterisks mark modes attributed to pyridine guest species.

Changes in framework-localized vibrational modes can also reveal direct and indirect structural ramifications of pyridine introduction to the MOF. Subtle differences in modes with frequency $>\sim 800\text{ cm}^{-1}$ tend to provide linker site structural information but are less diagnostic of guest species interaction with the open Fe sites of the nodes. Low frequency modes localized around the iron-oxo cluster should be more sensitive to changes in metal coordination, as they will undoubtedly be influenced by the terminal ligand.⁷⁸ Notably,

the mode that occurs at 489 cm^{-1} for Fe_3OBz and 492 cm^{-1} for MIL100, which we assign as a carboxylate rocking mode with Fe—O distortion,⁶⁵ shifts to lower frequency for the two pyridine coordinated species [483 cm^{-1} for Fe_3OBzPy and 486 cm^{-1} for MIL100(Fe)Py], reflecting the analogous change in force constant that accompanies the axial ligand change from water to pyridine in each case.

Substantial differences in other lower frequency modes of the two reference complexes are observed, including the appearance of modes around 200 cm^{-1} that may involve Fe—N_{py} stretch. The analogous MOF spectra, however, do not show these distinguishing features. Instead, the spectra exhibit regions of poorly resolved overlapping features, which most likely stem from both phonon mode coupling contributions and framework cluster inhomogeneities.

In-situ Raman spectroscopy was used to characterize the activated and propylene-containing MOFs, MIL100(Fe)-Act and MIL100(Fe)-Prop, and the results are shown in Figure. 2.5.

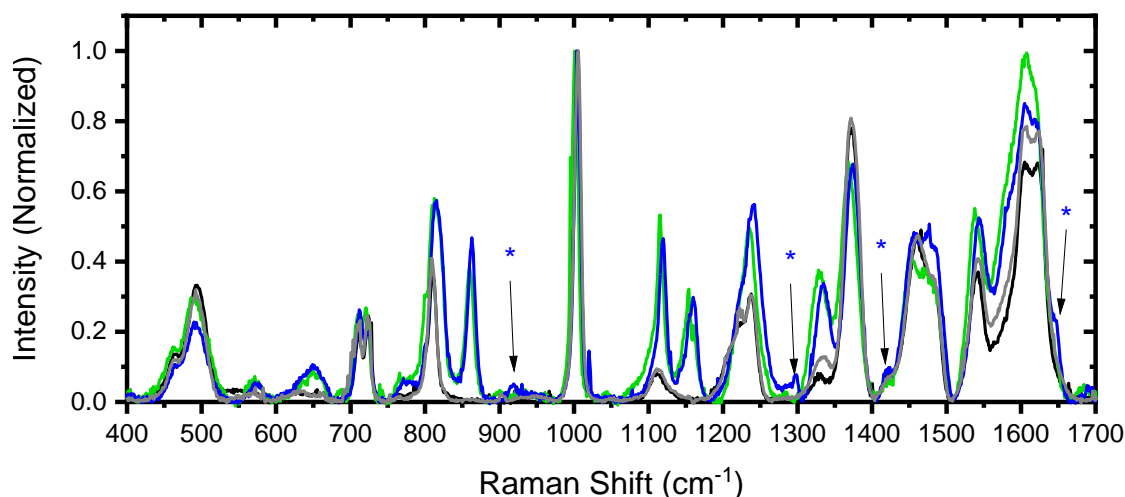


Figure 2.5: Raman spectra (obtained using 420 nm excitation through in situ measurement) highlighting the propylene modes⁷⁹ (indicated with asterisks) found in the propylene exposed MOF sample (blue) and compared to MIL100(Fe) (black), activated framework after 150°C in situ treatment for 3 hours (green), and after re-exposure to moisture in the air (gray).

The most significant changes are observed for the framework-based modes upon initial activation, reflecting the direct and indirect structural ramifications of water removal from the metal sites. Notably, in the spectrum of the activated MOF, new features are observed at 850 cm^{-1} and 1150 cm^{-1} , which may be attributed to Fe—OH stretching and deformation modes localized on the hydroxyl-coordinated iron site. Their appearance in this spectrum is likely a consequence of the drastic local symmetry change in the trinuclear iron oxo cluster created by removing the terminal H_2O species from two of the three iron sites (leaving one hydroxyl-bound iron). All spectral features readily recover upon rehydration of the framework, illustrating the reversibility of water coordination of the metal sites. Spectra collected upon framework activation followed by subsequent exposure to propylene gas revealed the presence of this guest molecule through the

observation of its characteristic vibrational modes. The C=C stretch observed at 1647 cm^{-1} for free propylene should shift to lower frequency upon metal binding owing to the π -electron interaction.⁸⁰ However, this region of the MOF spectrum is dominated by the strong $\nu(\text{C}=\text{C})$ peak of the framework linker. The propylene $\nu(\text{C}=\text{C})$ marker mode is observed as a poorly resolved shoulder, so any frequency shift is difficult to evaluate. The vibrations of the framework under propylene atmosphere appear similar to those of the activated MOF, which likely results from the weak interaction of this guest species.

2.3.1.2 X-ray absorption spectroscopy

Conventional XAS measurements collected for MIL100(Fe), MIL100(Fe)-Act, and MIL100(Fe)—Py as well as the corresponding iron benzoate (Fe_3OBz) and iron benzoate pyridine (Fe_3OBzPy) model complexes are depicted in Figure. 2.6. Comparison of the MOF spectra reveals modest differences that qualitatively reflect the Fe coordination environments of each framework. The comparable edge shifts, shown in Figure 2.7, indicate the retention of Fe(III) oxidation status in each case.

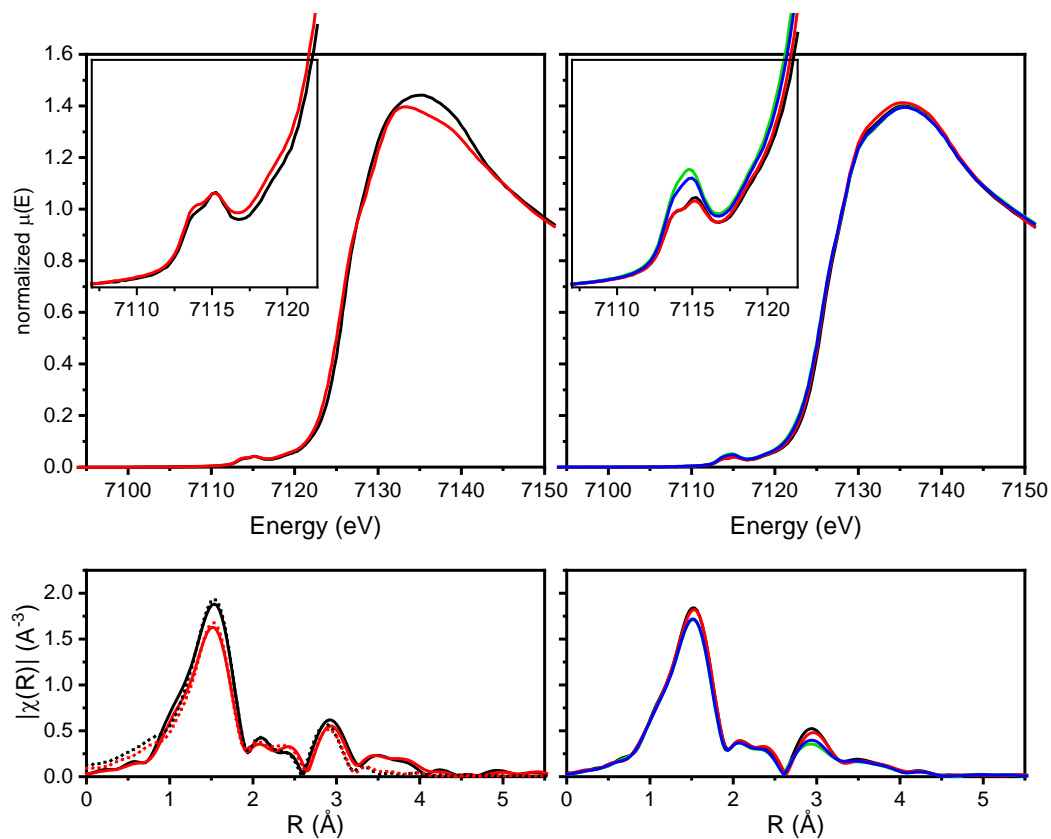


Figure 2.6 XANES spectra with magnified pre-edge regions (top) and EXAFS spectra (bottom) of reference complexes (left)— Fe_3OBz (black) and Fe_3OBzPy (red), and MOFs (right)—MIL100(Fe) (black), MIL100(Fe)-Py (red), MIL100(Fe)-Act (green), and MIL100(Fe)-Prop (blue).

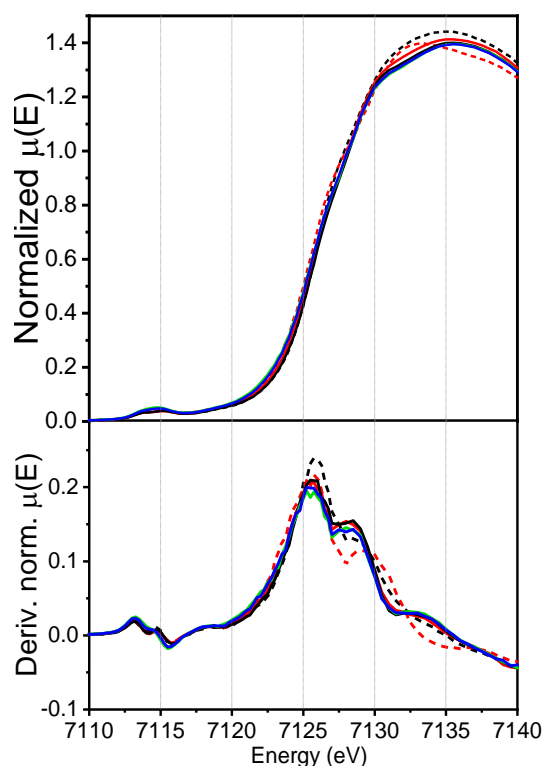


Figure 2.7: XANES spectra (top) and first derivative spectra (bottom) of Fe₃OBz (black, dashed), Fe₃OBzPy (red, dashed), MIL100(Fe) (black, solid), MIL100(Fe)-Act (green, solid), MIL100(Fe)-Py (red, solid), and MIL100(Fe)-Prop (blue).

The pre-edge features in the XANES region exhibit the expected trends for the changing coordination environment of the iron sites.⁸¹ In other words, the lower symmetry associated with pentacoordinated square pyramidal geometry of the activated framework leads to increased intensity in the pre-edge feature compared to that of the higher symmetry hexacoordinated pseudooctahedral geometry of the hydrated or pyridine coordinated clusters. However, while an absence of coordination (i.e., activated framework) is signified by a higher intensity pre-edge feature, there are only very minor differences between spectra of MIL100(Fe) vs MIL100(Fe)-Py. Analogously subtle pre-

edge feature differences are also observed for the reference complexes containing these axially coordinated ligands. In both cases, the split quadrupole allowed $1s \rightarrow 3d$ pre-edge feature, typical for high spin Fe^{3+} systems with approximate octahedral coordination,⁸¹ exhibits a slightly higher intensity ratio of the high to low energy components for the water coordinated versions. The spectral difference is somewhat more pronounced for the complexes since they are not complicated by contributions from hydroxyl coordinated iron sites, as is the case for the MIL100(Fe) systems. When propylene is introduced to the activated framework, the intensity decreases in the XANES pre-edge feature, compared to that of MIL100(Fe)-Act, indicates weak interaction of the propylene guest molecules with the open Fe sites of the trinuclear clusters.

With analogous local coordination environments, the trinuclear iron complexes and MIL100(Fe) systems exhibit similar EXAFS spectra (Figure. 2.6, bottom), as expected. The different axial ligand environments for both complexes and MOFs yield some differences in EXAFS peak amplitudes but negligible differences in their positions. The spectra of the reference complexes were analyzed using models derived from their known structures, and the resulting fits are reasonable and consistent with the crystallographic data, shown in Figures 2.8 and 2.9. The corresponding fitting parameters are presented in Tables 2.1 and 2.2.

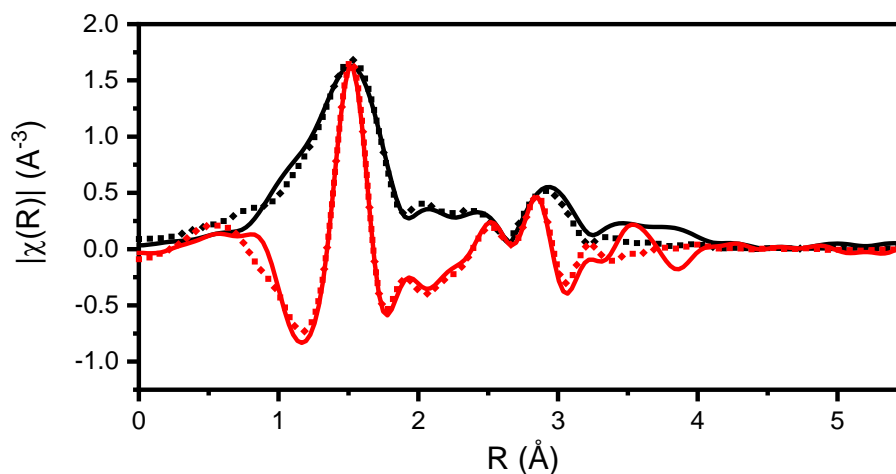


Figure 2.8: Fe K-edge EXAFS spectra of Fe₃OBzPy (black, solid) and fit (black, dotted) and the real component of Fe₃OBzPy (red, solid) and fit (red, dotted)

Table 2.1: EXAFS Fitting Parameters and comparison with crystallographic data^a for Fe₃OBzPy

Path	CN	R _{cryst} (Å) ^a	R _{fit} (Å)	σ ²
Fe-O _{μ3}	1	1.91(5)	1.93(3) ± 0.018(0)	0.002 ± 0.005
Fe-O _{equatorial}	4	2.01(4)	2.03(3) ± 0.01(9)	0.005 ± 0.002
Fe-N _{pyridine}	1	2.20(5)	2.22(6) ± 0.02(1)	0.010 ± 0.004
Fe-C _{carboxylate}	4	3.02(7)	3.01(5) ± 0.03(7)	0.006 ± 0.005
Fe-Fe	2	3.31(7)	3.33(0) ± 0.02(3)	0.007 ± 0.003

^a Distances obtained from crystal structure reported in ref 65,
 $S\sigma^2=0.92$ and E^0 was 4.077 eV for all paths
 $R=0.02$

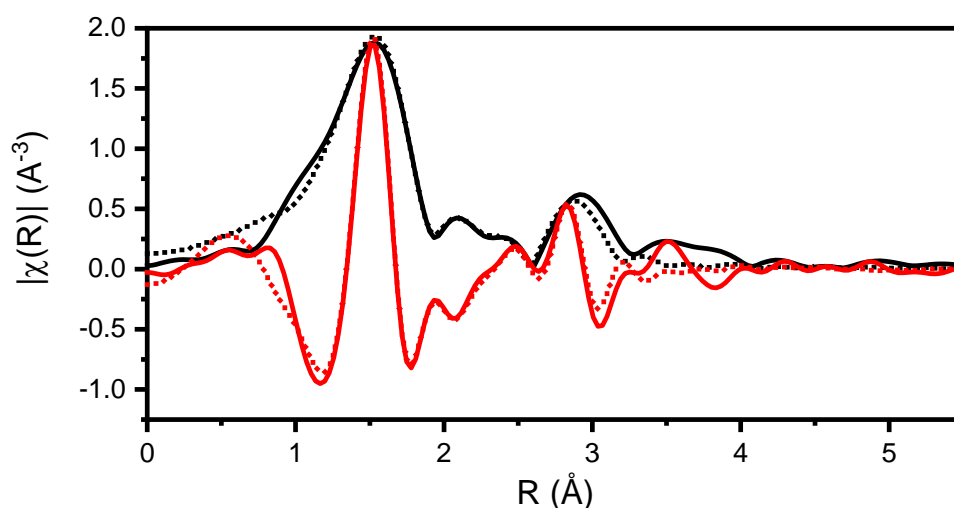


Figure 2.9: Fe K-edge EXAFS spectra of Fe₃OBz (black, solid) and fit (black,dotted) and the real component of Fe₃OBz (red, solid) and fit (red,dotted)

Table 2.2: EXAFS Fitting Parameters comparison with crystallographic data^a for Fe₃OBz

Path	CN	R _{cryst} (Å) ^a	R _{fit} (Å)	σ ²
Fe-O _{μ3}	1	1.90(0)	1.90(4) ± 0.01(8)	0.001 ± 0.005
Fe-O _{equatorial}	4	2.01(6)	2.02(0) ± 0.01(9)	0.004 ± 0.002
Fe-O _{water}	1	2.08(5)	2.08(9) ± 0.02(0)	0.002 ± 0.007
Fe-C _{carboxylate}	4	3.01(9)	2.97(9) ± 0.04(4)	0.009 ± 0.007
Fe-Fe	2	3.29(2)	3.30(7) ± 0.02(0)	0.006 ± 0.002

^aDistances obtained from crystal structure from ref 69

S_o²=0.98 and E⁰=5.1475 eV for all paths

R= 0.02

The MOF systems however do not benefit from this a priori crystallographic structure knowledge for all the ligand guest environments and consequently lead to severely underdefined fitting scenarios. EXAFS peak amplitude differences may reflect changes in metal coordination number (such as coordinated solvent loss resulting from MOF activation) but other factors such as scattering path disorder and interference play a role as well. Scattering paths arising from the μ₃ and carboxylate oxygens of the core cluster, as well as the axially coordinated/interacting guest (i.e., OH⁻, H₂O, pyridine, or

propylene), all contribute to this first shell peak, which severely hinders deconvolution of the individual paths through conventional EXAFS fitting.

These results highlight the major shortcomings of XAS characterization of host/guest interactions in most MOF materials. The weak XANES pre-edge features provide electronic and geometric insights on metal sites but deconvoluting the subtle intensity changes associated with minor differences in metal coordination is often complicated by strong overlap with the rising absorption edge. Moreover, these subtle pre-edge differences can be difficult to accurately model through computational means, as TDDFT methods are required. This is particularly true for multinuclear open shell transition metal-based systems, such as the MOF and reference complexes in this work. While traditional EXAFS analysis is often used to detect local metal coordination environment, this method is relatively insensitive to differences in atomic number for neighboring atoms within a given coordination shell and is further complicated by ambiguities in coordination number and disorder. These limitations can be a challenge for probing MOF adsorption processes since the coordination of the metal sites with both the linkers of the framework and the adsorbed guest molecules often involves this same set of similar atomic number neighboring atoms, i.e., C, O, and N, and the disorder of the bound guest species is usually unknown or difficult to assess.

2.3.1.3 X-ray emission spectroscopy

Vtc-XES, as a complementary X-ray characterization technique, can offer finer insight on these types of metal coordination environments. Vtc emission arises when the

electron originates from occupied valence orbitals and radiatively decays to the core-hole vacancy created on the absorbing metal. The vtc satellite features of the $K\beta$ emission line, specifically $K\beta_{2,5}$ and $K\beta''$, are of greatest interest for 3rd row transition metal-based systems, including the iron-based MOFs and complexes studied in this work. These emission lines stem from valence electron decay to the metal 1s core hole level. Intensity is derived through metal 4p contribution to the valence orbitals typically possessing metal 3d and significant ligand ns, np character. Consequently, since these orbitals reflect the chemical environment of the absorbing metal, vtc-XES is exceptionally sensitive to subtle electronic structure differences of the coordinated ligands.

Vtc-XES data collected for Fe_3OBz and $Fe_3OBz-Py$ (Figure. 2.10) illustrate the spectral differences associated with pyridine vs water coordination at each iron site. The $K\beta_{2,5}$ band clearly exhibits a higher intensity feature at 7107.9 eV for Fe_3OBzPy compared to the 7104.9 eV peak maximum of Fe_3OBz . A similar spectral trend is observed for the analogous pyridine versus water-loaded MOF systems, also shown in Figure. 2.10 along with their corresponding difference spectra. The difference in this case is not as prominent, which may be due to the slight variation of iron coordination at different node sites in the MIL100(Fe) framework⁶⁰ as well as the presence of hydroxyl coordination on one of the three iron sites as indicated by the DFT calculations discussed below.

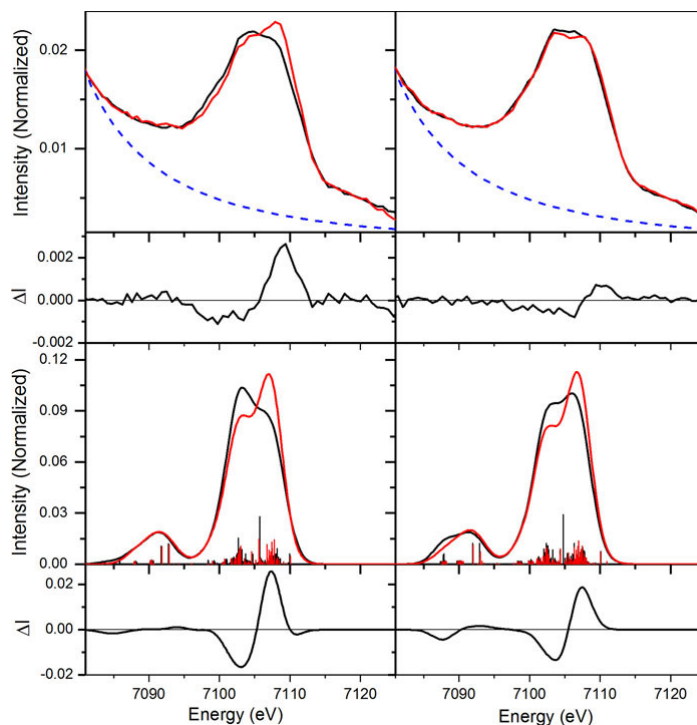


Figure 2.10 Experimental (top row) and theoretical (bottom row) $K\beta$ vtc-XES spectra of (left) Fe_3OBz (black) and Fe_3OBzPy (red), and (right) MIL100(Fe) (black) and MIL100(Fe)-Py (red). Corresponding difference spectra are plotted below each overlaid pair. Dashed blue lines indicate baseline arising from the tail of the $K\beta_{1,3}$ mainline feature. All XES spectra are normalized to unit area over the vtc region (see text for details).

DFT molecular orbital calculations, using crystal structure-derived geometries, allow us to interpret the experimentally observed differences in the $K\beta_{2,5}$ spectral features of the water- vs. pyridine-containing complexes and MOFs (Figure. 2.10, bottom). To account for the contribution of the different iron sites within the trinuclear clusters, spectra were calculated for the transitions localized on each iron site (Figures. 2.12-2.13) and averaged to generate the overall XES spectra for comparison with experimental results. Figure 2.11 depicts the states with orbital parentage involved in the calculated

transitions that contribute most to the overall shape of the vtc emission bands for the two model complexes. Accordingly, transitions from orbitals with significant benzoate ligand character are calculated to contribute to both high and low energy regions of the $K\beta_{2,5}$ feature. However, transitions from orbitals with the strongest mixing with the terminal H_2O ligand (i.e., Fe_3OBz orbitals shown in Figure. 2.11, left) are calculated to occur on average at lower energy than those involving orbitals with dominant pyridine ligand character (i.e., Fe_3OBzPy orbitals shown in Figure. 2.11, right). These results confirm that the relative intensity differences within the $K\beta_{2,5}$ band are diagnostic of the different axially coordinated ligands in these complexes.

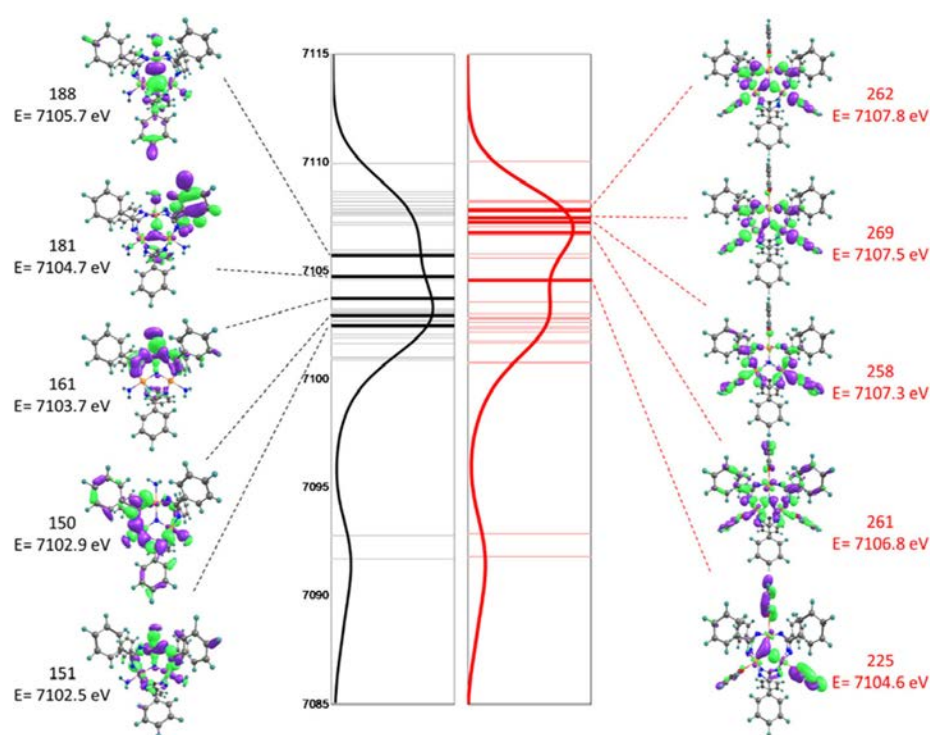


Figure 2.11 Energy level diagrams for Fe_3OBz (black) and Fe_3OBzPy (red) overlaid with the corresponding theoretical spectra. States with calculated oscillator strength of at least 0.45 are included. Those with significant axial ligand contributions to their orbital parentage are shown in bold along with the associated rendered

A similar trend is revealed by the calculations using trinuclear structural models of the water and pyridine ligated nodes of the MOFs derived from the MIL100(Fe) crystal structure, in which, two iron sites coordinate either water or pyridine and the third iron site is coordinated with a hydroxyl group. Shown in Figure 2.13, the presence of the pyridine ligand yields a spectrum with a more prominent higher energy $K\beta_{2,5}$ feature relative to that calculated for the hydrated structure. In both models, transitions from orbitals involving the iron-bound hydroxyl ligand also contribute to the higher energy side of the $K\beta_{2,5}$ band and the shorter Fe-O bond length predicts increased contribution to the overall intensity, shown in Figure 2.12.

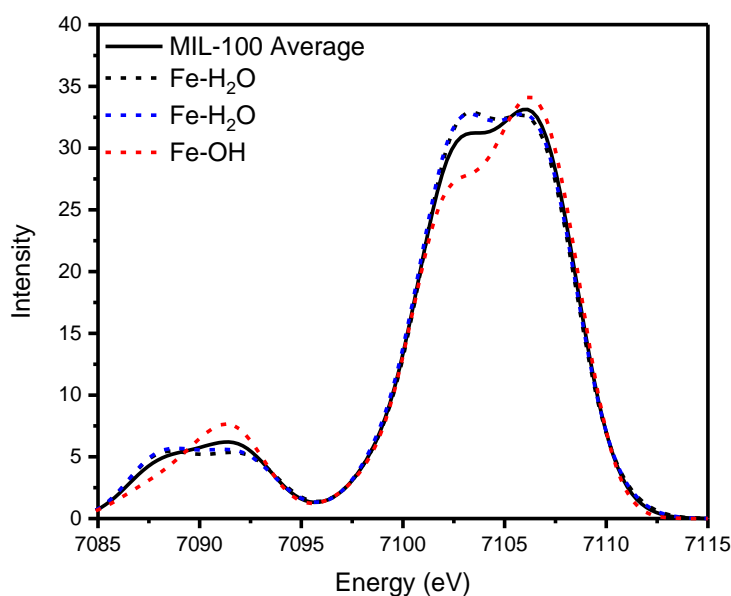


Figure 2.12: Calculated vtc-XES spectrum of MIL100(Fe) localized on each individual iron site (dotted lines) to generate the averaged overall spectrum (solid, black line)

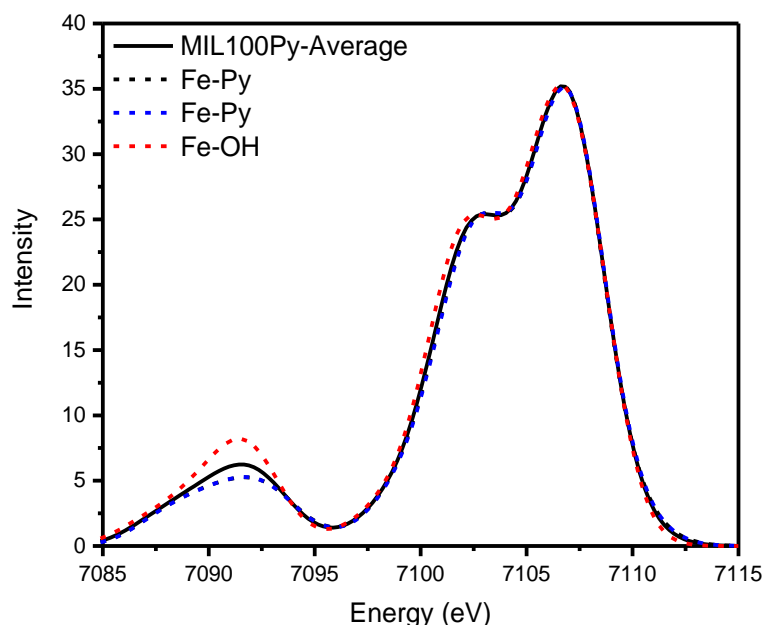


Figure 2.13: Calculated vtc-XES spectrum of MIL100(Fe)Py localized on each individual iron site (dotted lines) to generate the averaged overall spectrum (solid, black line)

This may partially explain the more subtle difference in bandshape observed experimentally for the MOF spectra since both frameworks have this ligand in common for one of the three Fe sites.

Notably, while the $K\beta''$ peak energy and intensity are often predictively associated with the chemical nature and bond length of the ligand environment, it tends to be dominated by transitions involving significant ligand s-character.³⁴ For the trinuclear Fe-based MOFs and complexes in this study, the calculated $K\beta''$ band derives most of its intensity from transitions involving the μ_3 -oxygen s-orbital and minimal s-orbital contribution from the other ligands. While some intensity is observed experimentally in

this crossover peak region for both complexes and MOF systems, uncertainties in baseline subtraction coupled with predicted insignificant differences between the two spectra prohibit further interpretation of this already very weak feature.

MIL100(Fe) and MIL100(Fe)-Py are good systems to demonstrate the efficacy of using vtc-XES to probe local metal coordination environment including binding with water or pyridine guest molecules because the spectra of convenient model complexes can be measured and calculated with reasonable accuracy to aid spectral interpretation. This is not the case for the other MOF guest environments, MIL100(Fe)-Act, which contains coordinatively unsaturated metal sites, and MIL100(Fe)-Prop, which contains weakly interacting propylene molecules at the available metal sites. These iron coordination environments cannot be replicated in stable molecular complexes or easily modeled computationally using DFT geometry optimization methods. Nevertheless, vtc-XES spectra were measured for the MOFs with these more elusive guest environments for comparison. Figure 2.14 depicts overlays of the vtc-XES spectra of MIL100(Fe), MIL100(Fe)-Py, and MIL100(Fe)-Prop with that of MIL100(Fe)-Act, along with the corresponding difference spectra derived from each pair. Subtle yet statistically relevant differences among these spectra are observed as indicated by the error analysis results summarized in Table 2.3. With all else equal, these differences can only arise from the disparity in Fe coordination, i.e., the contribution of the different axially bound species (water, pyridine, or propylene) in each case. The shift in the difference spectra peak can be used to identify variations in ligand environment with similar atomic number neighboring atoms. The preceding discussion of DFT-aided assignments for the features of the water vs pyridine containing systems explains the shift of the difference spectra

observed for MIL100(Fe) and MIL100(Fe)-Py. While spectral changes can be resolved for MIL100(Fe)-Prop compared to MIL100(Fe)-Act, indicating the presence of the axially interacting propylene guest, further interpretation of the difference spectrum is limited by the lack of analogous propylene ligated reference complex and DFT calculations.

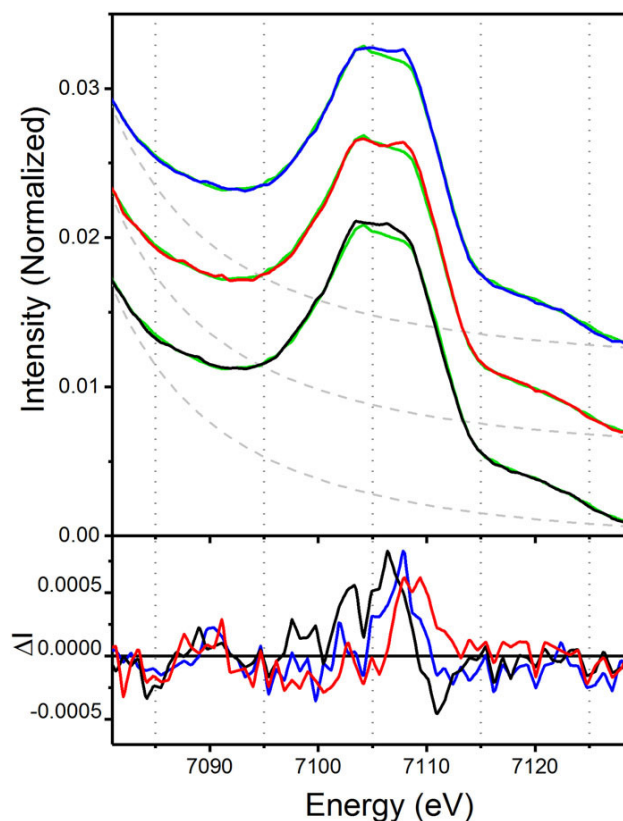


Figure 2.14 Top: Experimental vtc-XES spectra of MIL100(Fe) (black), MIL100(Fe)-Py (red), and MIL100(Fe)-Prop each overlaid with MIL100(Fe)-Act (green). Baseline arising from the tail of the $K\beta_{1,3}$ mainline feature shown as dashed gray lines. Vertical offset included for clarity. Bottom: Corresponding difference spectra associated with each overlaid pair of spectra from the top graph.

Table 2.3: vtc-XES Error Analysis

Sample	SNR^a
MIL100	3.46×10^2
MIL100Py	3.22×10^2
MIL100Prop	3.56×10^2
MIL100Act	3.53×10^2
Fe ₃ OBz	4.60×10^2
Fe ₃ OBzPy	3.75×10^2

$$^a SNR = \sqrt{N} \times \frac{\bar{x}}{\sigma}$$

where N =number of scans , \bar{x} = average signal, and σ =standard deviation of the signal (noise)

2.4 Conclusion

The examples in this study illustrate the advantages of using multiple complementary spectroscopy techniques for distinguishing subtle differences in MOF coordination environments but emphasize the need for model systems for more complete interpretation. Raman spectroscopy was used to reveal the presence of the different guest species in the frameworks and in the case of pyridine, provided strong evidence for its interaction at the metal node sites. The lack of unambiguous changes in framework-localized modes with varying metal coordination, however, warranted further evaluation using the more element specific techniques of X-ray absorption and emission spectroscopy to distinguish the metal ligation in these systems. While the nearly identical Fe coordination environments of the two reference complexes, Fe₃OBz and Fe₃OBzPy, lead to subtle XAS differences that are difficult to deconvolute using conventional analysis techniques, they can be distinguished by ligand-sensitive vtc-XES along with DFT computational support. As molecular models for the nodes in MIL100(Fe), these systems helped explain the vtc-XES spectra observed for the MOFs with water and pyridine guest environments compared to one another and the activated framework.

While the vtc-XES spectrum of the propylene treated MOF was distinguishable from those of the other MOF environments, suitable experimental or computational models were not available in this case to conclusively link the specific spectral differences with propylene guest interaction at the metal sites. This first nonresonant $K\beta$ vtc-XES investigation of MOF adsorption behavior illustrates the advantages and complementarity with conventional XAS and vibrational spectroscopy characterization and will serve as a benchmark for future applications to these and other porous hybrid materials for a better understanding of their host–guest properties.

2.5 References

1. Cui, Y.; Li, B.; He, H.; Zhou, W.; Chen, B.; Qian, G., Metal–Organic Frameworks as Platforms for Functional Materials. *Accounts of Chemical Research* **2016**, 49 (3), 483-493.
2. Dhakshinamoorthy, A.; Asiri Abdullah, M.; Garcia, H., Metal–Organic Frameworks as Catalysts for Oxidation Reactions. *Chemistry – A European Journal* **2016**, 22 (24), 8012-8024.
3. Foo, M. L.; Matsuda, R.; Kitagawa, S., Functional Hybrid Porous Coordination Polymers. *Chemistry of Materials* **2014**, 26 (1), 310-322.
4. Li, B.; Wen, H.-M.; Cui, Y.; Zhou, W.; Qian, G.; Chen, B., Emerging Multifunctional Metal–Organic Framework Materials. *Advanced Materials* **2016**, 28 (40), 8819-8860.
5. Stassen, I.; Burtch, N.; Talin, A.; Falcaro, P.; Allendorf, M.; Ameloot, R., An Updated Roadmap for the Integration of Metal-Organic Frameworks with Electronic Devices and Chemical Sensors. *Chemical Society Reviews* **2017**, 46 (11), 3185-3241.
6. Wang, C.; Liu, D.; Lin, W., Metal–Organic Frameworks as A Tunable Platform for Designing Functional Molecular Materials. *Journal of the American Chemical Society* **2013**, 135 (36), 13222-13234.
7. Wu, C.-D.; Zhao, M., Incorporation of Molecular Catalysts in Metal–Organic Frameworks for Highly Efficient Heterogeneous Catalysis. *Advanced Materials* **2017**, 29 (14), 1605446.
8. Wang, S.; Wang, X., Multifunctional Metal–Organic Frameworks for Photocatalysis. *Small* **2015**, 11 (26), 3097-3112.
9. Nijem, N.; Chabal, Y. J., Adsorbate Interactions in Metal Organic Frameworks Studied by Vibrational Spectroscopy. *Comments on Inorganic Chemistry* **2014**, 34 (3-4), 78-102.
10. Nijem, N.; Veyan, J.-F.; Kong, L.; Wu, H.; Zhao, Y.; Li, J.; Langreth, D. C.; Chabal, Y. J., Molecular Hydrogen "Pairing" Interaction in a Metal Organic Framework System with Unsaturated Metal Centers (MOF-74). *Journal of the American Chemical Society* **2010**, 132 (Copyright (C) 2011 American Chemical Society (ACS). All Rights Reserved.), 14834-14848.
11. Noei, H.; Kozachuk, O.; Amirjalayer, S.; Bureekaew, S.; Kauer, M.; Schmid, R.; Marler, B.; Muhler, M.; Fischer, R. A.; Wang, Y., CO Adsorption on a Mixed-Valence Ruthenium Metal–Organic Framework Studied by UHV-FTIR Spectroscopy and DFT Calculations. *The Journal of Physical Chemistry C* **2013**, 117 (11), 5658-5666.
12. Tan, K.; Canepa, P.; Gong, Q.; Liu, J.; Johnson, D. H.; Dyevoich, A.; Thallapally, P. K.; Thonhauser, T.; Li, J.; Chabal, Y. J., Mechanism of Preferential Adsorption of SO₂ into Two Microporous Paddle Wheel Frameworks M(bdc)(ted)_{0.5}. *Chemistry of Materials* **2013**, 25 (23), 4653-4662.
13. Chen, Y.; Zhang, J.; Li, J.; Lockard, J. V., Monitoring the Activation of a Flexible Metal–Organic Framework Using Structurally Sensitive Spectroscopy Techniques. *The Journal of Physical Chemistry C* **2013**, 117 (39), 20068-20077.
14. Nijem, N.; Thissen, P.; Yao, Y.; Longo, R. C.; Roodenko, K.; Wu, H.; Zhao, Y.; Cho, K.; Li, J.; Langreth, D. C.; Chabal, Y. J., Understanding the Preferential Adsorption

- of CO₂ over N₂ in a Flexible Metal–Organic Framework. *Journal of the American Chemical Society* **2011**, *133* (32), 12849-12857.
15. Strauss, I.; Mundstock, A.; Hinrichs, D.; Himstedt, R.; Knebel, A.; Reinhardt, C.; Dorfs, D.; Caro, J., The Interaction of Guest Molecules with Co-MOF-74: A Vis/NIR and Raman Approach. *Angewandte Chemie International Edition* **2018**, *57* (25), 7434-7439.
 16. Comito, R. J.; Metzger, E. D.; Wu, Z.; Zhang, G.; Hendon, C. H.; Miller, J. T.; Dincă, M., Selective Dimerization of Propylene with Ni-MFU-4l. *Organometallics* **2017**, *36* (9), 1681-1683.
 17. Falkowski, J. M.; Sawano, T.; Zhang, T.; Tsun, G.; Chen, Y.; Lockard, J. V.; Lin, W., Privileged Phosphine-Based Metal–Organic Frameworks for Broad-Scope Asymmetric Catalysis. *Journal of the American Chemical Society* **2014**, *136* (14), 5213-5216.
 18. Ji, P.; Song, Y.; Drake, T.; Veroneau, S. S.; Lin, Z.; Pan, X.; Lin, W., Titanium(III)-Oxo Clusters in a Metal–Organic Framework Support Single-Site Co(II)-Hydride Catalysts for Arene Hydrogenation. *Journal of the American Chemical Society* **2018**, *140* (1), 433-440.
 19. Manna, K.; Ji, P.; Lin, Z.; Greene, F. X.; Urban, A.; Thacker, N. C.; Lin, W., Chemoselective Single-Site Earth-Abundant Metal Catalysts at Metal–Organic Framework Nodes. *Nature Communications* **2016**, *7*, 12610.
 20. Sawano, T.; Lin, Z.; Boures, D.; An, B.; Wang, C.; Lin, W., Metal–Organic Frameworks Stabilize Mono(phosphine)–Metal Complexes for Broad-Scope Catalytic Reactions. *Journal of the American Chemical Society* **2016**, *138* (31), 9783-9786.
 21. Stubbs, A. W.; Braglia, L.; Borfecchia, E.; Meyer, R. J.; Román-Leshkov, Y.; Lamberti, C.; Dincă, M., Selective Catalytic Olefin Epoxidation with MnII-Exchanged MOF-5. *ACS Catalysis* **2018**, *8* (1), 596-601.
 22. Xiao, C.; Goh, T. W.; Brashler, K.; Pei, Y.; Guo, Z.; Huang, W., In Situ X-ray Absorption Spectroscopy Studies of Kinetic Interaction between Platinum(II) Ions and UiO-66 Series Metal–Organic Frameworks. *The Journal of Physical Chemistry B* **2014**, *118* (49), 14168-14176.
 23. Bonino, F.; Chavan, S.; Vitillo, J. G.; Groppo, E.; Agostini, G.; Lamberti, C.; Dietzel, P. D. C.; Prestipino, C.; Bordiga, S., Local Structure of CPO-27-Ni Metallorganic Framework upon Dehydration and Coordination of NO. *Chemistry of Materials* **2008**, *20* (15), 4957-4968.
 24. Prestipino, C.; Regli, L.; Vitillo, J. G.; Bonino, F.; Damin, A.; Lamberti, C.; Zecchina, A.; Solari, P. L.; Kongshaug, K. O.; Bordiga, S., Local Structure of Framework Cu(II) in HKUST-1 Metallorganic Framework: Spectroscopic Characterization upon Activation and Interaction with Adsorbates. *Chemistry of Materials* **2006**, *18* (5), 1337-1346.
 25. Rossin, A.; Di Credico, B.; Giambastiani, G.; Peruzzini, M.; Pescitelli, G.; Reginato, G.; Borfecchia, E.; Gianolio, D.; Lamberti, C.; Bordiga, S., Synthesis, Characterization and CO₂ Uptake of a Chiral Co(II) Metal-Organic Framework Containing a Thiazolidine-Based Spacer. *Journal of Materials Chemistry* **2012**, *22* (20), 10335-10344.
 26. Chavan, S.; Bonino, F.; Vitillo, J. G.; Groppo, E.; Lamberti, C.; Dietzel, P. D. C.; Zecchina, A.; Bordiga, S., Response of CPO-27-Ni Towards CO, N₂ and C₂H₄. *Physical Chemistry Chemical Physics* **2009**, *11* (42), 9811-9822.

27. Tulchinsky, Y.; Hendon, C. H.; Lomachenko, K. A.; Borfecchia, E.; Melot, B. C.; Hudson, M. R.; Tarver, J. D.; Korzyński, M. D.; Stubbs, A. W.; Kagan, J. J.; Lamberti, C.; Brown, C. M.; Dincă, M., Reversible Capture and Release of Cl₂ and Br₂ with a Redox-Active Metal–Organic Framework. *Journal of the American Chemical Society* **2017**, *139* (16), 5992-5997.
28. Brozek, C. K.; Miller, J. T.; Stoian, S. A.; Dincă, M., NO Disproportionation at a Mononuclear Site-Isolated Fe²⁺ Center in Fe²⁺-MOF-5. *Journal of the American Chemical Society* **2015**, *137* (23), 7495-7501.
29. Kucheryavy, P.; Lahanas, N.; Lockard, J. V., Spectroscopic Interrogations of Isostructural Metalloporphyrin-Based Metal–Organic Frameworks with Strongly and Weakly Coordinating Guest Molecules. *Journal of Coordination Chemistry* **2016**, *69*, 1780-1791.
30. Kucheryavy, P.; Lahanas, N.; Velasco, E.; Sun, C.-J.; Lockard, J. V., Probing Framework-Restricted Metal Axial Ligation and Spin State Patterns in a Post-Synthetically Reduced Iron-Porphyrin-Based Metal–Organic Framework. *The Journal of Physical Chemistry Letters* **2016**, *7*, 1109-1115.
31. Bauer, M., HERFD-XAS and Valence-to-core-XES: New Tools to Push the Limits in Research with Hard X-rays? *Physical Chemistry Chemical Physics* **2014**, *16* (27), 13827-13837.
32. Bergmann, U.; Glatzel, P., X-ray Emission Spectroscopy. *Photosynthesis Research* **2009**, *102* (2), 255.
33. Bergmann, U.; Glatzel, P.; Robblee, J. H.; Messinger, J.; Fernandez, C.; Cinco, R.; Visser, H.; McFarlane, K.; Bellacchio, E.; Pizarro, S.; Sauer, K.; Yachandra, V. K.; Klein, M. P.; Cox, B. L.; Nealon, K. H.; Cramer, S. P., High-resolution X-ray Spectroscopy of Rare Events: A Different Look at Local Structure and Chemistry. *Journal of Synchrotron Radiation* **2001**, *8* (2), 199-203.
34. Bergmann, U.; Horne, C. R.; Collins, T. J.; Workman, J. M.; Cramer, S. P., Chemical Dependence of Interatomic X-ray Transition Energies and Intensities – a Study of Mn Kβ⁰ and Kβ_{2,5} Spectra. *Chemical Physics Letters* **1999**, *302* (1–2), 119-124.
35. Gallo, E.; Glatzel, P., Valence to Core X-ray Emission Spectroscopy. *Advanced Materials* **2014**, *26* (46), 7730-7746.
36. Pollock, C. J.; DeBeer, S., Valence-to-Core X-ray Emission Spectroscopy: A Sensitive Probe of the Nature of a Bound Ligand. *Journal of the American Chemical Society* **2011**, *133* (14), 5594-5601.
37. Pollock, C. J.; DeBeer, S., Insights into the Geometric and Electronic Structure of Transition Metal Centers from Valence-to-Core X-ray Emission Spectroscopy. *Accounts of Chemical Research* **2015**, *48* (11), 2967-2975.
38. Beckwith, M. A.; Roemelt, M.; Collomb, M.-N. I.; DuBoc, C.; Weng, T.-C.; Bergmann, U.; Glatzel, P.; Neese, F.; DeBeer, S., Manganese Kβ X-ray Emission Spectroscopy As a Probe of Metal–Ligand Interactions. *Inorganic Chemistry* **2011**, *50* (17), 8397-8409.
39. Delgado-Jaime, M. U.; DeBeer, S.; Bauer, M., Valence-to-Core X-Ray Emission Spectroscopy of Iron–Carbonyl Complexes: Implications for the Examination of Catalytic Intermediates. *Chemistry – A European Journal* **2013**, *19* (47), 15888-15897.
40. Hugenbruch, S.; Shafaat, H. S.; Kramer, T.; Delgado-Jaime, M. U.; Weber, K.; Neese, F.; Lubitz, W.; DeBeer, S., In Search of Metal Hydrides: an X-ray Absorption and

Emission Study of [NiFe] Hydrogenase Model Complexes. *Physical Chemistry Chemical Physics* **2016**, *18* (16), 10688-10699.

41. Lee, N.; Petrenko, T.; Bergmann, U.; Neese, F.; DeBeer, S., Probing Valence Orbital Composition with Iron K β X-ray Emission Spectroscopy. *Journal of the American Chemical Society* **2010**, *132* (28), 9715-9727.
42. Pollock, C. J.; Lancaster, K. M.; Finkelstein, K. D.; DeBeer, S., Study of Iron Dimers Reveals Angular Dependence of Valence-to-Core X-ray Emission Spectra. *Inorganic Chemistry* **2014**, *53* (19), 10378-10385.
43. Pushkar, Y.; Long, X.; Glatzel, P.; Brudvig Gary, W.; Dismukes, G. C.; Collins Terrence, J.; Yachandra Vittal, K.; Yano, J.; Bergmann, U., Direct Detection of Oxygen Ligation to the Mn₄Ca Cluster of Photosystem II by X-ray Emission Spectroscopy. *Angewandte Chemie International Edition* **2010**, *49* (4), 800-803.
44. Schwalenstocker, K.; Paudel, J.; Kohn, A. W.; Dong, C.; Van Heuvelen, K. M.; Farquhar, E. R.; Li, F., Cobalt K β Valence-to-Core X-ray Emission Spectroscopy: A Study of Low-Spin Octahedral Cobalt(III) Complexes. *Dalton Transactions* **2016**, *45* (36), 14191-14202.
45. Smolentsev, G.; Soldatov, A. V.; Messinger, J.; Merz, K.; Weyhermüller, T.; Bergmann, U.; Pushkar, Y.; Yano, J.; Yachandra, V. K.; Glatzel, P., X-ray Emission Spectroscopy To Study Ligand Valence Orbitals in Mn Coordination Complexes. *Journal of the American Chemical Society* **2009**, *131* (36), 13161-13167.
46. Kowalska, J.; DeBeer, S., The role of X-ray spectroscopy in understanding the geometric and electronic structure of nitrogenase. *Biochimica et Biophysica Acta (BBA) - Molecular Cell Research* **2015**, *1853* (6), 1406-1415.
47. Lancaster, K. M.; Roemelt, M.; Ettenhuber, P.; Hu, Y.; Ribbe, M. W.; Neese, F.; Bergmann, U.; DeBeer, S., X-ray Emission Spectroscopy Evidences a Central Carbon in the Nitrogenase Iron-Molybdenum Cofactor. *Science* **2011**, *334* (6058), 974.
48. Martin-Diaconescu, V.; Chacón, K. N.; Delgado-Jaime, M. U.; Sokaras, D.; Weng, T.-C.; DeBeer, S.; Blackburn, N. J., K β Valence to Core X-ray Emission Studies of Cu(I) Binding Proteins with Mixed Methionine – Histidine Coordination. Relevance to the Reactivity of the M- and H-sites of Peptidylglycine Monooxygenase. *Inorganic Chemistry* **2016**, *55* (7), 3431-3439.
49. Boubnov, A.; Carvalho, H. W. P.; Doronkin, D. E.; Günter, T.; Gallo, E.; Atkins, A. J.; Jacob, C. R.; Grunwaldt, J.-D., Selective Catalytic Reduction of NO Over Fe-ZSM-5: Mechanistic Insights by Operando HERFD-XANES and Valence-to-Core X-ray Emission Spectroscopy. *Journal of the American Chemical Society* **2014**, *136* (37), 13006-13015.
50. Giordanino, F.; Borfecchia, E.; Lomachenko, K. A.; Lazzarini, A.; Agostini, G.; Gallo, E.; Soldatov, A. V.; Beato, P.; Bordiga, S.; Lamberti, C., Interaction of NH₃ with Cu-SSZ-13 Catalyst: A Complementary FTIR, XANES, and XES Study. *The Journal of Physical Chemistry Letters* **2014**, *5* (9), 1552-1559.
51. Lomachenko, K. A.; Borfecchia, E.; Negri, C.; Berlier, G.; Lamberti, C.; Beato, P.; Falsig, H.; Bordiga, S., The Cu-CHA deNO_x Catalyst in Action: Temperature-Dependent NH₃-Assisted Selective Catalytic Reduction Monitored by Operando XAS and XES. *Journal of the American Chemical Society* **2016**, *138* (37), 12025-12028.
52. Zhang, R.; Li, H.; McEwen, J.-S., Chemical Sensitivity of Valence-to-Core X-ray Emission Spectroscopy Due to the Ligand and the Oxidation State: A Computational

Study on Cu-SSZ-13 with Multiple H₂O and NH₃ Adsorption. *The Journal of Physical Chemistry C* **2017**, *121* (46), 25759-25767.

53. Bordiga, S.; Groppo, E.; Agostini, G.; van Bokhoven, J. A.; Lamberti, C., Reactivity of Surface Species in Heterogeneous Catalysts Probed by In Situ X-ray Absorption Techniques. *Chemical Reviews* **2013**, *113* (3), 1736-1850.
54. Liu, Y.; Eubank, J. F.; Cairns, A. J.; Eckert, J.; Kravtsov, V. C.; Luebke, R.; Eddaoudi, M., Assembly of Metal–Organic Frameworks (MOFs) Based on Indium-Trimer Building Blocks: A Porous MOF with soc Topology and High Hydrogen Storage. *Angewandte Chemie International Edition* **2007**, *46* (18), 3278-3283.
55. Serre, C.; Mellot-Draznieks, C.; Surblé, S.; Audebrand, N.; Filinchuk, Y.; Férey, G., Role of Solvent-Host Interactions That Lead to Very Large Swelling of Hybrid Frameworks. *Science* **2007**, *315* (5820), 1828.
56. Serre, C.; Millange, F.; Surblé, S.; Férey, G., A Route to the Synthesis of Trivalent Transition-Metal Porous Carboxylates with Trimeric Secondary Building Units. *Angewandte Chemie International Edition* **2004**, *43* (46), 6285-6289.
57. Sudik, A. C.; Côté, A. P.; Yaghi, O. M., Metal-Organic Frameworks Based on Trigonal Prismatic Building Blocks and the New “acs” Topology. *Inorganic Chemistry* **2005**, *44* (9), 2998-3000.
58. Zhong, G.; Liu, D.; Zhang, J., Applications of Porous Metal–Organic Framework MIL-100(M) (M = Cr, Fe, Sc, Al, V). *Crystal Growth & Design* **2018**, *18* (12), 7730-7744.
59. Dhakshinamoorthy, A.; Alvaro, M.; Chevreau, H.; Horcajada, P.; Devic, T.; Serre, C.; Garcia, H., Iron(III) Metal–Organic Frameworks as Solid Lewis Acids for the Isomerization of α -Pinene Oxide. *Catalysis Science & Technology* **2012**, *2* (2), 324-330.
60. Horcajada, P.; Surble, S.; Serre, C.; Hong, D.-Y.; Seo, Y.-K.; Chang, J.-S.; Grenèche, J.-M.; Margiolaki, I.; Férey, G., Synthesis and Catalytic Properties of MIL-100(Fe), an Iron(III) Carboxylate with Large Pores. *Chemical Communications* **2007**, (27), 2820-2822.
61. Timofeeva, M. N.; Panchenko, V. N.; Prikhod'ko, S. A.; Ayupov, A. B.; Larichev, Y. V.; Khan, N. A.; Jhung, S. H., Metal-Organic Frameworks as Efficient Catalytic Systems for the Synthesis of 1,5-Benzodiazepines from 1,2-Phenylenediamine and Ketones. *Journal of Catalysis* **2017**, *354*, 128-137.
62. Zhang, F.; Shi, J.; Jin, Y.; Fu, Y.; Zhong, Y.; Zhu, W., Facile synthesis of MIL-100(Fe) under HF-free conditions and its application in the acetalization of aldehydes with diols. *Chemical Engineering Journal* **2015**, *259*, 183-190.
63. Leclerc, H.; Vimont, A.; Lavalley, J.-C.; Daturi, M.; Wiersum, A. D.; Llewellyn, P. L.; Horcajada, P.; Férey, G.; Serre, C., Infrared Study of the Influence of Reducible Iron(III) Metal Sites on the Adsorption of CO, CO₂, Propane, Propene and Propyne in the Mesoporous Metal-Organic Framework MIL-100. *Physical Chemistry Chemical Physics* **2011**, *13* (24), 11748-11756.
64. Yoon, J. W.; Seo, Y.-K.; Hwang, Y. K.; Chang, J.-S.; Leclerc, H.; Wuttke, S.; Bazin, P.; Vimont, A.; Daturi, M.; Bloch, E.; Llewellyn, P. L.; Serre, C.; Horcajada, P.; Grenèche, J.-M.; Rodrigues, A. E.; Férey, G., Controlled Reducibility of a Metal–Organic Framework with Coordinatively Unsaturated Sites for Preferential Gas Sorption. *Angewandte Chemie International Edition* **2010**, *49* (34), 5949-5952.

65. Sowrey, F. E.; Tilford, C.; Wocadlo, S.; Anson, C. E.; Powell, A. K.; Bennington, S. M.; Montfrooij, W.; Jayasooriya, U. A.; Cannon, R. D., Spin frustration and concealed asymmetry: structure and magnetic spectrum of $[\text{Fe}_3\text{O}(\text{O}_2\text{CPh})_6(\text{py})_3]\text{ClO}_4\cdot\text{py}$. *Journal of the Chemical Society, Dalton Transactions* **2001**, (6), 862-866.
66. Ravel, B.; Newville, M., ATHENA, ARTEMIS, HEPHAESTUS: Data Analysis for X-ray Absorption Spectroscopy Using IFEFFIT. *Journal of Synchrotron Radiation* **2005**, 12 (4), 537-541.
67. Georgopoulou, A. N.; Sanakis, Y.; Psycharis, V.; Raptopoulou, C. P.; Boudalis, A. K., Mössbauer Spectra of Two Extended Series of Basic Iron(III) Carboxylates $[\text{Fe}_3\text{O}(\text{O}_2\text{CR})_6(\text{H}_2\text{O})_6]\text{A}$ ($\text{A}^- = \text{ClO}_4^-$, NO_3^-). *Hyperfine Interactions* **2010**, 198 (1), 229-241.
68. Finkelstein, K. D.; Pollock, C. J.; Lyndaker, A.; Krawczyk, T.; Conrad, J., Dual-Array Valence Emission Spectrometer (DAVES): A New Approach for Hard X-ray Photon-in Photon-out Spectroscopies. *AIP Conference Proceedings* **2016**, 1741 (1), 030009.
69. Neese, F., The ORCA program system. *Wiley Interdisciplinary Reviews: Computational Molecular Science* **2012**, 2 (1), 73-78.
70. Neese, F., Software update: the ORCA program system, version 4.0. *Wiley Interdisciplinary Reviews: Computational Molecular Science* **2018**, 8 (1), e1327.
71. Weigend, F., Accurate Coulomb-fitting basis sets for H to Rn. *Physical Chemistry Chemical Physics* **2006**, 8 (9), 1057-1065.
72. Weigend, F.; Ahlrichs, R., Balanced basis sets of split valence, triple zeta valence and quadruple zeta valence quality for H to Rn: Design and assessment of accuracy. *Physical Chemistry Chemical Physics* **2005**, 7 (18), 3297-3305.
73. Lassalle-Kaiser, B.; Boron, T. T.; Krewald, V.; Kern, J.; Beckwith, M. A.; Delgado-Jaime, M. U.; Schroeder, H.; Alonso-Mori, R.; Nordlund, D.; Weng, T.-C.; Sokaras, D.; Neese, F.; Bergmann, U.; Yachandra, V. K.; DeBeer, S.; Pecoraro, V. L.; Yano, J., Experimental and Computational X-ray Emission Spectroscopy as a Direct Probe of Protonation States in Oxo-Bridged MnIV Dimers Relevant to Redox-Active Metalloproteins. *Inorganic Chemistry* **2013**, 52 (22), 12915-12922.
74. Chemcraft - Graphical Software for Visualization of Quantum Chemistry Computations <https://www.chemcraftprog.com>.
75. Kline, C. H.; Turkevich, J., The Vibrational Spectrum of Pyridine and the Thermodynamic Properties of Pyridine Vapors. *The Journal of Chemical Physics* **1944**, 12 (7), 300-309.
76. Akyüz, S.; Dempster, A. B.; Morehouse, R. L.; Suzuki, S., An infrared and Raman spectroscopic study of some metal pyridine tetracyanonickelate complexes. *Journal of Molecular Structure* **1973**, 17 (1), 105-125.
77. Stangret, J.; Savoie, R., Raman spectroscopic study of the interaction of metal ions with pyridine and maleimide — models for nucleic acids. *Journal of Molecular Structure* **1993**, 297, 91-102.
78. Johnson, M. K.; Powell, D. B.; Cannon, R. D., Vibrational spectra of carboxylato complexes—III. Trinuclear ‘basic’ acetates and formates of chromium(III), iron(III) and other transition metals. *Spectrochimica Acta Part A: Molecular Spectroscopy* **1981**, 37 (11), 995-1006.

79. Ananthakrishnan, R., The Raman Spectra of Propylene and ISO-Butane. *Proceedings of the Indian Academy of Sciences - Section A* **1936**, 3 (6), 527-532.
80. Moskovits, M.; Dilella, D. P., Enhanced raman spectra of ethylene and propylene adsorbed on silver. *Chemical Physics Letters* **1980**, 73 (3), 500-505.
81. Westre, T. E.; Kennepohl, P.; DeWitt, J. G.; Hedman, B.; Hodgson, K. O.; Solomon, E. I., A Multiplet Analysis of Fe K-Edge $1s \rightarrow 3d$ Pre-Edge Features of Iron Complexes. *Journal of the American Chemical Society* **1997**, 119 (27), 6297-6314.

Chapter 3. Long-Lived Photoinduced Charge Separation in a Trinuclear Iron- μ_3 -oxo-based Metal–Organic Framework

3.1 Introduction

The development of new heterogeneous photocatalytic materials is motivated by the need to address a number of urgent environmental and energy supply issues. From the remediation of air and water pollutants to harnessing solar energy for fuel production, much effort has been focused on large band gap semiconductor-based photocatalysts, like TiO_2 , that effectively limit the use of solar energy only to the UV spectral region.^{1–3} Dye sensitization of these materials is one heavily pursued avenue for improvement, but in many cases, reliance on nonabundant elements, such as ruthenium,^{4–6} limits the practicality of this approach. Consequently, alternative photocatalytic materials are being explored that extend the usable photon energy range into the visible region without simultaneously introducing high rates of photogenerated charge-carrier recombination (as would inevitably occur for low band gap semiconductor materials such as iron oxide). Moreover, solid-state materials with intrinsic porosity offer potentially improved control of photochemical reactivity through the use of confined spaces and increased surface areas. As an emerging class of porous solid-state materials, metal–organic frameworks (MOFs) with photoactive redox sites provide a promising route for incorporating these attributes for photocatalytic applications.

MOFs are a class of hybrid materials consisting of microporous crystalline networks of metal ions or clusters connected by organic molecules. The wide range of organic linkers available, combined with variable metal coordination chemistry, yields tunable 3D architectures with resulting properties ranging from selective gas adsorption

to catalysis.⁷⁻⁸ The potential utility of MOFs specifically for photocatalysis has been largely recognized,⁹⁻¹² with photoreaction sites often incorporated as linker units tailored for postsynthetic ligation of reactive metals.¹³⁻¹⁵ Alternatively, the metal nodes of the framework itself can potentially serve as catalytic sites, where the requisite charge separation can be initiated through photoinduced population of available ligand-to-metal charge transfer (LMCT) states.¹⁶⁻¹⁷ For example, a series of Fe(III)-MOFs, composed of Fe₃-μ₃-oxo clusters separated by linkers such as terephthalic acid, has been shown to exhibit visible-light photocatalytic behavior.¹⁸ Like other MOFs with potentially photoactive redox sites, photoinduced charge-separation events involving the Fe sites within the framework are believed responsible for initiating subsequent chemical processes. Kinetics derived from optical transient absorption (OTA) spectroscopy studies of these MOFs point to a long-lived excited state that may be generated through population of an initial LMCT excited state.¹⁹ However, the lack of resolved optical UV-vis absorption or clear OTA spectral signatures for the transient presence of the reduced iron-oxo cluster species or oxidized linker prevents a definitive charge-transfer assignment. Consequently, the true nature of the excited state in these MOFs, including the transient changes in metal oxidation state, remains unconfirmed.

In this chapter, we monitored the long-lived excited state in one of these Fe₃-μ₃-oxo-based MOFs with trimesic acid linkers, called MIL-100(Fe) (Figure 3.1), is explored using X-ray transient absorption (XTA) spectroscopy to aid in its assignment. This synchrotron-based technique involves laser-pump X-ray probe measurements to track excited-state geometric and electronic changes of metal-based systems in the picosecond to nanosecond time domain. Because of the element specificity, XTA has become an

important tool for investigating the photochemistry of both molecular²⁰⁻³⁰ and solid-state³¹⁻³⁴ metal-based systems, including a newly reported application to a porous zeolitic imidazolate framework (ZIF).³² Here Fe K-edge XTA is used to reveal the charge-transfer character of the excited state in MIL-100(Fe) that eludes detection by OTA. These measurements require a balance of both the optical and X-ray absorption cross sections of the material, which are quite different between these photon energy ranges. This mismatch is partly curtailed by reducing the particle size of the MOF samples used in this experiment. For this reason, MIL-100(Fe) is prepared as a colloidal nanoparticle suspension. Additionally, trinuclear iron carboxylate model complexes are measured by OTA and both XTA and steady-state X-ray absorption spectroscopy (XAS), which provide valuable comparisons for the unambiguous assignment of the charge-separated nature of the long-lived excited state in the MOF.

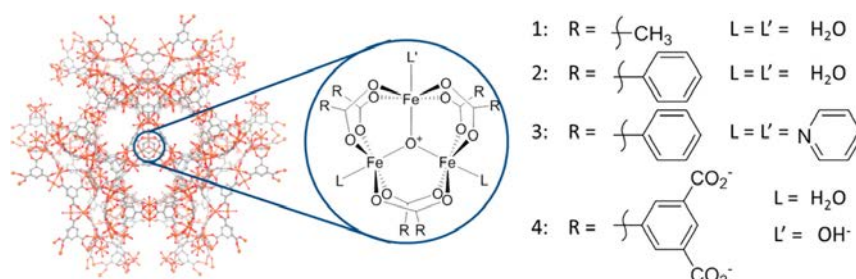


Figure 3.1. Left: MIL-100(Fe) structure. Right: μ_3 -oxo trinuclear iron core for reference complexes and MOF: 1: Fe₃O-Ac, 2: Fe₃O-Bz, 3: Fe₃O-BzPy, 4: MIL-100(Fe).

3.2 Experimental Methods

3.2.1 Materials and Synthesis

All solvents and starting materials, Fe(NO₃)₃·9 H₂O, 1,3,5-benzenetricarboxylic acid, glacial acetic acid, sodium hydroxide, FeCl₃·6 H₂O, FeCl₂·4 H₂O, benzoic acid, and

oleylamine (70%) were used without further purification, with the exception of pyridine (99%+), which was dried over molecular sieves prior to use.

MIL-100(Fe)-OA Oleylamine-coated MOF nanoparticles were synthesized following a modified literature procedure.³⁵ 3.03 g (10 mmol) of $\text{Fe}(\text{NO}_3)_3 \cdot 9 \text{H}_2\text{O}$, 1.89 g (9 mmol) of 1,3,5-benzenetricarboxylic acid, one drop of oleylamine, and 6 mL of Milli-Q water were mixed in a 25 mL round bottom flask. The reaction was stirred at 95°C for 12 hours. After cooling, the reaction mixture was diluted with 250 mL of a 1:1 ethanol;water solvent mixture and stirred for 24h at room temperature. The solid was separated by centrifuging at 10krpm for 40 minutes. This washing procedure was repeated two more times. A small portion was isolated for analysis by STEM and DLS and another portion was dried for further analysis by XRD and IR. Yield: ~4.0g. Analysis: XRD (Figure 3.2), IR (Figure 3.4), 708(s), 755(s), 1042(m), 1109(m), 1373(vs), 1441(s), 1570(s), 1621(vs), 1711(m), 2054 (vw), 3275 (vs)

MIL-100(Fe)-KF Surfactant-free nanoparticles of MIL-100(Fe) were synthesized by the same procedure as MIL100(Fe)-OA without the use of oleylamine. When the product was isolated, the KF was introduced by stirring the isolated product in 0.1 M KF solution for 1 h 40 min. The final isolation was done according to literature precedent.³⁶

Model Complexes Trinuclear iron carboxylate complexes, $[\text{Fe}_3(\mu_3\text{-O})(\text{O}_2\text{CPh})_6(\text{H}_2\text{O})_3]\text{ClO}_4$ ($\text{Fe}_3\text{O-Bz}$, Bz = benzoate), $[\text{Fe}_3(\mu_3\text{-O})(\text{O}_2\text{CPh})_6(\text{C}_5\text{H}_5\text{N})_3]\text{ClO}_4$ ($\text{Fe}_3\text{O-BzPy}$, Py = pyridine), $[\text{Fe}_3(\mu_3\text{-O})(\text{O}_2\text{CCH}_3)_6(\text{H}_2\text{O})_3]\text{Cl}$ ($\text{Fe}_3\text{O-Ac}$, Ac = acetate), and the one-electron-reduced mixed-valence complex, $\text{Fe(III)Fe(III)Fe(II)}(\mu_3\text{-O})(\text{O}_2\text{CCH}_3)_6(\text{H}_2\text{O})_3$ ($\text{MVFe}_3\text{O-Ac}$, MV = mixed valence) were synthesized following literature procedures.³⁷⁻³⁹

[Fe₃(μ₃-O)(O₂CPh)₆(C₅H₅N)₃]ClO₄ (Fe₃O-BzPy, Py = pyridine), was synthesized based on literature procedures.³⁹ Yield: 124.2 mg, 12.11%. Analysis: XRD (Figure 3.3), IR (Figure 3.4) peaks: 1681(w), 1622(vw), 1597(m), 1563(ms), 1528(vw), 1491(m), 1446(m), 1398(s), 1317(w), 1306(w), 1177(m), 1165(w), 1095(s), 1068 (s), 1041 (m), 1024 (m), 1012(m), 937(w), 837(w), 816(w), 754(m), 717(s), 700(s), 684(s), and 674(m).

[Fe₃(μ₃-O)(O₂CPh)₆(H₂O)₃]ClO₄ (Fe₃O-Bz, Bz = benzoate) was synthesized based on literature procedures.³⁹ Analysis: UV-vis (Figure 3.6), IR (Figure 3.4): 673(s), 683(s), 698(vs), 717(vs), 754(m), 818(w), 841(w), 937(m), 1003(m), 1012(m), 1024(m), 1041(m), 1070(s), 1093(s), 1146(vw), 1167(vw), 1178(w), 1221(m), 1308(w), 1315(w), 1398(vs), 1446(m), 1493(m), 1562(s), 1601(s).

[Fe₃(μ₃-O)(O₂CCH₃)₆(H₂O)₃]Cl (Fe₃O-Ac, Ac = acetate) was synthesized based on literature procedures.³⁸ Analysis: UV-vis (Figure 3.6), IR (Figure 3.4), 1583(vs), 1436(s), 1402(vs), 1353(vw), 1045(m), 1030(m), 951(vw), 864(m), 657(vs).

Fe(III)Fe(III)Fe(II)(μ₃-O)(O₂CCH₃)₆(H₂O)₃ (MVFe₃O-Ac, MV = mixed valence) was synthesized based on literature procedures.³⁷ Analysis: UV-vis DR (Figure 3.9), IR (Figure 3.4) 1710(vw), 1583 (vs), 1410(vs), 1348(s), 1257(w), 1049(m), 1035(m), 943(s) , 713(w), 654(vs).

3.2.2 Characterization

The powder XRD patterns were recorded using a Bruker D8 ADVANCE ECO Diffractometer. Attenuated total reflectance infrared spectra were collected for solid samples at room temperature using a Nicolette 6700 FT-IR spectrometer. Each spectrum

was recorded as an average of 64 scans. The hydrodynamic size of the particles dispersed in ethanol was measured using a ZetasizerNano ZS instrument (Malvern) in disposable 1 cm cuvettes. SEM images were obtained using an ultra-high resolution field emission scanning electron microscope (Hitachi S-4800) in transmission mode (STEM). The images were processed using ImageJ for particle size analysis.⁴⁰

3.2.3 Spectroscopic Methods

3.2.3.1 Optical Absorption Spectroscopy

Steady-state electronic absorption spectra were collected using a Cary Varian UV–visible–near-infrared (NIR) spectrophotometer. Transmission mode measurements were collected for liquid-phase samples of the reference complexes (0.17 mM) and MOF nanoparticle suspensions in ethanol in a 1 cm quartz cuvette. Solid-state powder samples were ground thoroughly and measured undiluted using a DR accessory (Harrick Scientific). All measurements were collected at room temperature.

3.2.3.2 Femtosecond Optical Transient Absorption Spectroscopy

The femtosecond OTA spectra of the samples were measured under a pump–probe configuration, as described elsewhere,⁴¹ at the Center for Nanoscale Materials (CNM) at Argonne National Laboratory. The ~ 100 fs pump and probe pulses were both provided by a 5 kHz Coherent Libra Ti: Sapphire ultrafast regenerative amplifier system operating at 800 nm. The pump beam at 400 nm was generated by frequency doubling the 800 nm fundamental from the amplifier; then, the laser beam was chopped to 2.5 kHz. The power and the spot size of the pump beam at the sample position were 0.9 mW and ~ 150 μm , respectively, which produced a pump fluence of $4 \times$

1015 photons/cm². A whitelight continuum probe beam was created by passing the 800 nm fundamental from the amplifier through a 3 mm sapphire plate. The reference complex, Fe₃OBzPy, was dissolved in anhydrous ethanol (1.3 mM concentration) and measured in a 2 mm path length fused silica cuvette.

3.2.3.3 X-ray Absorption Spectroscopy

Steady state X-ray absorption data were collected at the Fe K-edge (7111.2 eV) in transmission mode at Beamline 2-2 at the SSRL. The X-ray white beam was monochromatized by a Si(111) monochromator and detuned by 30% to minimize the harmonic content of the beam. Iron foil was used as the reference for energy calibration. The incident beam intensity (I_0) was measured by a 15 cm ionization chamber with 100% N₂. The transmitted beam intensity (I_t) and reference (I_r) were both measured by a 30 cm ionization chamber with 75% N₂ and 25% Ar. For the model complexes, a mixture of 15 mg of sample, thoroughly ground with ~150 mg of boron nitride, was packed into 3 mm diameter Kapton tubes and heat-sealed from both sides to yield approximately one X-ray absorption length. For each system, with respect to X-ray photons was confirmed by the comparison of several sequential scans collected on a given sample spot, which showed no change, shown in Figure 3.17.

3.2.3.4 X-ray Transient Absorption Spectroscopy

The X-ray transient absorption (XTA) measurements were performed at 11-ID-D, Advanced Photon Source (APS), at Argonne National Lab. The laser pump source was the second-harmonic output of a fs Ti:Sapphire regenerative amplified laser: 400 nm, 100 fs fullwidth-half-maximum (fwhm) and 10 kHz repetition rate. The laser pulse was then

stretched to 0.9 ps using a pair of prisms. The X-ray was Hybrid Fill RHB (Singlet) mode, where an intense X-ray pulse with 16% of the total average photon flux was separated in time from other weak X-ray pulses. The intense X-ray pulse with 118 ps fwhm and 271.5 kHz repetition rate was used as the probe. Samples were prepared in 100% ethanol to yield a 5 mM total concentration of iron in solution (for the model complexes) or colloidal suspension (for the MOF nanoparticles). To minimize photodamage, the liquid sample was purged with nitrogen and circulated in a closed-loop jet flow assembly during data collection. The complete experimental setup has been described elsewhere.⁴² In brief, the laser pump and X-ray probe beams were spatially and temporally overlapped at the 600 μm diameter sample stream. The laser fluence used in the measurements is $\sim 40 \mu\text{J}/\text{mm}^2$. The X-ray fluorescence signal was detected by two avalanche photodiodes (APDs) positioned at 90° angle on both sides of the incident X-ray beam. A third APD detector, collecting upstream X-ray scattering, was used for the normalization. A Z-1 (Mn) filter/soller slit filter combination, which was custom-designed for the specific sample chamber configuration and the distance between the sample and the detector, was inserted between the sample fluid jet and the APD detectors to reduce the scattering background. Ten X-ray absorption spectra were collected and averaged at 100 ps (nominal time zero), 1 ns, 10 ns, 100 ns, and 3.6 μs time delays between the laser pulse and synchronized X-ray bunch. Spectra obtained using the 10 X-ray bunches prior to the synchronized bunch were used to generate an average “pre-time zero” XTA spectrum. Spectra were also collected in the absence of laser light for comparison.

3.3 Results

3.3.1 MIL-100(Fe) Nanoparticle Synthesis and Characterization

To best match the optical and X-ray absorption cross sections in this solid-state material for the XTA measurements, MIL-100(Fe) is prepared in nanoparticle form. Moreover, this format has the added practical benefit of generating stable colloidal suspensions that are compatible with the liquid-jet flow sample arrangement of the XTA experiment. Borrowing from the common preparation methods used in metal and metal-oxide nanoparticle synthesis,⁴³ oleylamine is added to the MOF precursor solution as a surfactant to limit and stabilize particle size formation. For comparison, MOF nanoparticles were also prepared using another previously reported method involving a KF treatment step and no oleylamine.³⁶ The crystallinity of the MOFs generated using both nanoparticle synthesis methods was verified by powder X-ray diffraction (PXRD) analysis, shown in Figure 3.2. The FT-IR spectra were collected for the pyridine loaded MOF and reference complex and compared to the parent in order to identify the presence of pyridine, shown in Figure 3.4.

3.3.1.1 Powder X-Ray Diffraction (PXRD)

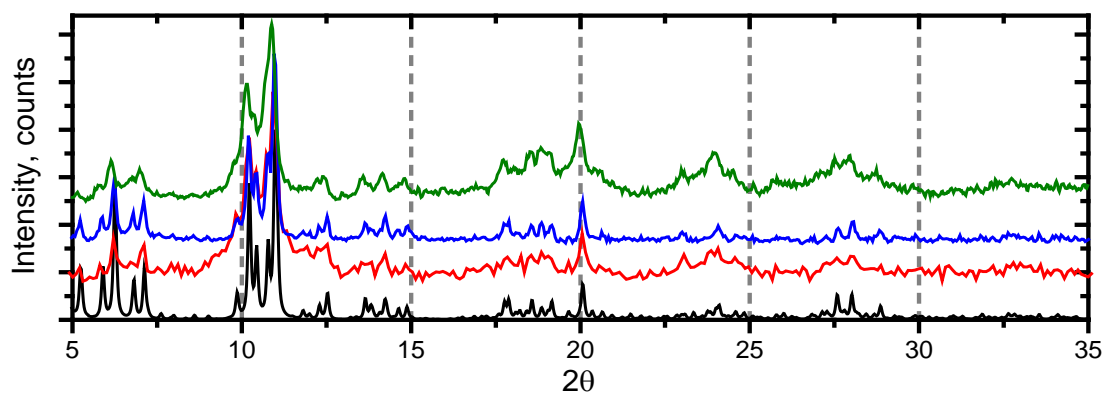


Figure 3.2. PXRD of MIL-100(Fe), Simulated (Black), KF Treated (Red), Oleylamine Treated (Blue), Oleylamine sample after XTA experiment (Green)

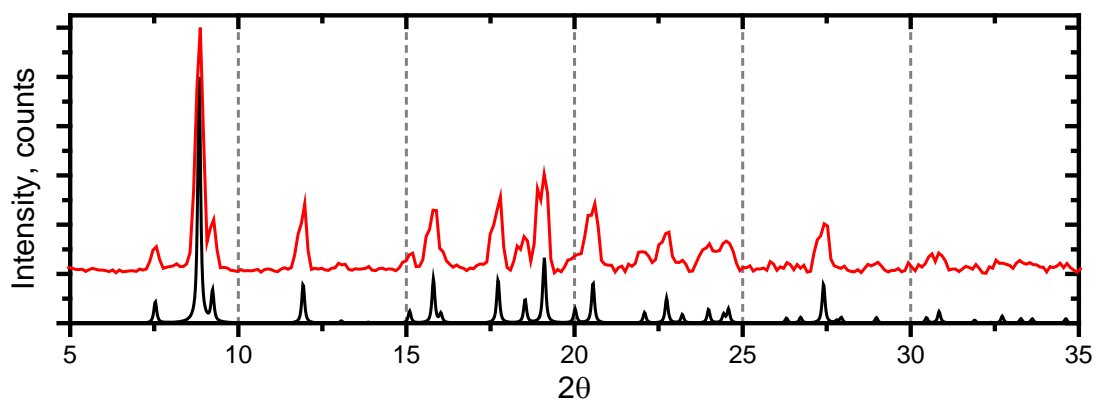


Figure 3.3. Simulated (black) and experimental (red) PXRD patterns for $\text{Fe}_3\text{O-BzPy}$ reference complex

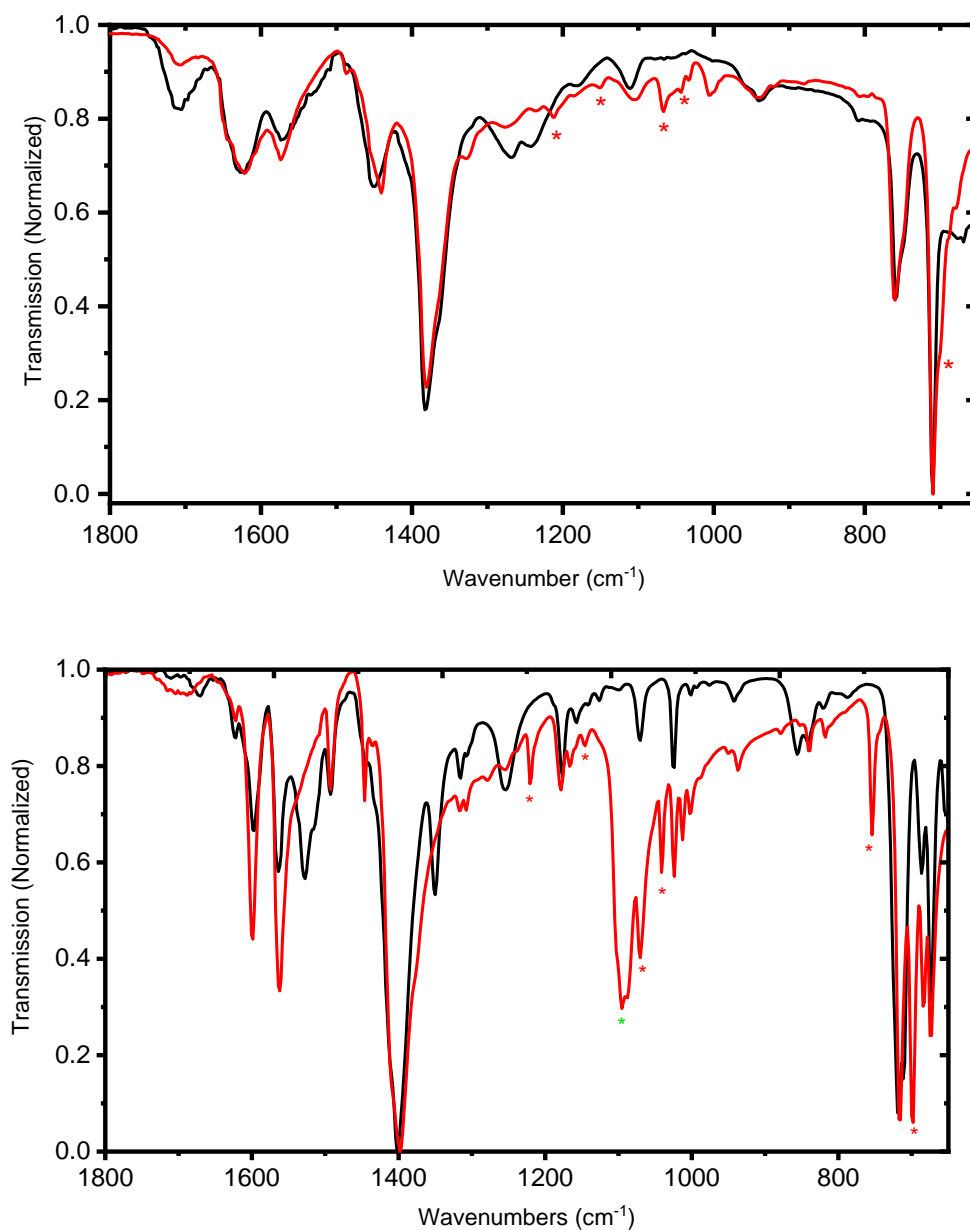


Figure 3.4: FT-IR Spectra of (top): MIL100(Fe) (black) and MIL100(Fe)-Py (red) and (bottom): Fe₃OBz (black) and Fe₃OBzPy (red) with characteristic pyridine modes^{35, 44} marked with red asterisks, perchlorate modes marked with green asterisk

3.3.1.2 Transmission Mode Scanning Electron Microscopy (STEM)

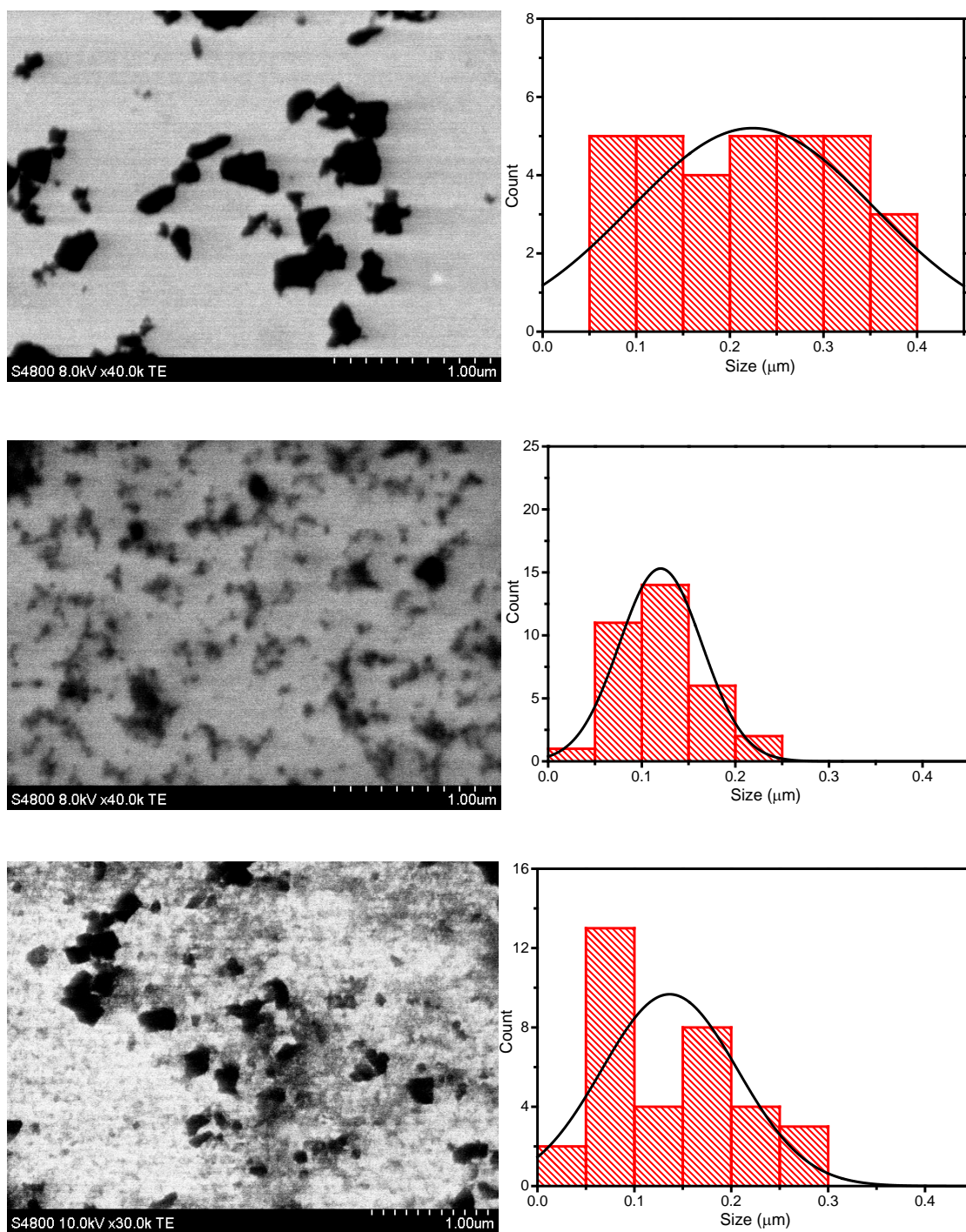


Figure 3.5. Top: STEM Image of MIL-100(Fe)-KF Middle: MIL-100(Fe)-OA, Bottom: MIL-100(Fe)-OA after XTA measurements

3.3.1.3 Dynamic Light Scattering (DLS)

Particle size analysis was performed using several methods including transmission mode scanning electron microscopy (STEM), dynamic light scattering (DLS), and PXRD.⁴⁵ The results of these measurements, including average particle size and size distribution, are summarized in Table 3.5. While both preparation schemes generated nanoscale MIL-100 particles, the oleylamine method succeeded in generating smaller average particle size (130 vs 200 nm) with narrower size distribution. Moreover, this sample showed better stability upon irradiation with 400 nm laser light.

Table 3.1. DLS Results for MIL-100(Fe)-OA

Sample Name	Peak 1 Mean (r.nm)	Peak 2 Mean (r.nm)	Peak 1 Area Integration (%)	Peak 2 Area Integration (%)
MIL100-OA	83.87	0	100	0
MIL100-OA	135.2	0	100	0
MIL100-OA	266.6	0	100	0

Table 3.2. DLS Results for MIL-100(Fe) treated with KF

Sample Name	Peak 1 Mean (r.nm)	Peak 2 Mean (r.nm)	Peak 1 Area Integration (%)	Peak 2 Area Integration (%)
MIL100-KF	224	139.4	54.2	45.8
MIL100-KF	179.8	0	100	0
MIL100-KF	192.9	0	100	0

Table 3.3. Summary of particle sized determined DLS, XRD, and STEM.

Sample	DLS (nm)	STEM (nm)	PXRD (nm)	Average (nm)
MIL-100 KF	249	210 ± 104	128 ± 31	196
MIL-100 OA	161	120 ± 44	115 ± 87	133
MIL-100 OA After XTA	----	137 ± 70	----	137

3.3.2 Optical Absorption Spectroscopy.

The optical electronic absorption spectra for the MOF materials were obtained through transmission absorption measurements of the colloidal nanoparticle suspensions and diffuse reflectance (DR) measurements of the solid-state powders. Both transmission and DR spectra were also obtained for the trinuclear iron carboxylate model complexes in solution and solid state, respectively. The transmission spectra for the MOF and the Fe_3OBz and Fe_3OBzPy model complexes are illustrated in Figure 3.6 and Figure 3.7. These systems all exhibit a similar broad absorption spectrum with unresolved overlapping bands in the UV region that extends to the visible spectral range. While the colloidal suspension of the MOF produces a significant scattering contribution to the spectrum that obscures any low extinction absorption features, DR data (Figure 3.8) better reveal the underlying absorption bands and allow a more substantive spectral comparison with the reference complexes. Besides the dominant absorption envelope in the UV, which presumably contains the LMCT state transition, several weak bands are observed in the visible wavelength range. These are attributed to ligand field-state transitions and are only clearly observed in the undiluted solid state sample spectra. Comparison between the $\text{Fe}_3\text{O-BzPy}$ and $\text{Fe}_3\text{O-Bz}$ model complex spectra indicates that

while the presence of the coordinated pyridine alters the low extinction ligand field state transition energies, the main band containing the LMCT state transition remains relatively unchanged. Because the mixed-valence complex, $\text{MVFe}_3\text{O}-\text{Ac}$, was only stable in the solid state, only the DR spectrum was obtained for this model complex. Comparison with the DR spectrum of $\text{Fe}_3\text{O}-\text{Ac}$ (Figure 3.9) reveals an additional broad intervalence band in the NIR spectral region for $\text{MVFe}_3\text{O}-\text{Ac}$ in addition to the weak ligand field bands that are inherent to both complexes.

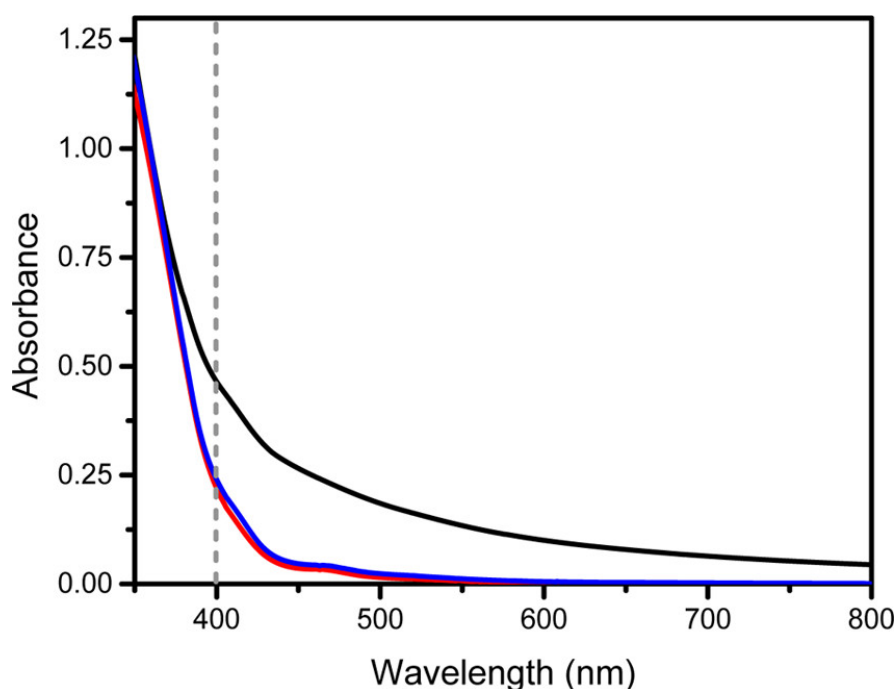


Figure 3.6. Transmission UV-vis absorption of MIL-100(Fe)-OA (black), $\text{Fe}_3\text{O}-\text{Bz}$ (red), and $\text{Fe}_3\text{O}-\text{BzPy}$ (blue). Vertical dashed line indicates pump laser wavelength for XTA measurements

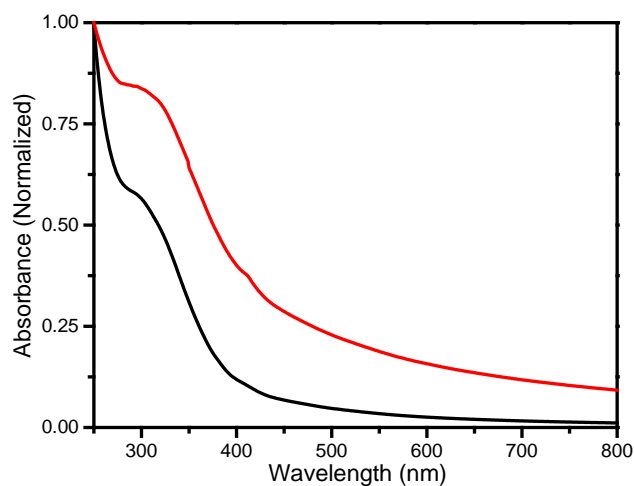


Figure 3.7. Transmission UV/VIS spectra of a suspension of MIL-100(Fe)-OA in ethanol (black) and MIL-100(Fe)-KF Treated (red).

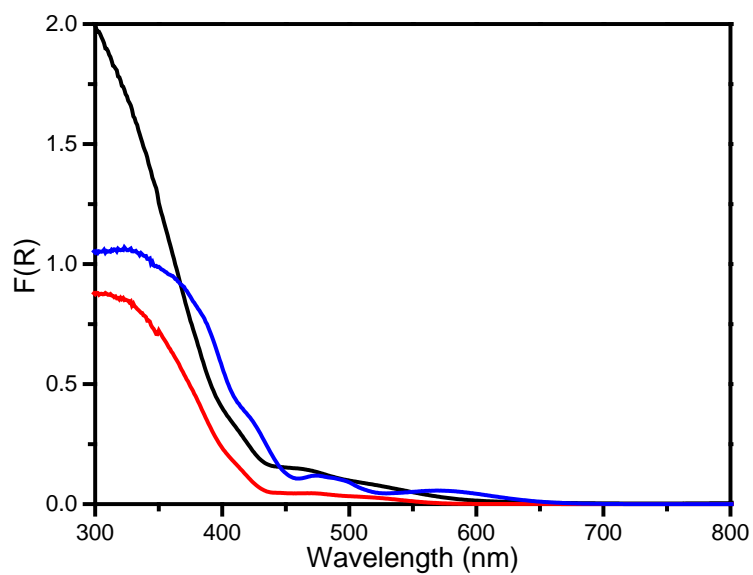


Figure 3.8. Diffuse reflectance spectra of MIL-100(Fe)-OA (Black), Fe₃O-Bz (Red) and Fe₃O-BzPy (blue).

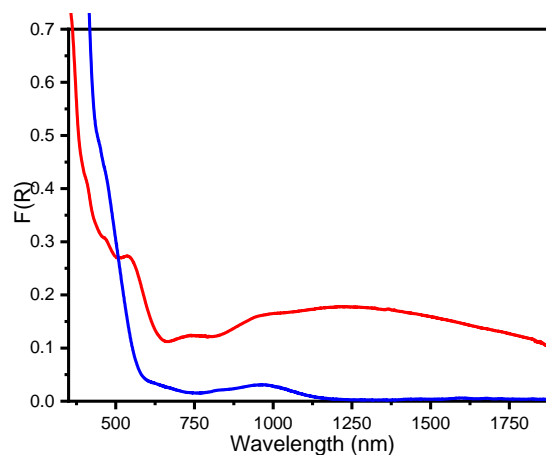


Figure 3.9. Diffuse Reflectance Spectra of $\text{Fe}_3\text{O-Ac}$ (blue) and $\text{MVFe}_3\text{O-Ac}$ (red)

3.3.3 Ultrafast Optical Transient Absorption Spectroscopy

Ultrafast OTA measurements were collected using a 400 nm actinic pump and a broadband visible wavelength probe for both MIL-100(Fe)-OA and the $\text{Fe}_3\text{O-BzPy}$ complex. The reference complex exhibited a broad TA signal throughout the visible region with a maximum around 530 nm. These data along with the results of the multiexponential fit of the decay are provided in Figure 3.10 and Table 3.4. The kinetics analysis indicates that the majority of the excited state decays on a subpicosecond time scale and that the longest component of the lifetime is on the order of 250 ps. Attempts to extract analogous excited state decay kinetics in this early time regime for MIL-100(Fe)-OA , however, were unsuccessful because the weak OTA signal from the MOF colloidal suspension was overwhelmed by adverse light-scattering effects in this energy range.

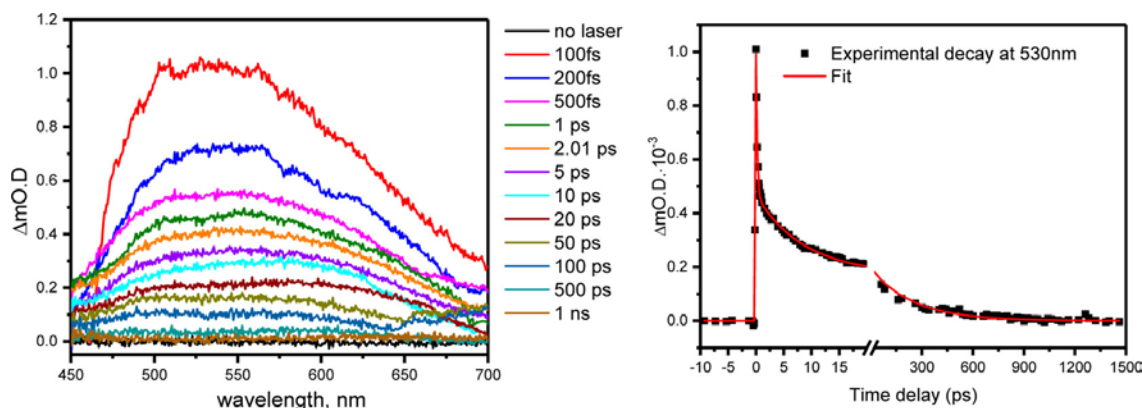


Figure 3.10. Optical transient absorption spectra collected at different time delays, up to 1 ns (left) and kinetics probed at 530 nm (right) of the $\text{Fe}_3\text{O-BzPy}$ reference complex.

Table 3.4. OTA Exponential Lifetime Fitting Results for $\text{Fe}_3\text{O-BzPy}$ at 530 nm

	τ	A (%)
IRF	140.0 ± 0 fs	
τ_1	209.2 ± 8.6 fs	72 ± 1
τ_2	8.2 ± 0.5 ps	16 ± 1
τ_3	250.2 ± 11.2 ps	11 ± 1

3.3.4 Steady-State X-ray Absorption Spectroscopy

Steady state Fe K-edge X-ray absorption spectra measured for the MIL-100(Fe) MOF and all trinuclear Fe carboxylate reference complexes are shown in Figure 3.11. The similarity of the MOF, $\text{Fe}_3\text{O-Bz}$, $\text{Fe}_3\text{O-BzPy}$, and $\text{Fe}_3\text{O-Ac}$ spectra, including edge energy position, indicates identical Fe(III) oxidation states and comparable iron coordination environments in each case. The spectrum of $\text{MVFe}_3\text{O-Ac}$ exhibits an edge shift to lower energy by 2.79 eV compared with that of $\text{Fe}_3\text{O-Ac}$, which is caused by the one electron reduced trinuclear Fe(III)/Fe(III)/Fe(II) mixed-valence cluster. This shift is consistent with those reported for numerous other iron oxides with the same iron valence compositions.⁴⁶⁻⁴⁸

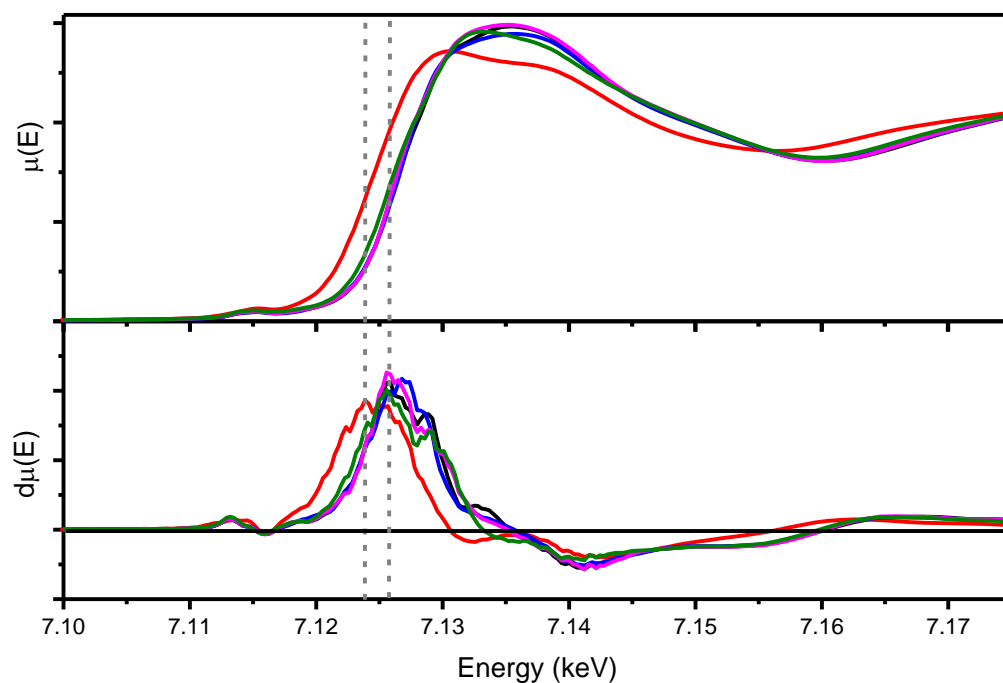


Figure 3.11. (Top) Steady State XAS of MIL-100(Fe) (Black) and reference Complexes Fe₃O-BzPy (green), Fe₃O-Bz (magenta), MVFe₃O-Ac (Red), and Fe₃O-Ac (Blue). (Bottom) Derivative of the XAS Spectra

An overlay of the XANES spectra of the Fe(III) and mixed-valence iron acetate reference complexes, Fe₃O-Ac and MVFe₃O-Ac, is shown in Figure 3.12a along with the corresponding difference spectrum obtained between the two.

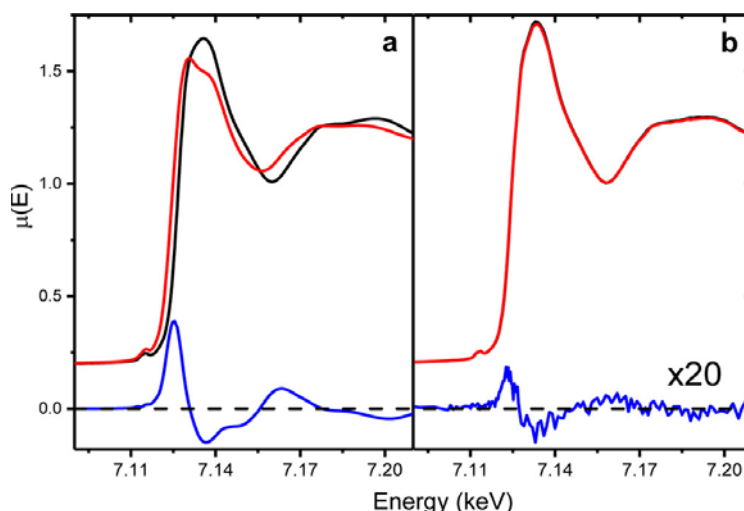


Figure 3.12. (a) Steady-state XANES spectra of $\text{Fe}_3\text{O-Ac}$ (black) and $\text{MVFe}_3\text{O-Ac}$ (red). (b) “Pre-time zero” (black) and “time zero” (red) XTA spectra for MIL-100(Fe)-OA. Corresponding difference spectra shown in blue and vertical offset included for clarity.

3.3.4 X-ray Transient Absorption Spectroscopy

XTA spectra were measured at several delay times for the MOF nanoparticle suspensions and the iron benzoate pyridine reference complex. The spectra of MIL-100(Fe)-OA collected at nominal time zero ($t = 100$ ps) and pretime zero delays (referred to as “time zero” and “pre-time zero” spectra respectively) are overlaid in Figure 3.12. A 20 \times magnification of their difference spectrum is shown at the bottom of the graph to highlight the transient edge energy shift. The analogous spectra collected for the MIL-100(Fe)-KF nanoparticles (Figure 3.13) and the $\text{Fe}_3\text{O-BzPy}$ reference complex exhibit the same edge energy shift trend. The amplitude of the derivative-like feature of the reference complex difference spectrum, however, is markedly smaller than that of the MOF systems, as illustrated in Figure 3.14.

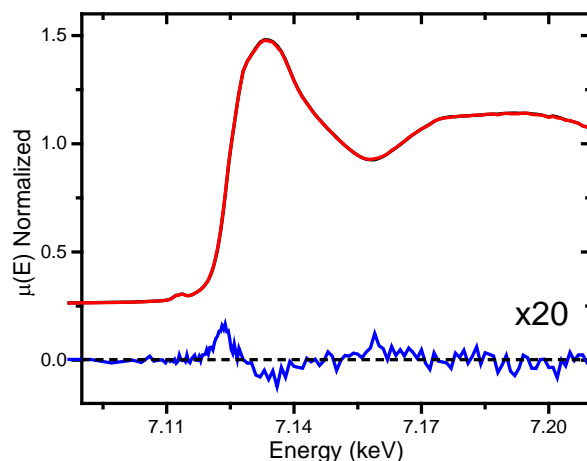


Figure 3.13. “time-zero” (red) and “pre-time zero” (black) XTA spectra of MIL-100(Fe)-KF. Difference spectrum shown in blue. (vertical offset for clarity)

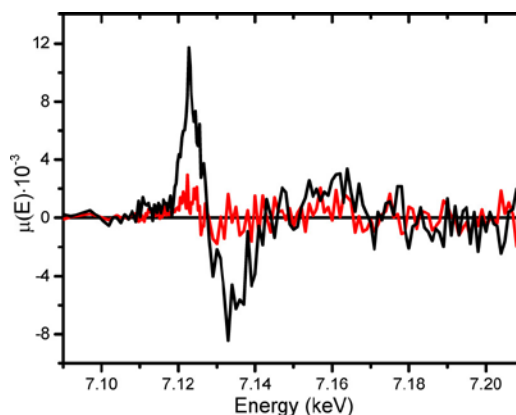


Figure 3.14 “Time zero” XTA difference spectra of MIL-100(Fe)-OA (black) and Fe₃O-BzPy (red).

XTA spectra collected at later time delays marked the decay of these transient difference signals. As shown in Figure 3.15, the derivative feature of the MIL-100(Fe)-OA difference spectrum is still apparent at 100 ns time delay and decays by the 3.6 μ s time delay. In contrast, the difference signal for the reference complex is not observed at these later time delays, indicating a near complete decay within 1 ns (Figure 3.15).

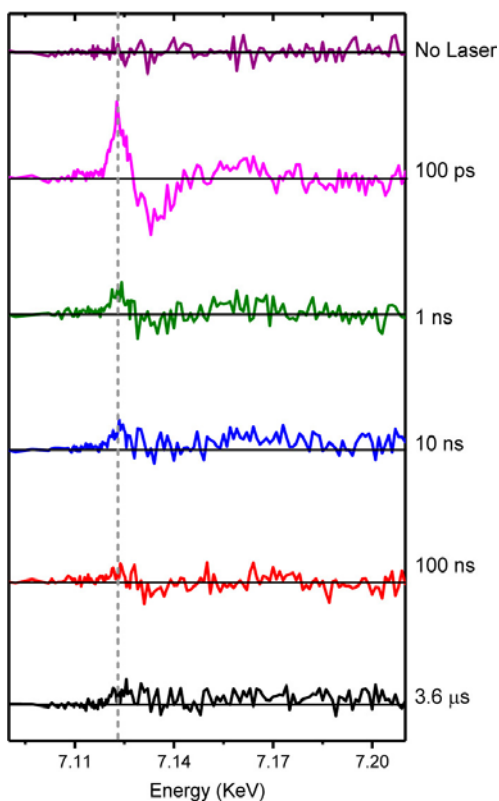


Figure 3.15. XTA difference spectra obtained at multiple time delays for MIL100(Fe)-OA. Vertical offsets included for clarity. The XTA difference spectrum collected in the absence of laser light is plotted at the top for comparison

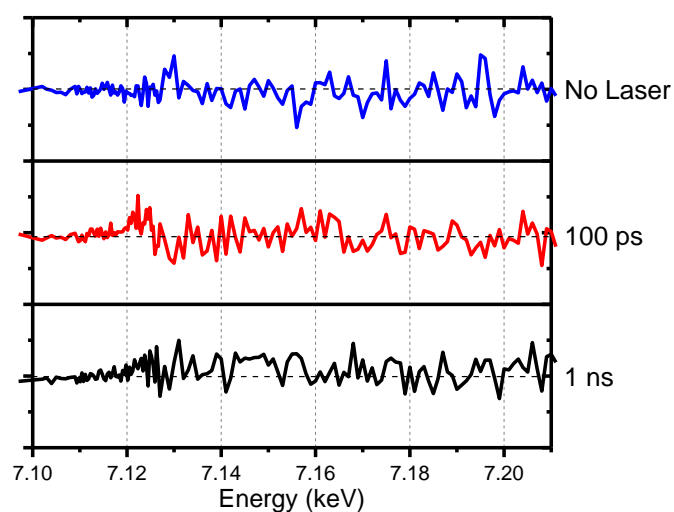


Figure 3.16. XTA difference spectra obtained at multiple time delays for Fe₃O-BzPy.

To assess X-ray or laser damage, multiple scans were collected in the absence of either the laser pump or x-ray probe, as seen in Figures 3.17 and 3.18. Without laser irradiation, there is no apparent significant changes in the spectrum after multiple acquisitions for the MOF or the reference complex. Changes in amplitude of the white line seen in the MIL-100-OA spectrum are due to settling of nanoparticles through the experiment. In Figure 3.17, damage due to the laser, in the absence of the x-ray probe, was assessed. A slight shift in the edge to lower energy is observed after subsequent scans, indicating a build of permanently reduced iron sites. Due to this observation, the sample was refreshed often to prevent this photoreduction.

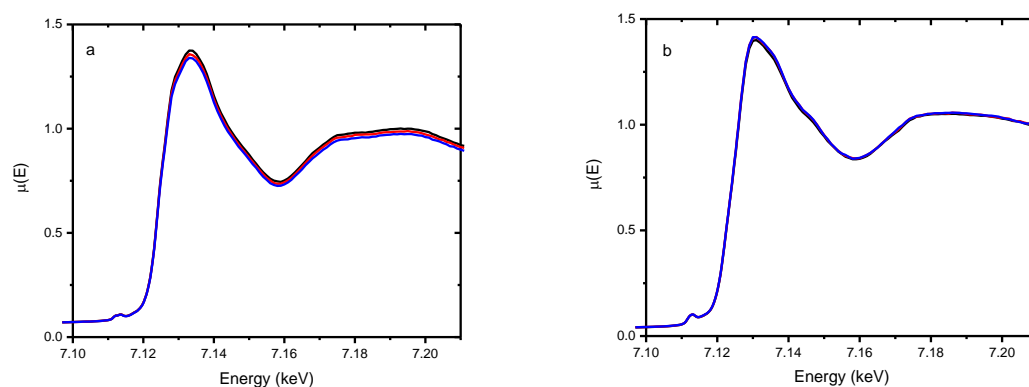


Figure 3.17. Sample stability assessment for XTA measurements: negligible X-ray-induced changes. Three sequential XTA Spectra collected in the absence of laser irradiation for a) MIL-100(Fe)-OA and b) Fe₃-OBzPy. Observed amplitude reduction for MIL-100(Fe)-OA sample is attributed to slight settling of nanoparticles out of suspension in the reservoir over time.

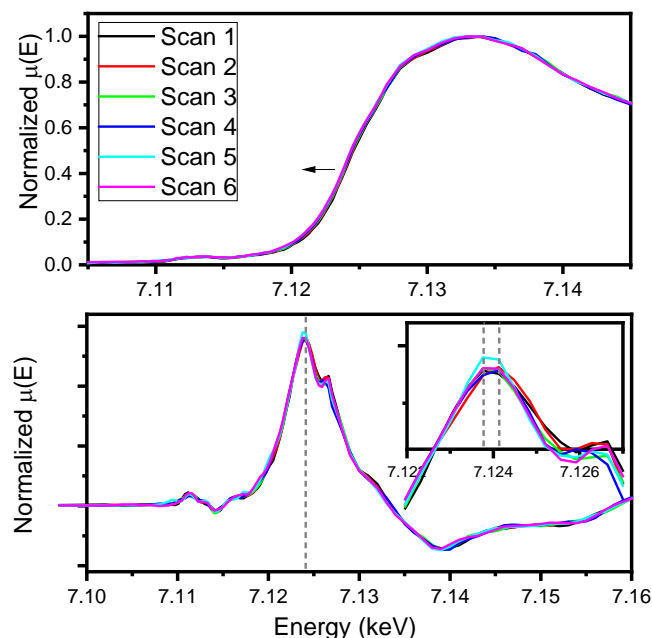


Figure 3.18. Sample stability assessment for XTA measurements: laser-induced changes. Representative individual XTA spectra (first 6 sequential scans) collected from one sample of MIL-100(Fe)-OA. Corresponding derivative spectra (bottom) shows very small edge shift to lower energy from one scan to the next, revealing a slight build-up of laser photo-reduced iron sites in the sample over the course of these measurements. Note: only the first few scans per sample were included to generate the average XTA spectrum for each system/delay time measured.

3.4 Discussion

MIL-100(Fe) was generated in nanoparticle form to not only promote a stable colloidal suspension for the XTA measurements but also accommodate the different optical and X-ray photon absorption cross sections in this material. Moreover, in terms of practical applications, the large surface-to-volume ratio and more readily accessible iron clusters of the nanoparticle format would likely lead to higher photocatalytic activity.

Compared with MIL-100(Fe)-KF, MIL-100(Fe)-OA exhibited smaller particle size, narrower size distribution, and also higher stability upon irradiation with 400 nm laser light. With average particle diameter size of ~ 130 nm, the percentage of surface located iron clusters in MIL-100(Fe)-OA is estimated to be on the order of $\sim 1\%$ and therefore have a negligible contribution to the observed XTA signal.

Calculation of the fraction of iron clusters on the surface of MIL-100(Fe)-OA nanoparticles was performed using the following equation using spherical particle approximation⁴⁹ :

$$F = \frac{4}{\sqrt[3]{n}} \quad (1)$$

$$\% \text{ Fe on the surface} = \frac{F}{n} \cdot 100\% \quad (2)$$

where F is a fraction of atoms on the surface and n is the total number of atoms in the nanoparticles. Each particle with the size of 130 nm has mass equal to $1.115 \cdot 10^{-18}$ g. Based on the molecular formula for MIL-100 ($\text{Fe}_3\text{C}_{18}\text{H}_{36}\text{O}_{28.5}$)⁵⁰ its molecular weight is 876 g/mol, which translates to $1.31 \cdot 10^{-21}$ moles or 791 MOF units in the particle. Since each MOF unit has 3 iron centers, the total number of iron centers is equal 2373. Using equations 1 and 2 we obtain fraction of iron centers on the surface to be $\sim 1.3\%$.

Any observed transient spectral changes can therefore be ascribed primarily to the electronic structure changes of the photoexcited iron cluster node sites within the nanoparticle (albeit within layers of the framework closer to the surface), not just on its outermost surface. This is an important distinction for potential photocatalytic applications that may rely on utilizing active sites within the porous structure of these

frameworks for improved control over their reactivity. Analysis of the XTA measurements collected for the MIL-100 MOF and Fe(III) model complex confirms the charge separated nature of their excited states that evades definitive detection by other time-resolved spectroscopy methods. Laser excitation at 400 nm is used to populate the LMCT excited state suspected within the broad envelope of poorly resolved absorption bands that extend into the visible spectral region (Figure 3.6) for each of these Fe₃-μ₃-oxo-based systems. The X-ray probe of the Fe K-edge reveals the transient electronic changes associated with the iron sites in these materials. These changes are best illustrated by the difference spectra depicted in Figure 3.12b. The derivative-like feature of the XTA difference spectrum of MIL-100(Fe)-OA highlights the edge shift to lower energy upon excited-state population. The same edge shift trend is indicated by the difference spectrum of the Fe₃O-BzPy model complex as well, albeit with significantly smaller amplitude (Figure 3.14). These transient changes indicate increased electron density at the iron sites, as would be associated with the population of charge-transfer excited states. To further confirm this assignment, these difference spectra were compared with one generated from the steady-state X-ray absorption spectra of Fe₃O-Ac and its mixed-valence analogue, MVFe₃O-Ac. (The acetate version of these trinuclear iron carboxylate complexes was employed for this comparison due to the higher stability of its mixed-valence species compared with that of the analogous benzoate complex.) The latter, with a one-electron reduction of the trinuclear iron cluster, serves as a model for the transiently reduced iron-oxo clusters produced through LMCT excitation. The shape of the difference spectra in both experiments looks nearly identical, suggesting similarly reduced iron electron configurations. Notably, the MIL100(Fe)-KF XTA data

show the same edge shift as those of the MOF (Figure 3.13). This verifies that the oleylamine surfactant is not involved in the excited LMCT state of MIL100(Fe)-OA. Rather, the charge transfer occurs from the trimesate linkers to the iron-oxo clusters in both MOF cases. XTA measurements collected at subsequent time delays verified the long-lived nature of the charge separated excited state of the MOF. As illustrated in Figure 3.15, the XTA difference signal indicating charge separation persists at least into the hundreds of nanoseconds time range for the MIL-100(Fe)-OA suspension. Moreover, these data are consistent with the excited-state lifetime information obtained through OTA measurements. Previously reported nanosecond OTA data for closely related MOF systems have indicated that the lifetime of the excited state is on the order of hundreds of nanoseconds to microseconds.¹⁹ For comparison, the XTA difference signal for the reference complex, Fe₃O-BzPy, decays by 1 ns time delay (Figure 3.16), indicating a much shorter CT-state lifetime. Indeed, analysis of the femtosecond OTA kinetics obtained for this reference complex (Figure 3.10) revealed its longest lifetime component to be only ~250 ps. The short lifetime of Fe₃OBzPy, compared with that of the MOF, also accounts for the smaller amplitude difference XTA signal observed at the earliest delay time because much of the excited-state decay would occur within the ~120 ps X-ray pulse duration. This assessment is further supported by the OTA data, which show that much of the optical signal is decayed by 100 ps. The different lifetimes of the MOF and the reference complex, as indicated by the XTA (and OTA) measurements, suggest the important role of delocalization and the framework in stabilizing the charge-separated excited states. In the complex, the transferred electron in the CT excited state may be partially delocalized among the trinuclear iron sites (the analogous mixed-valence ground

state of the reference complex $\text{MVFe}_3\text{O}-\text{Ac}$, e.g., has been reported as “class II” according to the Robin-Day classification system, i.e., partial charge delocalization,⁵¹ but it is still limited to one iron-oxo cluster (i.e., intra-cluster charge delocalization only), and, consequently, geminate charge recombination is the most likely deactivation pathway. In the case of the MOF environment, these iron-oxo clusters are interconnected by aromatic carboxylate linkers that appear to promote charge migration between clusters, thereby delaying recombination via intercluster delocalization. Understanding the mechanism and framework attributes that promote this charge migration is beyond the scope of this study but is an important future research direction in the area of photoactive MOF materials

3.5 References

1. Han, F.; Kambala, V. S. R.; Srinivasan, M.; Rajarathnam, D.; Naidu, R., Tailored Titanium Dioxide Photocatalysts for the Degradation of Organic Dyes in Wastewater Treatment: A Review. *Applied Catalysis A: General* **2009**, *359* (1–2), 25–40.
2. Ni, M.; Leung, M. K. H.; Leung, D. Y. C.; Sumathy, K., A Review and Recent Developments in Photocatalytic Water-Splitting Using TiO₂ for Hydrogen Production. *Renewable and Sustainable Energy Reviews* **2007**, *11* (3), 401–425.
3. Wang, H.; Zhang, L.; Chen, Z.; Hu, J.; Li, S.; Wang, Z.; Liu, J.; Wang, X., Semiconductor Heterojunction Photocatalysts: Design, Construction, and Photocatalytic Performances. *Chemical Society Reviews* **2014**, *43* (15), 5234–5244.
4. Kim, Y. I.; Salim, S.; Huq, M. J.; Mallouk, T. E., Visible-Light Photolysis of Hydrogen Iodide Using Sensitized Layered Semiconductor Particles. *Journal of the American Chemical Society* **1991**, *113* (25), 9561–9563.
5. Peng, T.; Dai, K.; Yi, H.; Ke, D.; Cai, P.; Zan, L., Photosensitization of Different Ruthenium(II) Complex Dyes on TiO₂ for Photocatalytic H₂ Evolution Under Visible-Light. *Chemical Physics Letters* **2008**, *460* (1–3), 216–219.
6. Zhang, X.; Peng, T.; Song, S., Recent Advances in Dye-Sensitized Semiconductor Systems for Photocatalytic Hydrogen Production. *Journal of Materials Chemistry A* **2016**, *4* (7), 2365–2402.
7. Furukawa, H.; Cordova, K. E.; O’Keeffe, M.; Yaghi, O. M., The Chemistry and Applications of Metal-Organic Frameworks. *Science* **2013**, *341* (6149), 1230444.
8. Wang, C.; Liu, D.; Lin, W., Metal–Organic Frameworks as A Tunable Platform for Designing Functional Molecular Materials. *Journal of the American Chemical Society* **2013**, *135* (36), 13222–13234.
9. Dhakshinamoorthy, A.; Asiri, A. M.; García, H., Metal–Organic Framework (MOF) Compounds: Photocatalysts for Redox Reactions and Solar Fuel Production. *Angewandte Chemie International Edition* **2016**, *55* (18), 5414–5445.
10. Horiuchi, Y.; Toyao, T.; Takeuchi, M.; Matsuoka, M.; Anpo, M., Recent Advances in Visible-Light-Responsive Photocatalysts for Hydrogen Production and Solar Energy Conversion - from Semiconducting TiO₂ to MOF/PCP photocatalysts. *Physical Chemistry Chemical Physics* **2013**, *15* (32), 13243–13253.
11. Wang, J.-L.; Wang, C.; Lin, W., Metal–Organic Frameworks for Light Harvesting and Photocatalysis. *ACS Catalysis* **2012**, *2* (12), 2630–2640.
12. Zhang, T.; Lin, W., Metal-Organic Frameworks for Artificial Photosynthesis and Photocatalysis. *Chemical Society Reviews* **2014**.
13. Maza, W. A.; Haring, A. J.; Ahrenholtz, S. R.; Epley, C. C.; Lin, S. Y.; Morris, A. J., Ruthenium(II)-Polypyridyl Zirconium(IV) Metal-Organic Frameworks as a New Class of Sensitized Solar Cells. *Chemical Science* **2016**, *7* (1), 719–727.
14. Wang, C.; deKrafft, K. E.; Lin, W., Pt Nanoparticles@Photoactive Metal–Organic Frameworks: Efficient Hydrogen Evolution via Synergistic Photoexcitation and Electron Injection. *Journal of the American Chemical Society* **2012**, *134* (17), 7211–7214.
15. Zhou, T.; Du, Y.; Borgna, A.; Hong, J.; Wang, Y.; Han, J.; Zhang, W.; Xu, R., Post-Synthesis Modification of a Metal-Organic Framework to Construct a Bifunctional

Photocatalyst for Hydrogen Production. *Energy & Environmental Science* **2013**, 6 (11), 3229-3234.

16. Fu, Y.; Sun, D.; Chen, Y.; Huang, R.; Ding, Z.; Fu, X.; Li, Z., An Amine-Functionalized Titanium Metal–Organic Framework Photocatalyst with Visible-Light-Induced Activity for CO₂ Reduction. *Angewandte Chemie International Edition* **2012**, 51 (14), 3364-3367.
17. Wang, D.; Huang, R.; Liu, W.; Sun, D.; Li, Z., Fe-Based MOFs for Photocatalytic CO₂ Reduction: Role of Coordination Unsaturated Sites and Dual Excitation Pathways. *ACS Catalysis* **2014**, 4 (12), 4254-4260.
18. Laurier, K. G. M.; Vermoortele, F.; Ameloot, R.; De Vos, D. E.; Hofkens, J.; Roelfaers, M. B. J., Iron(III)-Based Metal–Organic Frameworks As Visible Light Photocatalysts. *Journal of the American Chemical Society* **2013**, 135 (39), 14488-14491.
19. Laurier, K. G. M.; Fron, E.; Atienzar, P.; Kennes, K.; Garcia, H.; Van der Auweraer, M.; De Vos, D. E.; Hofkens, J.; Roelfaers, M. B. J., Delayed Electron-Hole Pair Recombination in Iron(III)-Oxo Metal-Organic Frameworks. *Physical Chemistry Chemical Physics* **2014**, 16 (11), 5044-5047.
20. Bressler, C.; Milne, C.; Pham, V. T.; ElNahhas, A.; van der Veen, R. M.; Gawelda, W.; Johnson, S.; Beaud, P.; Grolimund, D.; Kaiser, M.; Borca, C. N.; Ingold, G.; Abela, R.; Chergui, M., Femtosecond XANES Study of the Light-Induced Spin Crossover Dynamics in an Iron(II) Complex. *Science* **2009**, 323 (5913), 489.
21. Cannizzo, A.; Milne, C. J.; Consani, C.; Gawelda, W.; Bressler, C.; van Mourik, F.; Chergui, M., Light-Induced Spin Crossover in Fe(II)-Based Complexes: The Full Photocycle Unraveled by Ultrafast Optical and X-Ray Spectroscopies. *Coordination Chemistry Reviews* **2010**, 254 (21), 2677-2686.
22. Chen, L. X.; Jager, W. J. H.; Jennings, G.; Gosztola, D. J.; Munkholm, A.; Hessler, J. P., Capturing a Photoexcited Molecular Structure Through Time-Domain X-ray Absorption Fine Structure. *Science* **2001**, 292 (5515), 262-264.
23. Chen, L. X.; Shaw, G. B.; Novozhilova, I.; Liu, T.; Jennings, G.; Attenkofer, K.; Meyer, G. J.; Coppens, P., MLCT State Structure and Dynamics of a Copper(I) Diimine Complex Characterized by Pump-Probe X-ray and Laser Spectroscopies and DFT Calculations. *Journal of the American Chemical Society* **2003**, 125 (23), 7022-7034.
24. Cho, H.; Strader, M. L.; Hong, K.; Jamula, L.; Gullikson, E. M.; Kim, T. K.; de Groot, F. M. F.; McCusker, J. K.; Schoenlein, R. W.; Huse, N., Ligand-Field Symmetry Effects in Fe(II) Polypyridyl Compounds Probed by Transient X-ray Absorption Spectroscopy. *Faraday Discussions* **2012**, 157 (0), 463-474.
25. Gawelda, W.; Pham, V.-T.; Benfatto, M.; Zaushtsyn, Y.; Kaiser, M.; Grolimund, D.; Johnson, S. L.; Abela, R.; Hauser, A.; Bressler, C.; Chergui, M., Structural Determination of a Short-Lived Excited Iron(II) Complex by Picosecond X-Ray Absorption Spectroscopy. *Physical Review Letters* **2007**, 98 (5), 057401.
26. Lockard, J. V.; Rachford, A. A.; Smolentsev, G.; Stickrath, A. B.; Wang, X.; Zhang, X.; Attenkofer, K.; Jennings, G.; Soldatov, A.; Rheingold, A. L.; Castellano, F. N.; Chen, L. X., Triplet Excited State Distortions in a Pyrazolate Bridged Platinum Dimer Measured by X-ray Transient Absorption Spectroscopy. *The Journal of Physical Chemistry A* **2010**, 114 (48), 12780-12787.

27. Shelby, M. L.; Mara, M. W.; Chen, L. X., New Insight into Metalloporphyrin Excited State Structures and Axial Ligand Binding from X-ray Transient Absorption Spectroscopic Studies. *Coordination Chemistry Reviews* **2014**, 277–278, 291-299.
28. Smolentsev, G.; Sundström, V., Time-resolved X-ray Absorption Spectroscopy for the Study of Molecular Systems Relevant for Artificial Photosynthesis. *Coordination Chemistry Reviews* **2015**, 304–305, 117-132.
29. van der Veen, R. M.; Milne, C. J.; El Nahhas, A.; Lima, F. A.; Pham, V.-T.; Best, J.; Weinstein, J. A.; Borca, C. N.; Abela, R.; Bressler, C.; Chergui, M., Structural Determination of a Photochemically Active Diplatinum Molecule by Time-Resolved EXAFS Spectroscopy. *Angewandte Chemie International Edition* **2009**, 48 (15), 2711-2714.
30. Chen, L. X., Taking Snapshots of Photoexcited Molecules in Disordered Media by Using Pulsed Synchrotron X-rays. *Angewandte Chemie-International Edition* **2004**, 43 (22), 2886-2905.
31. Huang, J.; Buyukcakir, O.; Mara, M. W.; Coskun, A.; Dimitrijevic, N. M.; Barin, G.; Kokhan, O.; Stickrath, A. B.; Ruppert, R.; Tiede, D. M.; Stoddart, J. F.; Sauvage, J.-P.; Chen, L. X., Highly Efficient Ultrafast Electron Injection from the Singlet MLCT Excited State of Copper(I) Diimine Complexes to TiO₂ Nanoparticles. *Angewandte Chemie International Edition* **2012**, 51 (51), 12711-12715.
32. Pattengale, B.; Yang, S.; Ludwig, J.; Huang, Z.; Zhang, X.; Huang, J., Exceptionally Long-Lived Charge Separated State in Zeolitic Imidazolate Framework: Implication for Photocatalytic Applications. *Journal of the American Chemical Society* **2016**, 138 (26), 8072-8075.
33. Zamponi, F.; Penfold, T. J.; Nachtegaal, M.; Lubcke, A.; Rittmann, J.; Milne, C. J.; Chergui, M.; van Bokhoven, J. A., Probing the Dynamics of Plasmon-Excited Hexanethiol-Capped Gold Nanoparticles by Picosecond X-ray Absorption Spectroscopy. *Physical Chemistry Chemical Physics* **2014**, 16 (42), 23157-23163.
34. Zhang, X.; Smolentsev, G.; Guo, J.; Attenkofer, K.; Kurtz, C.; Jennings, G.; Lockard, J. V.; Stickrath, A. B.; Chen, L. X., Visualizing Interfacial Charge Transfer in Ru-Dye-Sensitized TiO₂ Nanoparticles Using X-ray Transient Absorption Spectroscopy. *The Journal of Physical Chemistry Letters* **2011**, 2 (6), 628-632.
35. Zhang, F.; Shi, J.; Jin, Y.; Fu, Y.; Zhong, Y.; Zhu, W., Facile Synthesis of MIL-100(Fe) Under HF-Free Conditions and Its Application in the Acetalization of Aldehydes with Diols. *Chemical Engineering Journal* **2015**, 259, 183-190.
36. Bellido, E.; GuilleVIC, M.; Hidalgo, T.; Santander-Ortega, M. J.; Serre, C.; Horcajada, P., Understanding the Colloidal Stability of the Mesoporous MIL-100(Fe) Nanoparticles in Physiological Media. *Langmuir : the ACS journal of surfaces and colloids* **2014**, 30 (20), 5911-20.
37. Dai, J.-X.; Wu, F.-H.; Rothenberger, A.; Zhang, Q.-F., Synthesis and Structures of μ -3-Oxo-Centered Mixed-Valent Trinuclear Iron Complexes with 1-Methyl-Imidazole Ligands. *Z. Naturforsch* **2007**, 62b, 1117 – 1122.
38. Shova, S. G.; Cadelnic, I. G.; Gdaniec, M.; Simonov, Y. A.; Jovmir, T. C.; Meriacre, V. M.; Filoti, G.; Turta, C. I., Syntheses and Structural Study of Trinuclear Iron Acetates [Fe₃O(CH₃COO)₆(H₂O)₃]Cl· 6H₂O and [Fe₃O(CH₃COO)₆(H₂O)₃] [FeCl₄]· 2CH₃COOH. *Journal of Structural Chemistry* **1998**, 39 (5), 747-761.

39. Sowrey, F. E.; Tilford, C.; Wocadlo, S.; Anson, C. E.; Powell, A. K.; Bennington, S. M.; Montfrooij, W.; Jayasooriya, U. A.; Cannon, R. D., Spin Frustration and Concealed Asymmetry: Structure and Magnetic Spectrum of $[\text{Fe}_3\text{O}(\text{O}_2\text{CPh})_6(\text{py})_3]\text{ClO}_4 \cdot \text{py} \dagger$. *Journal of the Chemical Society, Dalton Transactions* **2001**, (6), 862-866.
40. Schneider, C. A.; Rasband, W. S.; Eliceiri, K. W., NIH Image to ImageJ: 25 years of Image Analysis. *Nat. Methods* **2012**, 9 (7), 671-675.
41. Burdett, J. J.; Gosztola, D.; Bardeen, C. J., The Dependence of Singlet Exciton Relaxation on Excitation Density and Temperature in Polycrystalline Tetracene Thin Films: Kinetic Evidence for a Dark Intermediate State and Implications for Singlet Fission. *The Journal of Chemical Physics* **2011**, 135 (21), 214508.
42. Chen, L. X.; Zhang, X., Photochemical Processes Revealed by X-ray Transient Absorption Spectroscopy. *The Journal of Physical Chemistry Letters* **2013**, 4 (22), 4000-4013.
43. Mourdikoudis, S.; Liz-Marzán, L. M., Oleylamine in Nanoparticle Synthesis. *Chemistry of Materials* **2013**, 25 (9), 1465-1476.
44. Kline, C. H.; Turkevich, J., The Vibrational Spectrum of Pyridine and the Thermodynamic Properties of Pyridine Vapors. *J. Chem. Phys.* **1944**, 12 (7), 300-309.
45. Holzwarth, U.; Gibson, N., The Scherrer Equation Versus the 'Debye-Scherrer Equation'. *Nat Nano* **2011**, 6 (9), 534-534.
46. O'Day, P. A.; Rivera, N.; Root, R.; Carroll, S. A., X-ray Absorption Spectroscopic Study of Fe Reference Compounds for the Analysis of Natural Sediments. *American Mineralogist* **2004**, 89 (4), 572.
47. Piquer, C.; Laguna-Marco, M. A.; Roca, A. G.; Boada, R.; Guglieri, C.; Chaboy, J., Fe K-Edge X-ray Absorption Spectroscopy Study of Nanosized Nominal Magnetite. *The Journal of Physical Chemistry C* **2014**, 118 (2), 1332-1346.
48. Waychunas, G. A.; Apter, M. J.; Brown, G. E., X-ray K-edge Absorption Spectra of Fe Minerals and Model Compounds: Near-Edge Structure. *Physics and Chemistry of Minerals* **1983**, 10 (1), 1-9.
49. Goloverda, G.; Jackson, B.; Kidd, C.; Kolesnichenko, V., Synthesis of Ultrasmall Magnetic Iron Oxide Nanoparticles and Study of Their Colloid and Surface Chemistry. *J. Magn. Magn. Mater.* **2009**, 321 (10), 1372-1376.
50. Horcajada, P.; Surble, S.; Serre, C.; Hong, D.-Y.; Seo, Y.-K.; Chang, J.-S.; Greneche, J.-M.; Margiolaki, I.; Ferey, G., Synthesis and Catalytic Properties of MIL-100(Fe), an Iron(III) Carboxylate with Large Pores. *Chemical Communications* **2007**, (27), 2820-2822.
51. Cannon, R. D.; Montri, L.; Brown, D. B.; Marshall, K. M.; Elliott, C. M., Partial Electron Delocalization in a Mixed-Valence Trinuclear Iron(III)-Iron(II) Complex. *Journal of the American Chemical Society* **1984**, 106 (9), 2591-2594.

Chapter 4: Synthetic methods and characterization of transition metal doped MIL-125-NH₂ metal-organic frameworks

4.1 Introduction

Photocatalysis is an active area of research that requires harvesting photons to generate chemical energy that can be used to fuel many reactions. Traditionally, metal oxide-based semiconductors, such as TiO₂, Fe₂O₃, WO₃, ZnO, CeO₂, CdS, ZnS, MoO₃, ZrO₂, and SnO₂, have been studied for their application as photocatalysts¹. Of these, TiO₂ has been proven to be one of the most promising and attractive for a wide range of photocatalytic applications. Titanium dioxide has been widely explored for solar energy relevant photocatalysis applications thanks to its thermodynamically suitable band structure and the reversible photoredox behavior of the Ti centers, which can serve as catalytic sites.²⁻³ Initial work done by Fujishima and Honda explored the first photocatalytic application of TiO₂ for water photolysis⁴. The intrinsically large bandgap and common solid state structures of bulk TiO₂ however, lead to low utilization of the solar energy spectrum, rapid recombination of electron-hole pairs and therefore poor efficiencies⁵. Subsequent research has focused on enhancing the photocatalytic activity of TiO₂ to overcome its shortcomings via doping, dye-sensitization, and metal nanoparticle loading¹. Of these methods, one of the most widely used is transition metal doping. Several reports showed that doping TiO₂ with several transition metals shifted the absorption edge into the visible, thereby increasing photocatalytic ability⁶⁻⁹. To explain these effects, DFT simulations have been employed to understand changes to the band structure upon transition metal doping. Calculations showed that the 3d metal doping largely lowered the valence band or created a mid-gap state and as the atomic number of the dopant increased, so did localization of the photoexcited electron¹⁰.

Inspired by these findings, research has recently begun on the use and design of metal-organic frameworks (MOFs) for photocatalytic applications. In contrast to the semiconductors that were conventionally studied as inorganic photocatalysts, the latest research showed promise in these permanently porous and crystalline, solid state materials composed of metal nodes and organic linkers¹¹⁻¹². The nature of these materials makes them more amenable for intelligent design and therefore can be creatively optimized for a specific application, namely photocatalysis. Of the various reported photocatalytic MOFs, Ti(IV)-based MOFs have been of increasing interest. Inspired by the structure of TiO₂, titanium-oxo based MOFs are regarded to be chemically and structurally stable, inexpensive, redox active, and form structurally stable coordination with a variety of linkers¹³.

The first crystalline carboxylate-based Ti-MOF was reported in 2009, known as MIL-125¹⁴. The framework is composed of cyclic Ti₈O₈(OH)₄(COO)₁₂ octamers with edge- and corner-sharing TiO₅(OH) octahedra, linked by terephthalate (1,4-benzenedicarboxylate) linkers. In the presence of a sacrificial donor, under inert de-aerated conditions, UV irradiation of the MOF produced a white to dark blue color change upon photo-excitation into the ligand-to-metal cluster charge transfer (LCCT) generating a pseudo-stable Ti(III) center as confirmed by EPR spectroscopy.¹⁴ The darker color resulted from a newly created intervalence band and metal-centered d-d transition. The amine-functionalized analogue, MIL-125-NH₂(Ti), containing aminoterephthalate linkers, was synthesized shortly after. The auxochrome-functionalized linker was used to extend the absorption of the MOF into the visible wavelength region, as has been demonstrated for other MOFs such as Zr-oxo based UiO-

66.¹⁵ Further band gap tuning has been attempted by altering the unoccupied frontier orbital energy level by borrowing the concept of heteroatom doping used in semiconductors, such as TiO_2 ¹⁶⁻²⁰. The first report of heterometal-doping in MIL-125-NH₂ involved incorporation of Cu(II) sites through a direct synthesis method.¹⁹ The authors reported improved photocatalytic capability of the Cu-doped MOF compared to the parent and ascribed this phenomenon to enhanced visible light absorption. Recent computational work predicts that substitution of certain heterometals at the Ti sites effectively produces more localized charge-separated excited states as electron density on the metal-oxo clusters is increased.²¹ As experimental verification of these theoretical findings, the authors also report a series of V-doped MIL-125-NH₂ MOFs with different loading percentages obtained via a similar direct synthesis route as in the Cu-doped version. In both these examples, XRD characterization revealed structures consistent with the MIL-125 topology but a dearth of evidence is presented for the presumed location of the metal dopant within the metal-oxo core.

This chapter focuses on expanding the set of transition metal-doped MIL125-NH₂ MOFs and providing evidence for the nodal cluster coordination of the heterometal. The series, as illustrated in figure 4.1 will be used as part of a systematic evaluation of heterometal dopant-induced MOF electronic structure changes.

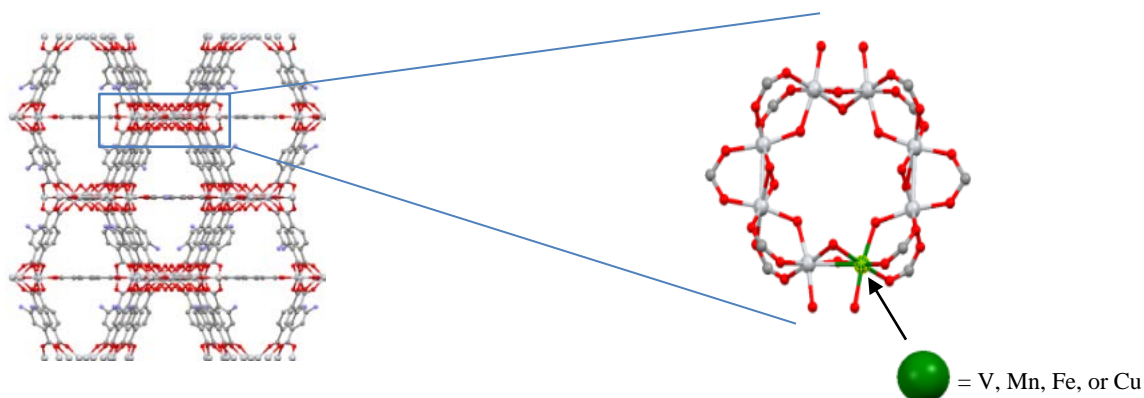


Figure 4.1 Structure of MIL-125-NH₂, highlighting the octameric core containing the dopant (V, Mn, Fe, or Cu).

However, before these trends can be evaluated, a synthetic protocol for direct incorporation of a heterometal into the titanium cluster must be established. A number of different synthetic approaches have been studied for heterometal doping of MOF materials and these have been a topic of a few reviews²²⁻²⁴. Of the reported methods, the three general synthetic strategies are: use of organic ligands with additional metal binding sites, post-synthetic metal exchange, or one-pot synthesis using multiple metal precursors²³. Direct synthesis of mixed metal MOFs using metalloligands, such as in porphyrin chemistry, allows for metals sites to be at the metal node or embedded within the linker²⁴. However, for the purposes of studying the impact of a heterometal on a ligand-to-cluster charge transfer, it is preferred to have physical distance between the antenna and the electron sink.

Transmetalation, or post-synthetic metal exchange is a doping method that involves incorporation of substitution of metal cations after synthesis of the homonuclear MOF. The procedure generally involves immersing the parent MOF in a saturated solution of the heterometal salt²³. However, this doping procedure suffers from slow exchange rates, requiring long immersion times and therefore the additional issue of unpredictable loading amounts of the dopant metal²². For the purpose of studying the impact of a heterometal on the photoactivity generated by exciting into a LCCT electronic transition, it is necessary to have control over the position and loading percentage of the dopant metal within the framework. Furthermore, it is imperative to confirm true integration of

the heterometal within the MOF framework, rather than as metal nanoparticles or metal salt impurity co-crystallized with the parent MOF. Consequently, a one-pot synthesis to generate multi-metal MOFs proved to be the most promising method of direct heterometal incorporation. Direct synthesis requires that appropriate ratio mixtures of the different metal precursors are used during the synthesis of the MOF. While this method is more straightforward, it requires that the two metals, as well as the linker, are compatible to form the bimetallic MOF and that the heterometal is similar in ionic radius, charge density, and softness/hardness to the homonuclear MOF metal center/cluster.

In this chapter, the synthesis of MIL-125-NH₂ doped with V(III), Mn(II), Fe(III), and Cu(II) has been adapted using a one-pot direct synthetic method with doping ratios that stoichiometrically amount to one heterometal per Ti-oxo cluster. First row transition metals were selected based on the hard-soft acid basis theory with a comparable polarizability of 2.438 (based on anatase TiO₂)²⁵, as well as, comparable ionic radius (0.42 Å)²⁶. The initial focus is to prove successful incorporation of the heterometal in the Ti-cluster while maintaining the MIL125 topology and characterize the coordination environment. For comparison, transmetallation via post-synthetic metal exchange reaction was attempted for two of these transition metal doped frameworks, Cu(II) and Fe(III). Finally, the electronic structure is evaluated using UV/VIS Diffuse Reflectance as a first step in a systematic study to experimentally understand how the heterometal affects the LCCT electronic structure and dynamics.

4.2 Experimental Methods

4.2.1 Materials and Synthesis

4.2.1.1 Materials

Dry methanol, dry dimethylformamide (DMF), and anhydrous metal chloride (VCl_3 , MnCl_2 , FeCl_3 , CuCl_2) dissolved in dried solvents, were further dried over molecular sieves prior to use. Titanium (IV) tert-butoxide ($\text{Ti}(\text{OC}_4\text{H}_9)_4$), and 2-aminoterephthalic acid ($\text{NH}_2\text{-BDC}$), were used without further purification.

4.2.1.2 Synthesis

MIL-125- $\text{NH}_2(\text{Ti})$ was synthesized according to literature precedent with a slight modification¹⁹. 0.26 mL of $\text{Ti}(\text{OC}_4\text{H}_9)_4$ was measured into a Schlenk flask in a glove box. To the Schlenk flask, outside the glove box, 0.504 g of $\text{NH}_2\text{-BDC}$, 12.1 mL DMF and 1.4 mL methanol were added to the Schlenk flask under the flow of N_2 . The solution was sonicated for 30 minutes and then a spatula tip full of CTMAB was added. The reaction mixture was then transferred to a Teflon-lined autoclave and heated to 150°C for 24 hours. The MOF was then centrifuged and resuspended with DMF and methanol 3 times. The supernatant was decanted after each washing.

MIL125- $\text{NH}_2(\text{Ti}, \text{M})$, targeting one heterometal/cluster doping level, was synthesized using a similar procedure to the parent, however, anhydrous metal chloride was combined with the linker and the solvents. Similarly, 0.26 mL of $\text{Ti}(\text{OC}_4\text{H}_9)_4$ was measured into a Schlenk flask in a glove box. Outside the glove box, a stoichiometric amount (7:1 Ti:M molar ratio) of anhydrous metal chloride dissolved in 12.1 mL DMF and 1.4 mL methanol was added to the Schlenk flask along with , 0.504 g $\text{NH}_2\text{-BDC}$ under constant flow of N_2 gas. The reaction mixture was then transferred to a Teflon-lined autoclave and heated to 150°C for 24 hours. The MOF was then centrifuged and resuspended with DMF and

methanol 3 times. The supernatant was decanted after each washing. Synthesis of MIL125-NH₂(Ti,Cu) and MIL125-NH₂(Ti,Fe) via a transmetallation was attempted by first activating the as-synthesized MIL-125-NH₂(Ti) under vacuum at 160°C for 24 hours. The activated framework was transferred, under N₂ gas, to a scintillation vial. Dry methanol was saturated with the anhydrous metal salt (CuCl₂ or FeCl₃) and added to the vial and stirred for 20 minutes. After soaking in the undisturbed vial for 7 days, the samples were isolated by centrifugation and washed three times with methanol and DMF to remove excess salt.

4.2.2 Characterization and Methods

4.2.2.1 Characterization

Powder XRD patterns were recorded using a Bruker D8 ADVANCE ECO Diffractometer. Steady-state electronic absorption spectra were collected using a Cary Varian UV–visible–near-infrared (NIR) spectrophotometer. Solid-state powder samples were ground thoroughly and measured undiluted using a Diffuse Reflectance accessory (Harrick Scientific). Solution based measurements were conducted in a 2mm cuvette. Samples were suspended in acetonitrile and centrifuged at 2.5 krpm for 20 minutes. This washing procedure was repeated 7 times to ensure no residual linker was left.

4.2.2.2 X-ray absorption Spectroscopy

X-ray absorption data were collected at the V K-edge (5465 eV), Mn K-Edge (6539 eV), Fe K-edge (7112 eV), and Cu K-edge (8979 eV) at Beamline 8-ID (ISS) at the National Synchrotron Light Source II at Brookhaven National Laboratory using a damping wiggler source and Si(111) double crystal monochromator. The monochromatic

beam spot size was 1 mm. A metal foil was used as the reference for energy calibration. Powder MOF samples were measured undiluted in fluorescence mode using a passivated implanted planar silicon (PIPS) fluorescence detector and Z-1 filters. All data were collected at room temperature. Thirty continuous-scan spectra were collected, each with 1 minute total acquisition time, and averaged. No more than 10 scans were collected on one spot to minimize x-ray damage. Negligible X-ray damage was observed with sequential scans within 10 scans per spot.

Ti K-edge (4966 eV) X-ray absorption data were collected, in transmission mode, at 9-BM at Advanced Photon Source (APS) at Argonne National Lab using a Si(111) crystal monochromator. The monochromatized beam was generated with a 500 μ m x 500 μ m spot size. A Ti-metal foil was used as a reference for energy calibration. All samples were measured undiluted and data was collected at room temperature.

4.3 Results and Discussion

4.3.1 XRD

Following the synthesis of MIL-125-NH₂(Ti) and the transition metal doped frameworks, MIL125-NH₂(Ti,M) using both direct synthesis and transmetallation procedures, the crystallinity and phase of each MOF sample was evaluated using powder X-ray diffraction (XRD), as shown in Figures 4.2 through 4.8.

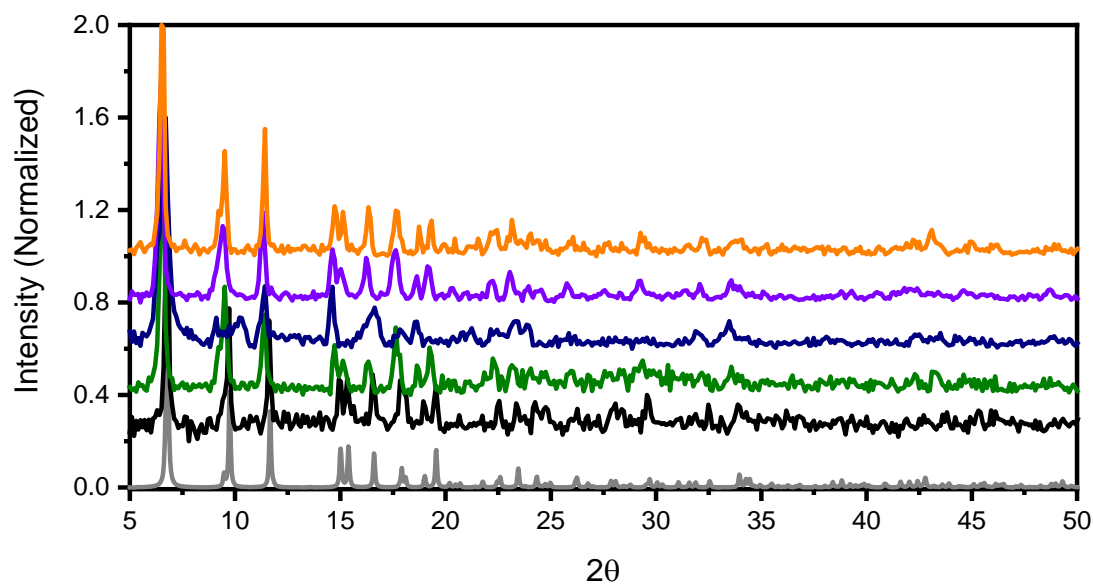


Figure 4.2 Powder X-ray diffraction of MIL-125 simulated¹⁴ (gray), MIL-125-NH₂(Ti) (black), MIL-125-NH₂(Ti,V) (green), MIL-125-NH₂(Ti,Mn) (navy), MIL-125-NH₂(Ti,Fe) (purple), and MIL-125-NH₂(Ti,Cu) (orange). Diffraction patterns are offset for clarity.

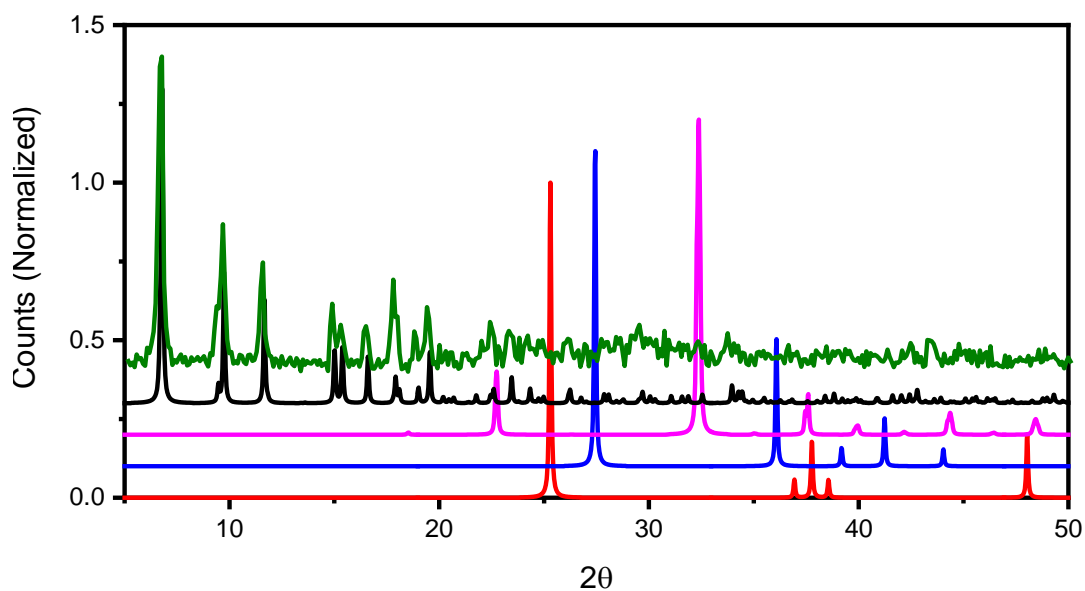


Figure 4.3 Powder X-ray diffraction of MIL-125 simulated¹⁴ (black), TiO₂ anatase (red), TiO₂ rutile (blue), V₂O₃ (pink), and MIL-125-NH₂(Ti,V) (green)

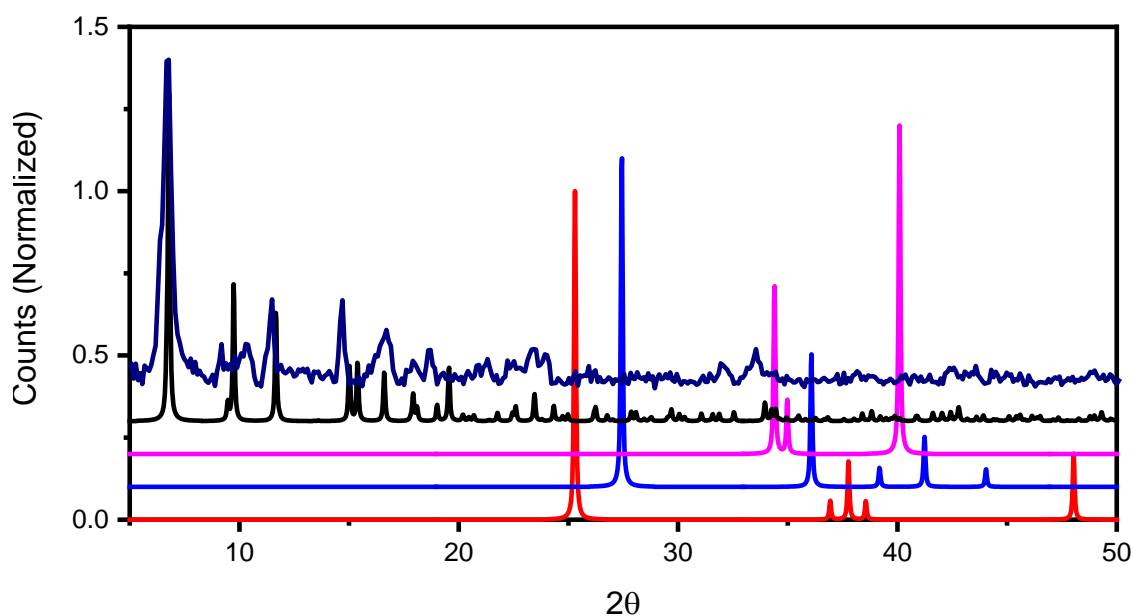


Figure 4.4 Powder X-ray diffraction of MIL-125 simulated¹⁴ (black), TiO₂ anatase (red), TiO₂ rutile (blue), MnO (pink), and MIL-125-NH₂(Ti,Mn) (navy)

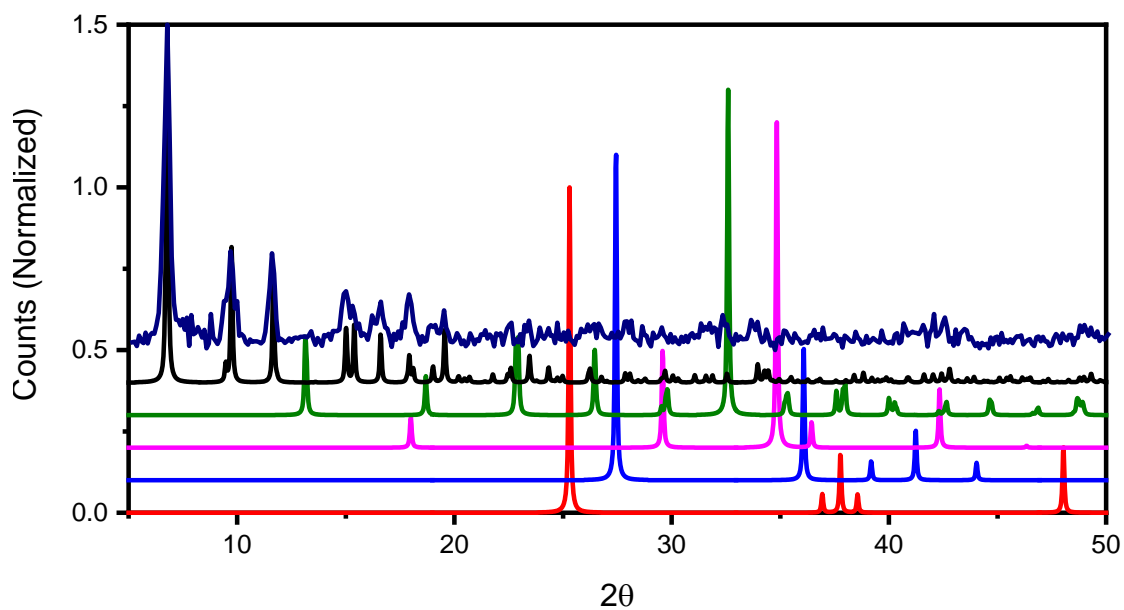


Figure 4.5 Powder X-ray diffraction of MIL-125 simulated¹⁴ (black), TiO₂ anatase (red), TiO₂ rutile (blue), Fe₃O₄ (pink), Fe₂O₃ (green), and MIL-125-NH₂(Ti,Fe) (purple)

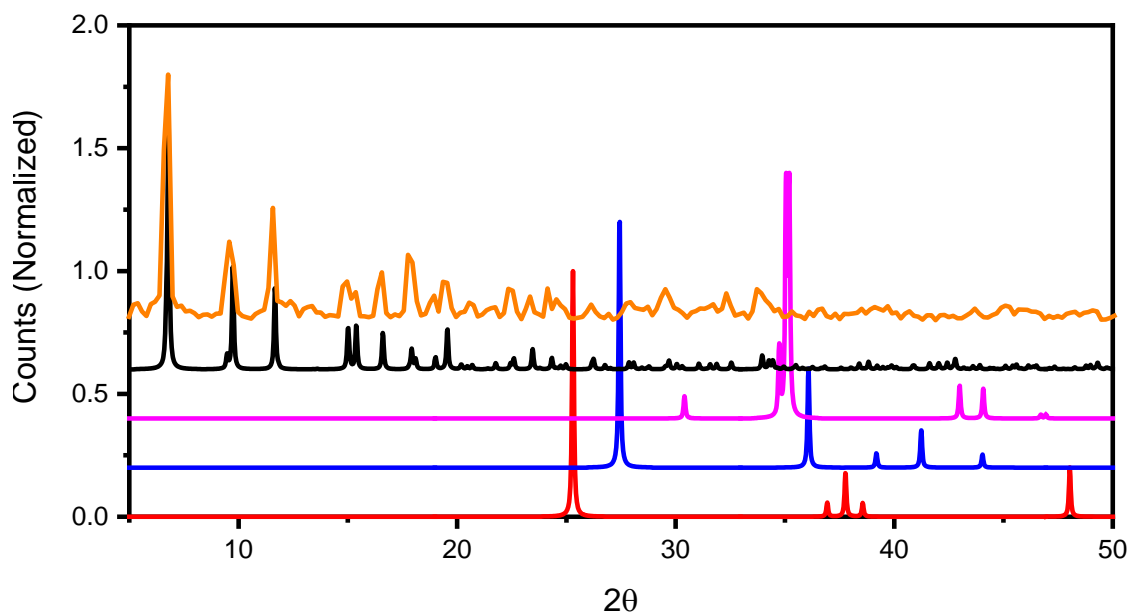


Figure 4.6 Powder X-ray diffraction of MIL-125 simulated¹⁴ (black), TiO₂ anatase (red), TiO₂ rutile (blue), CuO (pink), and MIL-125-NH₂(Ti,Cu) (orange)

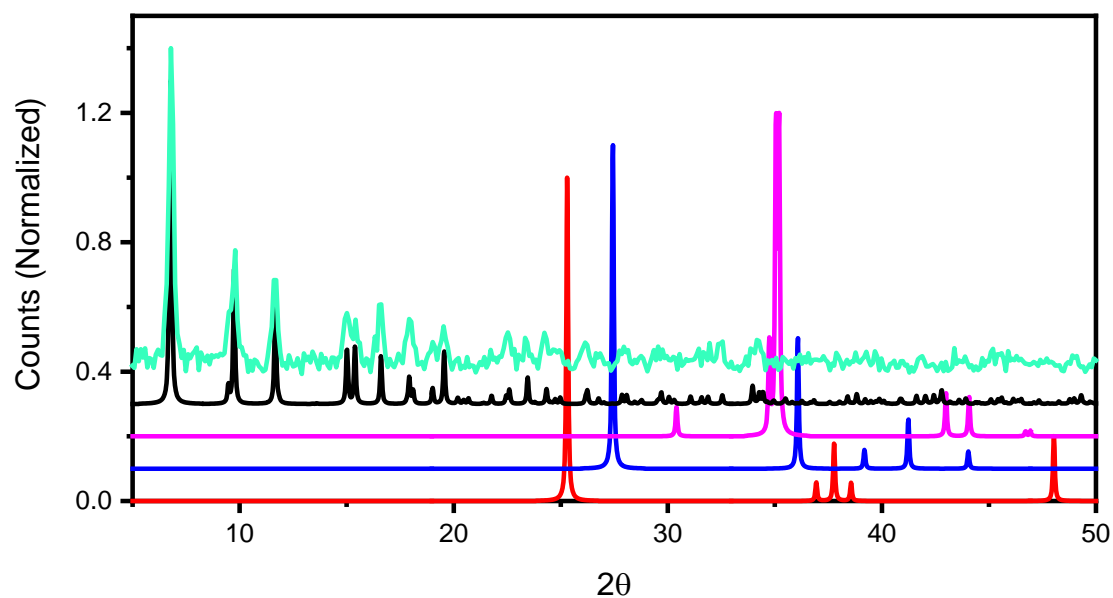


Figure 4.7 Powder X-ray diffraction of MIL-125 simulated¹⁴ (black), TiO₂ anatase (red), TiO₂ rutile (blue), CuO (pink), and CuCl₂ soaked MIL-125-NH₂ (turquoise)

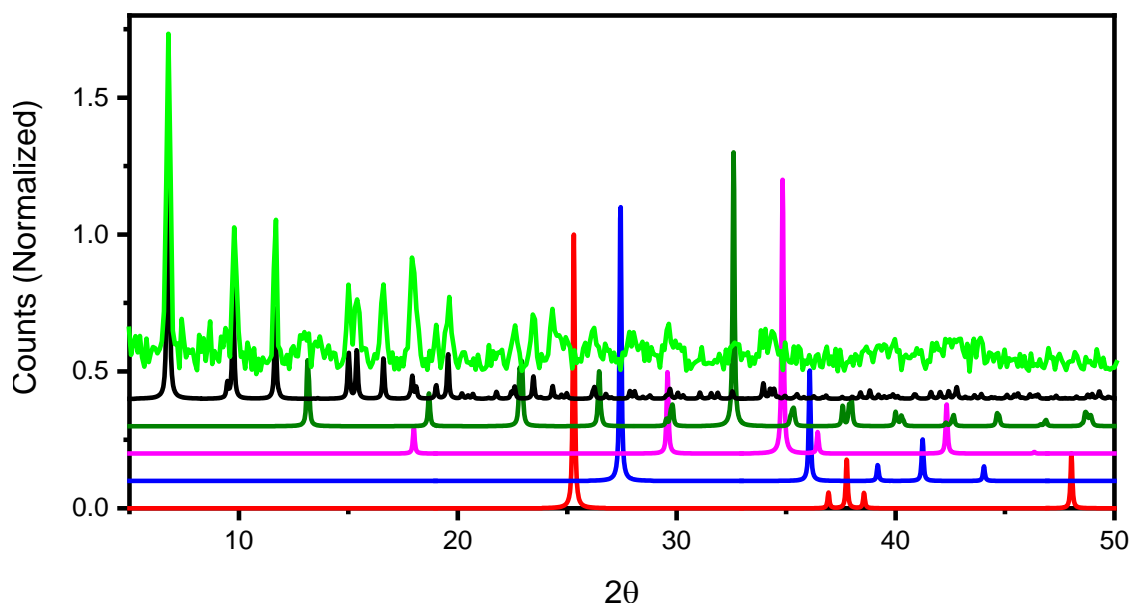


Figure 4.8 Powder X-ray diffraction of MIL-125 simulated¹⁴ (black), TiO₂ anatase (red), TiO₂ rutile (blue), Fe₃O₄ (pink), Fe₂O₃ (green) and FeCl₃ soaked MIL-125-NH₂ (lime green)

As seen in the XRD comparisons, the diffraction patterns of the doped MOFs obtained via direct synthesis generally match that of the parent MIL-125-NH₂(Ti) framework and the pattern simulated from the reported MIL-125 crystal structure,¹⁴ with some minor discrepancies in the case of the Mn-doped MOF. The inconsistencies seen in MIL-125-NH₂(Ti, Mn) may indicate some contribution of the heteroatom-induced structural distortion or mixed phase. Additionally, the XRD patterns of the Cu and Fe-doped MIL125-NH₂ frameworks obtained via post-synthetic modification methods match closely to those obtained via direct synthesis, indicating that the structures are preserved

upon extended soaking in the saturated heterometal ion solutions. Furthermore, comparing each of the MOF experimental XRD patterns with those of several metal oxide materials confirms the absence of these common side products and the purity of the MOF structures.

4.3.2 X-Ray Absorption Spectroscopy

X-ray absorption spectroscopy (XAS) is a powerful, element-specific technique that can be used to probe the geometry, coordination environment, and oxidation state of the element of interest. We used XAS, measured at both the Ti and the corresponding heterometal K-edges, to shed light on the electronic and geometric structures of the metal sites in the MIL-125-NH₂(Ti,M) frameworks.. The Ti K-edge X-ray absorption near edge spectra (XANES) of the parent MIL-125-NH₂(Ti) compared to TiO₂ are shown in Figure 4.9. The similarity in edge position of TiO₂ compared to the MOF confirms that Ti centers are +4 oxidation state. Furthermore, MIL-125-NH₂ exhibits a pre-edge structure containing 3 prominent features due to quadrupolar and dipolar transitions on the Ti metal center that are a signature of hexacoordinated Ti-oxo distorted octahedra²⁷. Although the energy of the pre-edge features are similar for MIL-125-NH₂ and TiO₂, the intensities are quite different. The increased intensity in the pre-edge feature for MIL-125-NH₂ most likely reflects a more distorted octahedral geometry than that of TiO₂.

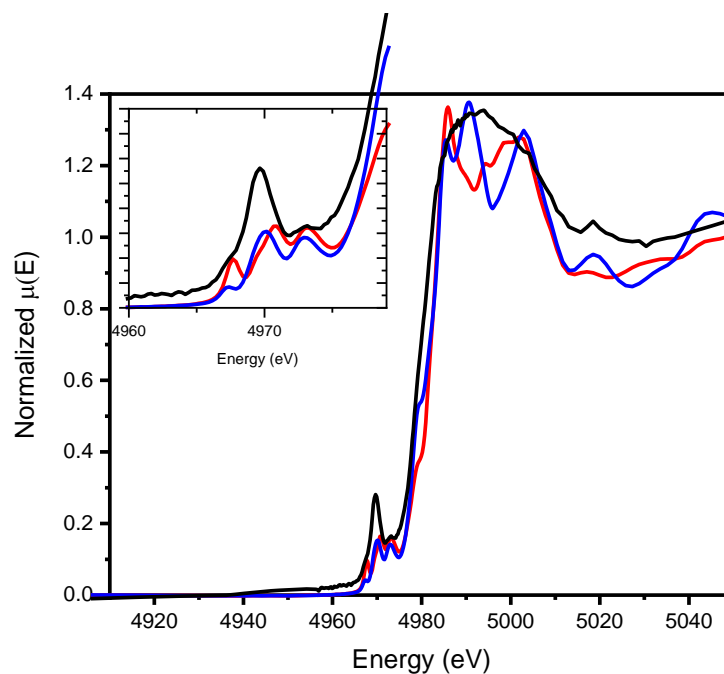


Figure 4.9 Ti K-edge XAS of MIL-125-NH₂(Ti) (black), TiO₂ anatase (red), and TiO₂ rutile (blue)

Further insights on the average local coordination of the Ti sites can be provided through comparison of the Ti K-edge extended X-ray absorption fine structure (EXAFS) spectra. The EXAFS spectrum, plotted in R space of MIL-125-NH₂(Ti) is shown in Figure 4.10, as well as a few representative single scattering paths.

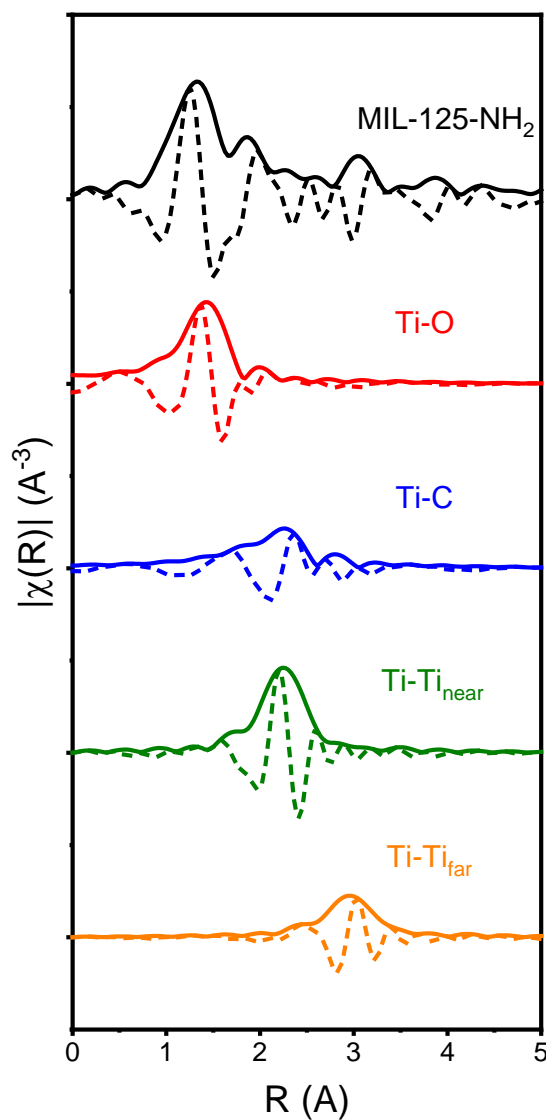


Figure 4.10 Experimental EXAFS of MIL-125-NH₂ with calculated scattering paths plotted in R space

The calculated scattering paths were generated using FEFF in the program Artemis²⁸ using the MIL-125 crystal structure¹⁴. The comparison between the experimental spectra and generated paths indicates that the first shell is dominated by contribution from the oxygen scattering paths. The second shell mainly arises from carbon and the nearest Ti scattering paths. The farther adjacent Ti center primarily

contributes to the third shell feature. The structural ramifications of the transition metal doping can also be probed using Ti K-edge XAS. The XANES of MIL-125-NH₂(Ti) and MIL-125-NH₂(Ti, M) MOFs collected at the Ti K-edge are shown in Figure 4.11. All display nearly identical pre-edge features to one another, suggesting Ti(IV) centers with similar electronic structure and geometry. Therefore, the similarity between the XANES of the doped and undoped MOF samples indicates that upon heterometal incorporation, there is no significant change to the local geometry or oxidation state of the Ti centers. However, because the spectrum represents an average over all the Ti centers in the octameric ring, the technique is not sensitive to slight distortions of geometry associated with the substitution of one Ti metal with a heterometal. Despite this, it appears that the inclusion of the heterometal does not further alter the pre-edge features and therefore the average electronic structure of the Ti sites.

Figure 4.12 depicts Ti K-edge EXAFS spectra of MIL-125-NH₂(Ti), and the transition metal-doped versions, with the exception of MIL-125-NH₂(Ti,V). Collection of the EXAFS spectrum for this MOF was not possible due to the proximity of the V K-edge (5465 eV) which severely limited the Ti K-edge (4966 eV) data collection energy range. For the remaining MIL-125-NH₂(Ti,M) MOFs, for which Ti-K-edge EXAFS spectra were collected, their comparison shows similar peaks, indicating comparable local environments about the Ti sites. The Mn-doped MIL-125-NH₂ exhibits the greatest deviation among the MOFs, possibly due to greater disorder. This observation is in agreement with the XRD characterization, which also suggested greater disorder in the Mn-doped MOF.

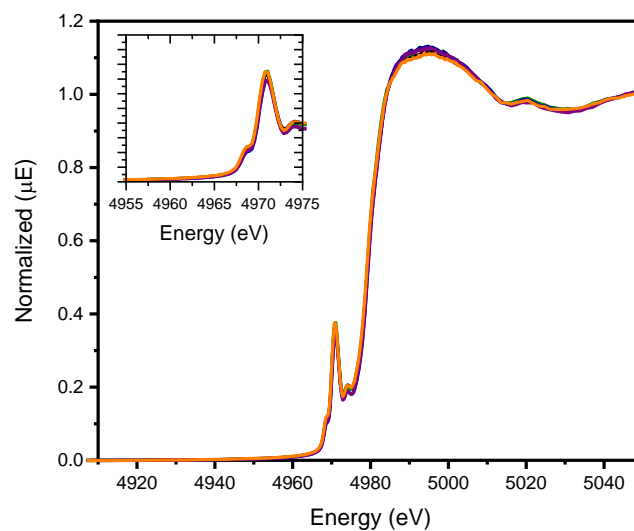


Figure 4.11 Ti K-edge XAS of MIL-125-NH₂ (black), V-doped MIL-125-NH₂ (green), Mn-doped MIL-125-NH₂ (navy), Fe-doped MIL-125-NH₂ (purple), and Cu-doped MIL-125-NH₂ (orange).

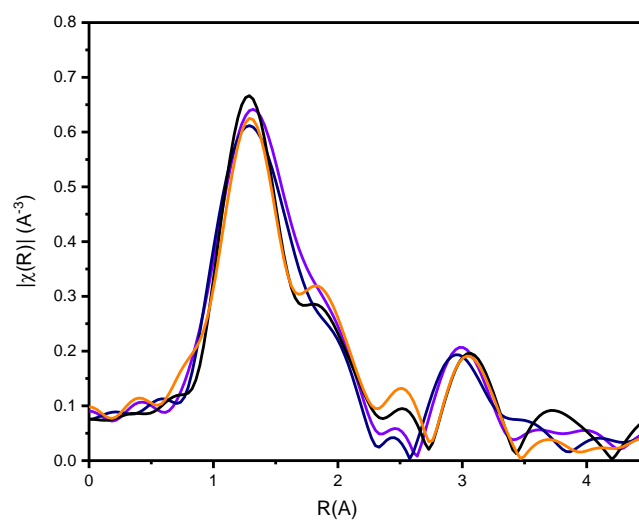


Figure 4.12 Ti K-edge EXAFS plotted in R space of MIL-125-NH₂ (black), Mn-doped MIL-125-NH₂ (navy), Fe-doped MIL-125-NH₂ (purple), and Cu-doped MIL-125-NH₂ (orange).

In order to gain more information on the surrounding geometry of the dopant metal and confirm true incorporation into the framework, XAS measurements were conducted at the corresponding heterometal K-edges. XANES spectra can reveal coordination geometry and oxidation state of the dopant metal, providing information on the local coordination environment and evidence for direct incorporation in the MOF. Comparison with standards of alternative oxidation states or known chemical environment can be used to understand the spectral features, as well as, make assessment of dopant metal speciation ²².

To confirm the coordination environment and oxidation state of the heterometal in MIL-125-NH₂(Ti,Cu) , the Cu K-edge spectra were measured for this MOF and several reference materials as shown in Figure 4.13. These references represent possible alternative ways Cu could incorporate in MIL-125-NH₂(Ti); as CuO , the starting material metal chloride, CuCl₂, or as Cu(0) nanoparticles. The spectrum of the MIL-125-NH₂(Ti,Cu) resembles closely to what has been reported for Cu(II) doped TiO₂²⁹. The edge features and white line shape are used to diagnose the oxidation state and coordination geometry of the Cu dopant. As shown in Figure 4.13, the edge position of the Cu-doped MOF closely matches that of CuO and other previously published Cu(II) octahedral species while the white line intensity is quite different²⁹. The edge position differs from that of the starting material, CuCl₂, despite having the same oxidation state because of differences in coordination geometry which can affect the shape and position of the rising edge. ,

The Cu K-edge EXAFS region provides further indication of the coordination of the Cu in the directly synthesized Cu-doped MOF. MIL-125-NH₂(Ti,Cu) has a feature in the first coordination shell similar to that found in CuO which has been assigned to the Cu-O scattering path³⁰. However, the Cu-Cl and Cu-Cu scattering paths are clearly absent from the MOF. Additionally, the rest of MIL-125-NH₂(Ti,Cu) scattering peaks, outside the Cu-O scattering, do not match any of the other references. Therefore, this EXAFS comparison indicates that the Cu in the MOF does not exist as CuO, Cu metal nanoparticles, or CuCl₂.

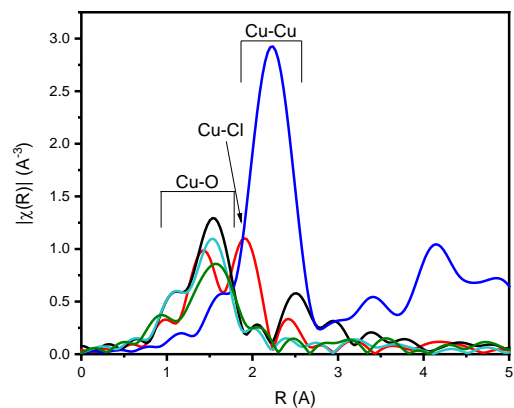
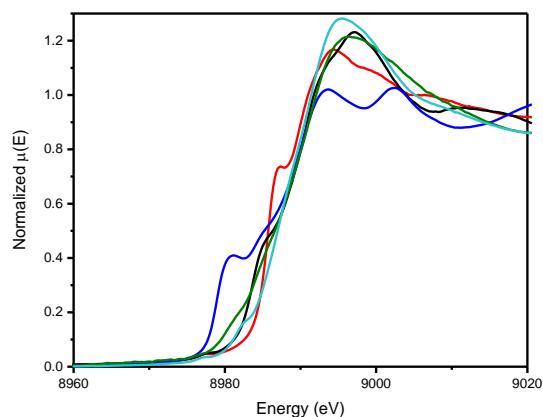


Figure 4.13 Left Cu K-edge XANES and Right: EXAFS plotted in R space of CuO (black), CuCl₂ (red), Cu foil (blue), MIL-125-NH₂(Ti,Cu) (green), and CuCl₂ soaked MIL-125-NH₂ (turquoise).

Figure 4.14 shows the normalized Fe K-edge XANES spectra of MIL-125-NH₂(Ti,Fe) and corresponding Fe reference materials. The doped MOF is compared to Fe₂O₃ the starting metal chloride, FeCl₃, and iron metal. This comparison provides evidence that the Fe(III) centers are truly incorporated into the titanium-oxo clusters of the MOF. As seen in the inset of Figure 4.14, the pre-edge feature of the doped MOF resembles that of Fe₂O₃, showing a nearly unresolved low intensity, doublet feature due to the excitation into the two sets of d orbitals split by an octahedral field, indicating a similar octahedral coordination environments of the Fe centers in these materials. Additionally, the energy of the rising edge of the MOF spectrum, as compared to the reference spectra, confirms that the Fe dopant is in the +3 oxidation state within the MOF.

Qualitative assessment of the EXAFS indicates the first coordination shell of the MOF is similar to that of the Fe₂O₃; this peak has been previously assigned to be primarily due to Fe-O scattering³¹. The Fe-Fe and Fe-Cl scattering paths are absent in the MOF which is consistent with the XANES results, indicating that the Fe centers are likely incorporated in cluster sites within the framework rather than as these possible contaminants.

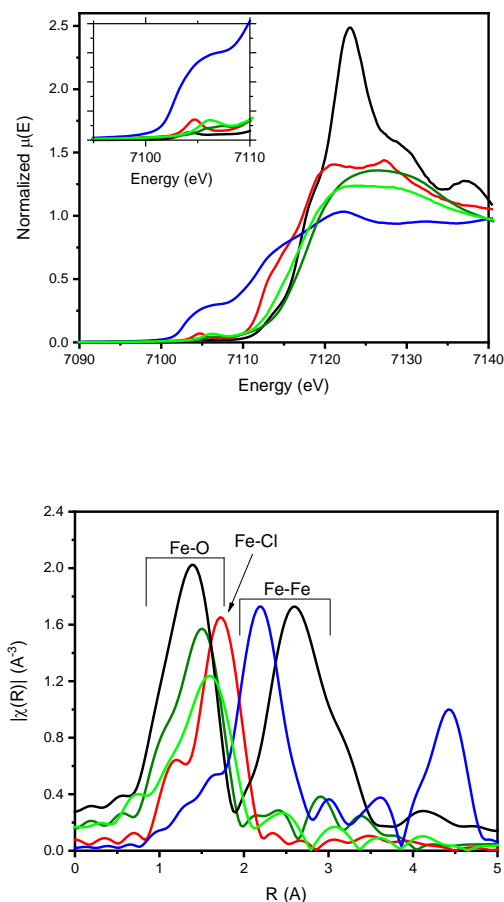


Figure 4.14 Left Fe K-edge XANES and Right: EXAFS plotted in R space of Fe₂O₃ (black), FeCl₃ (red), Fe foil (blue), and MIL-125-NH₂(Ti,Fe) (light green).

Figure 4.15 shows the normalized Mn K-edge XANES spectra of the MIL-125-NH₂(Ti, Mn) and corresponding Mn materials representing possible other ways in which Mn could be incorporated into the framework, namely as an oxide, MnO, the starting metal chloride, MnCl₂, or metallic manganese nanoparticles. The pre-edge feature of the doped MOF resembles that of MnO and MnCl₂, revealing a low intensity, broadened, doublet feature, confirming that dopant is in a similar octahedrally coordination environment as the Mn(II) sites of the standards²⁷⁻²⁹. However, the shape of the

absorption edge for the MIL-125-NH₂(Ti,Mn) differs compared to the MnO or MnCl₂, indicating that the Mn incorporated into the framework is not in the form of these species. For Mn(II), the centroid position of the pre-edge feature is oxidation state diagnostic. Because the position of the pre-edge feature for MIL-125-NH₂(Ti,Mn) appears at an identical energy as the Mn(II) standards, we can conclude that the Mn(II) site is in the +2 oxidation state³².

The EXAFS shown in Figure 4.15 can provide further insight on the neighboring atoms to the Mn dopant. The peaks present in MIL-125-NH₂(Ti,Mn) in the first coordination shell are similar to that seen in the MnO standard, which has been previously assigned to the Mn-O scattering paths and suggests that the Mn may be directly incorporated into the MOF.

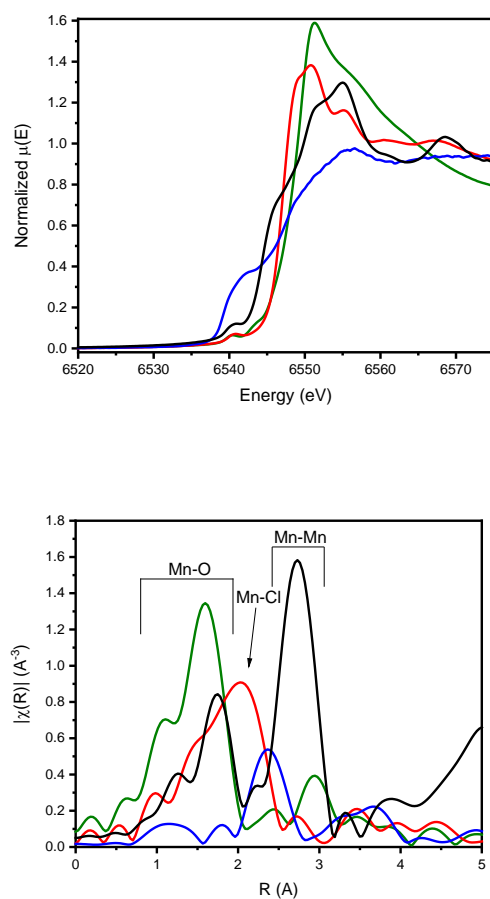


Figure 4.15 Left Mn K-edge XANES and Right: EXAFS plotted in R space of MnO (black), MnCl₂ (red), Mn foil (blue), and MIL-125-NH₂(Ti,Mn) (green)

Figure 4.16 shows the normalized V K-edge XANES spectra of MIL-125-NH₂(Ti,V) and corresponding V materials representing possible other ways in which V could be incorporated into the framework; the starting metal chloride, VCl₃ and vanadium metal. Due to toxicity issues, V₂O₃ and V₂O₄ could not be measured, but the reported spectra have an edge energy at 5475.0 and 5478.1³³ eV and a pre-edge feature at 5469.1 and 5470.4³⁴ eV, respectively³⁵. The similarity of the pre-edge feature in the

spectrum of the MOF with that of V_2O_4 as well as VCl_3 signify a comparably octahedrally coordinated V center.³⁶ However, the shift in the edge to higher energy, compared to that of the VCl_3 indicates V(IV) oxidation state. .

The EXAFS spectrum shown in Figure 4.16 is somewhat inconclusive. Clearly, the V-V scattering path, seen in the V foil, is absent in the MIL-125- $\text{NH}_2(\text{Ti},\text{V})$. However, because the V_2O_3 was not measured, comparison of those scattering paths, which may indicate first shell coordination to oxygen, cannot be determined. Despite this, the EXAFS of MIL-125- $\text{NH}_2(\text{Ti},\text{V})$ appears quite different than that of VCl_3 or V foil, indicating the V species is different than these two alternative coordination environments. .

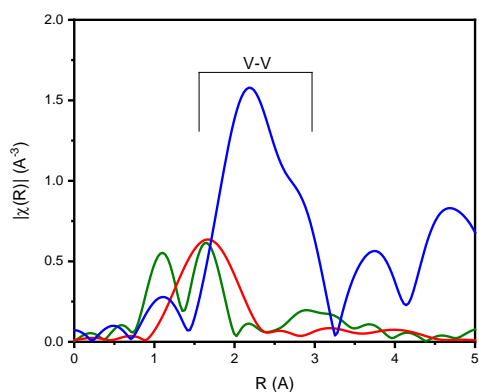
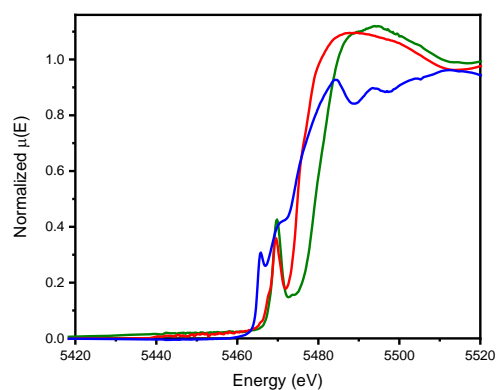


Figure 4.16 Left V K-edge XANES and Right: EXAFS plotted in R space of VCl_3 (red), V foil (blue), and MIL-125- $\text{NH}_2(\text{Ti}, \text{V})$ (green)

XAS characterization at either the Fe or Cu K-edge of the MOFs that underwent post synthetic treatments with Fe(III) and Cu(II) in attempts to dope the metal-oxo clusters via transmetallation are shown in Figures 4.14 and 4.13. Comparison with the direct synthesis versions of the Cu doped framework shows slightly altered pre-edge and edge positions of the post-synthetically doped Cu-MOF, however the edge features in the two spectra differ. The EXAFS reveals nearly identical peaks in the first two shells for CuO and post-synthetically doped MOF. However, the Cu-Cl and Cu-Cu scattering paths are absent in the CuCl_2 soaked MOF. The analysis of speciation of the Cu in the transmetallated MOF is not as straightforward as the direct synthesis MOF, however, the XAS data suggests that there could be mixed phases of Cu within the MOF.

The Fe(III) post-synthetically doped MOF XANES included in the overlay in Figure 4.14 has an edge that is shifted to lower energy compared to the direct synthesis MOF, potentially indicating a reduction of the iron. However, the low intensity, double feature pre-edge suggests that the iron site is in an octahedral coordination environment. Comparison of the EXAFS shows that the first two coordination shells in the transmetallated MOF are due to Fe-O scattering, as seen in the Fe_2O_3 or the direct synthesis MOF. Like the direct synthesis MOF, there is an absence of the Fe-Fe scattering peak, indicating that the Fe in the MOF does not exist as Fe metal nanoparticles or Fe_2O_3 . However, due to the edge shift seen in the XANES, it's possible

that the Fe in the post-synthetically doped MOF is a different speciation than that in the direct synthesis.

Upon qualitative comparison of the scattering peaks in the experimental spectra of the transition metal doped MIL-125-NH₂ with the MIL-125-NH₂(Ti), shown in Figure 4.17, it seems probable the heterometals in all the MOFs, with the except of vanadium, are in a similar coordination environment to the coordination of the titanium sites in the parent MOF. In the first coordination shell, each of the MOFs displays a similar peak, likely due to the metal-oxygen scattering. Notably, the peak position in the heterometal doped MOFs appear at slightly different scattering distances compared to that of the MIL-125-NH₂(Ti) spectrum. This shift signifies differences in metal-oxygen bond lengths. The longer distance seen in the MIL-125-NH₂(Ti,Fe) is expected based on the typical range of reported Fe-O bond lengths (1.94–2.12 Å)³⁷ compared to Ti-O bond lengths (1.94 Å).³⁸ All other metal dopants show a similar increase in first shell distance.

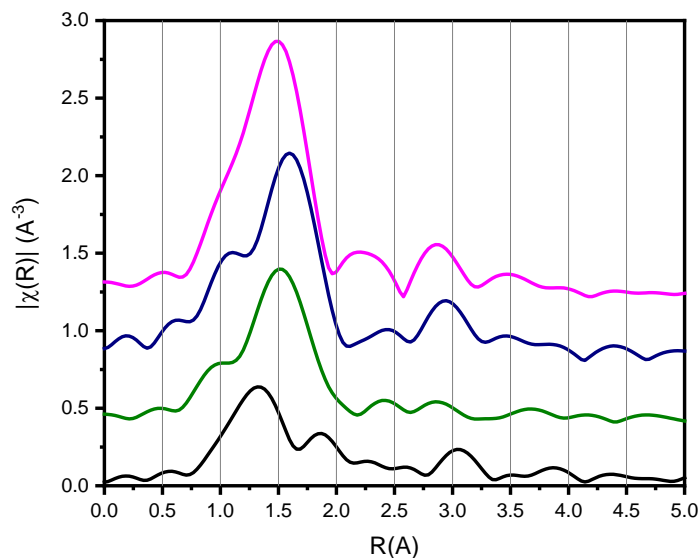


Figure 4.17 Experimental EXAFS spectra plotted in R space of MIL-125-NH₂(Ti) (black), MIL-125-NH₂(Ti,Mn) (navy), MIL-125-NH₂(Ti,Fe) (pink), and MIL-125-NH₂(Ti,Cu) (green).

4.3.3 Optical Electronic Absorption Spectroscopy

The optical electronic absorption spectra for the MOF materials were obtained through UV/vis diffuse reflectance (DR) measurements of the solid-state powders as shown in Figure 4.18. These MOFs all exhibit a similar absorption spectrum with a $n \rightarrow \pi^*$ transition of the aminated linker with peak maxima just below 400nm that takes on LCCT character upon incorporation in the MOF as evidenced by additional intensity in the visible region³⁹. This feature appears further red shifted in the doped MOF spectra, as highlighted by comparison of the spectra with those of the parent MIL-125-NH₂(Ti) framework as well as the NH₂- BDC linker. While the red shift of the feature indicates a lower energy state that is likely localized on the heterometal, periodic trends are difficult to establish at this stage given the broad, poorly resolved spectra and different sample-dependent scattering signal contributions.

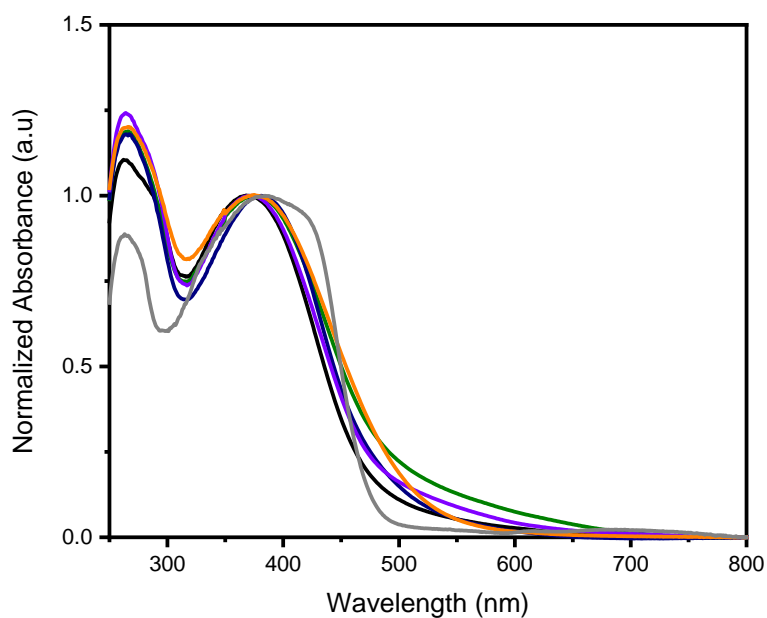


Figure 4.18 UV/VIS Diffuse Reflectance spectra of MIL-125-NH₂(Ti) (black), 2-aminoterephthalic acid (gray), MIL-125-NH₂(Ti,V)(green), MIL-125-NH₂(Ti,Mn) (navy), MIL-125-NH₂(Ti,Fe) (purple), and MIL-125-NH₂(Ti,Cu) (orange).

4.4 Conclusion

In this chapter, MIL-125-NH₂(Ti) was successfully doped via the one pot method using V(III), Mn(II), Fe(III), and Cu(II) chloride salt precursors. To synthesize each sample, a stoichiometric amount of the transition metal salt was added to the synthesis targeting a framework with 1 heterometal site substituting a Ti(IV). The crystallinity of each new

MOF was confirmed using PXRD and the structure was consistent with the parent MIL-125-NH₂(Ti).

Further structural insight was provided by qualitative analysis of the X-ray absorption spectra at the Ti and heterometal K-edges. Comparison of the heterometal K-edge XANES region indicated that the dopants were unique with respect to the possible contaminants. The pre-edge and edge position, as well as the shape of the spectra for each heterometal, with the exception of V, were consistent with a distorted octahedral coordination environment with the presumed oxidation state. Further evidence of the inclusion of the dopant metal into the titanium-oxo cluster was seen in the EXAFS region of the spectrum. Qualitative assessment of each of the scattering paths within the first three coordination spheres confirmed that it is probable that the heterometal is octahedrally coordinated to six oxygens, with two neighboring Ti centers, such as found for each titanium site in the homonuclear MOF. Given these results, we were able to reasonably conclude, except in the case of V, that the coordination and geometry of the heterometal indicated true incorporation of the metal into the titanium-oxo cluster.

Beyond analysis of the location of the dopant metal in the framework, we preliminarily explored the impact of the heterometal center on the electronic nature of the MOF. Previously, the electronic spectrum of the parent MIL-125-NH₂(Ti) has been reported to have a ligand-to-cluster charge transfer (LCCT) transition extending from the UV to visible region of the spectrum⁴⁰. To date, the electronic impact of a dopant on the LCCT state has not been investigated. While the true nature of the LCCT state in response to doping is a topic of chapter 5 of this thesis (for the Fe-doped version), we observed changes in the electronic spectrum of each doped MOF. Based on our diffuse reflectance

spectra, it appears that the dopant metal has an obvious effect on the nature of the LCCT transition. In all metals, the solid-state UV/VIS spectrum reveals an appearance of a low energy shoulder due to the presence of the heterometal. However, to unravel the nature of the underlying transitions in the broad absorption envelop, future pump-probe optical and x-ray studies are needed

4.5 References

1. Etacheri, V.; Di Valentin, C.; Schneider, J.; Bahnemann, D.; Pillai, S. C., Visible-light activation of TiO₂ photocatalysts: Advances in theory and experiments. *Journal of Photochemistry and Photobiology C: Photochemistry Reviews* **2015**, 25, 1-29.
2. D'Alessandro, D. M., Exploiting redox activity in metal–organic frameworks: concepts, trends and perspectives. *Chem Comm* **2016**, 52 (58), 8957-8971.
3. Calbo, J.; Golomb, M. J.; Walsh, A., Redox-active metal–organic frameworks for energy conversion and storage. *J. Mat. Chem. A* **2019**, 7 (28), 16571-16597.
4. Fujishima, A.; Honda, K., Electrochemical photolysis of water at a semiconductor electrode. *Nature (London)* **1972**, 238 (5358), 37-8.
5. Dong, H.; Zeng, G.; Tang, L.; Fan, C.; Zhang, C.; He, X.; He, Y., An overview on limitations of TiO₂-based particles for photocatalytic degradation of organic pollutants and the corresponding countermeasures. *Water Research* **2015**, 79, 128-146.
6. Yamashita, H.; Ichihashi, Y.; Takeuchi, M.; Kishiguchi, S.; Anpo, M., Characterization of metal ion-implanted titanium oxide photocatalysts operating under visible light irradiation. *J. Synchrotron Radiat.* **1999**, 6 (3), 451-452.
7. Khakpash, N.; Simchi, A.; Jafari, T., Adsorption and solar light activity of transition-metal doped TiO₂ nanoparticles as semiconductor photocatalyst. *Journal of Materials Science: Materials in Electronics* **2012**, 23 (3), 659-667.
8. Roy, N.; Sohn, Y.; Leung, K. T.; Pradhan, D., Engineered Electronic States of Transition Metal Doped TiO₂ Nanocrystals for Low Overpotential Oxygen Evolution Reaction. *The Journal of Physical Chemistry C* **2014**, 118 (51), 29499-29506.
9. Wang, C.; Chen, Z.; Jin, H.; Cao, C.; Li, J.; Mi, Z., Enhancing visible-light photoelectrochemical water splitting through transition-metal doped TiO₂ nanorod arrays. *Journal of Materials Chemistry A* **2014**, 2 (42), 17820-17827.
10. Umebayashia, T. Y., Tetsuya; Itohb, Hisayoshi; Asai, Keisuke, Analysis of electronic structures of 3d transition metal-doped TiO₂ based on band calculations. *Journal of Physics and Chemistry of Solids* **2002**, 63, 1909-1920.
11. Valvekens, P.; Vermoortele, F.; De Vos, D., Metal–organic frameworks as catalysts: the role of metal active sites. *Catalysis Science & Technology* **2013**, 3 (6), 1435-1445.
12. Wang, J.-L.; Wang, C.; Lin, W., Metal–Organic Frameworks for Light Harvesting and Photocatalysis. *ACS Catalysis* **2012**, 2 (12), 2630-2640.
13. Zhu, J.; Li, P.-Z.; Guo, W.; Zhao, Y.; Zou, R., Titanium-based metal-organic frameworks for photocatalytic applications. *Coord. Chem. Rev.* **2018**, 359, 80-101.
14. Dan-Hardi, M.; Serre, C.; Frot, T.; Rozes, L.; Maurin, G.; Sanchez, C.; Férey, G., A New Photoactive Crystalline Highly Porous Titanium(IV) Dicarboxylate. *Journal of the American Chemical Society* **2009**, 131 (31), 10857-10859.
15. Gomes Silva, C.; Luz, I.; Llabrés i Xamena, F. X.; Corma, A.; García, H., Water Stable Zr–Benzenedicarboxylate Metal–Organic Frameworks as Photocatalysts for Hydrogen Generation. *Chemistry – A European Journal* **2010**, 16 (36), 11133-11138.
16. Hendon, C. H.; Tiana, D.; Fontecave, M.; Sanchez, C.; D'arras, L.; Sassoye, C.; Rozes, L.; Mellot-Draznieks, C.; Walsh, A., Engineering the Optical Response of the Titanium-MIL-125 Metal–Organic Framework through Ligand Functionalization. *J. Am. Chem. Soc.* **2013**, 135 (30), 10942-10945.

17. Fu, Y.; Yang, H.; Du, R.; Tu, G.; Xu, C.; Zhang, F.; Fan, M.; Zhu, W., Enhanced photocatalytic CO₂ reduction over Co-doped NH₂-MIL-125(Ti) under visible light. *RSC Advances* **2017**, 7 (68), 42819-42825.
18. Logan, M. W.; Ayad, S.; Adamson, J. D.; Dilbeck, T.; Hanson, K.; Uribe-Romo, F. J., Systematic variation of the optical bandgap in titanium based isorecticular metal-organic frameworks for photocatalytic reduction of CO₂ under blue light. *J. Mat. Chem. A* **2017**, 5 (23), 11854-11863.
19. Ao, D.; Zhang, J.; Liu, H., Visible-light-driven photocatalytic degradation of pollutants over Cu-doped NH₂-MIL-125(Ti). *Journal of Photochemistry and Photobiology A: Chemistry* **2018**, 364, 524-533.
20. Abdelhameed, R. M.; Simões, M. M. Q.; Silva, A. M. S.; Rocha, J., Enhanced Photocatalytic Activity of MIL-125 by Post-Synthetic Modification with CrIII and Ag Nanoparticles. *Chem. Eur. J.* **2015**, 21 (31), 11072-11081.
21. Syzgantseva, M. A.; Ireland, C. P.; Ebrahim, F. M.; Smit, B.; Syzgantseva, O. A., Metal Substitution as the Method of Modifying Electronic Structure of Metal-Organic Frameworks. *Journal of the American Chemical Society* **2019**, 141 (15), 6271-6278.
22. Abednatanzi, S.; Gohari Derakhshandeh, P.; Depauw, H.; Coudert, F. X.; Vrielinck, H.; Van Der Voort, P.; Leus, K., Mixed-metal metal-organic frameworks. *Chem Soc Rev* **2019**, 48 (9), 2535-2565.
23. Castillo-Blas, C.; Gándara, F., Metal-organic Frameworks Incorporating Multiple Metal Elements. *Israel Journal of Chemistry* **2018**, 58 (9-10), 1036-1043.
24. Masoomi, M. Y.; Morsali, A.; Dhakshinamoorthy, A.; Garcia, H., Mixed-Metal MOFs: Unique Opportunities in Metal-Organic Framework (MOF) Functionality and Design. *Angew Chem Int Ed Engl* **2019**, 58 (43), 15188-15205.
25. Dimitrov, V.; Sakka, S., Electronic oxide polarizability and optical basicity of simple oxides. I. *Journal of Applied Physics* **1996**, 79 (3), 1736-1740.
26. Shannon, R. D., Revised effective ionic radii and systematic studies of interatomic distances in halides and chalcogenides. *Acta Crystallographica Section A* **1976**, 32 (5), 751-767.
27. Farges, F.; Brown, G. E.; Rehr, J. J., Ti K-edge XANES studies of Ti coordination and disorder in oxide compounds: Comparison between theory and experiment. *Physical Review B* **1997**, 56 (4), 1809-1819.
28. Ravel, B.; Newville, M., ATHENA, ARTEMIS, HEPHAESTUS: Data Analysis for X-ray Absorption Spectroscopy Using IFEFFIT. *Journal of Synchrotron Radiation* **2005**, 12 (4), 537-541.
29. Unwiset, P.; Makdee, A.; Chanapattarapol, K. C.; Kidkhunthod, P., Effect of Cu addition on TiO₂ surface properties and photocatalytic performance: X-ray Absorption Spectroscopy analysis. *Journal of Physics and Chemistry of Solids* **2018**, 120, 231-240.
30. Gao, Y.; Xie, K.; Wang, W.; Mi, S.; Liu, N.; Pan, G.; Huang, W., Structural features and catalytic performance in CO preferential oxidation of CuO-CeO₂ supported on multi-walled carbon nanotubes. *Catalysis Science & Technology* **2015**, 5 (3), 1568-1579.
31. Yang, D.; An, Y.; Wang, S.; Wu, Z.; Liu, J., Evidence of the oxygen vacancies-induced room-temperature ferromagnetism in the (In_{0.97}-xFe_xSn_{0.03})₂O₃ films. *RSC Advances* **2014**, 4 (64), 33680-33686.

32. Chalmin, E.; Farges, F.; Brown, G. E., A pre-edge analysis of Mn K-edge XANES spectra to help determine the speciation of manganese in minerals and glasses. *Contributions to Mineralogy and Petrology* **2009**, *157* (1), 111-126.
33. Benzi, F.; Giuli, G.; Della Longa, S.; Paris, E., Vanadium K-edge XANES in vanadium-bearing model compounds: a full multiple scattering study. *J Synchrotron Radiat* **2016**, *23* (Pt 4), 947-952.
34. Wong, J.; Lytle, F. W.; Messmer, R. P.; Maylotte, D. H., K-edge absorption spectra of selected vanadium compounds. *Physical Review B* **1984**, *30* (10), 5596-5610.
35. Rees, J. A.; Wandzilak, A.; Maganas, D.; Wurster, N. I. C.; Hugenbruch, S.; Kowalska, J. K.; Pollock, C. J.; Lima, F. A.; Finkelstein, K. D.; DeBeer, S., Experimental and theoretical correlations between vanadium K-edge X-ray absorption and K β emission spectra. *JBIC Journal of Biological Inorganic Chemistry* **2016**, *21* (5), 793-805.
36. Nomura, K., Solution X-Ray Absorption Spectroscopy (XAS) for Analysis of Catalytically Active Species in Reactions with Ethylene by Homogeneous (Imido)vanadium(V) Complexes—Al Cocatalyst Systems. *Catalysts* **2019**, *9* (12).
37. Tanwar, K. S.; Petitto, S. C.; Ghose, S. K.; Eng, P. J.; Trainor, T. P., Fe(II) adsorption on hematite (0001). *Geochimica et Cosmochimica Acta* **2009**, *73* (15), 4346-4365.
38. Naicker, P. K.; Cummings, P. T.; Zhang, H.; Banfield, J. F., Characterization of Titanium Dioxide Nanoparticles Using Molecular Dynamics Simulations. *The Journal of Physical Chemistry B* **2005**, *109* (32), 15243-15249.
39. Nasalevich, M. A.; Hendon, C. H.; Santaclara, J. G.; Svane, K.; van der Linden, B.; Veber, S. L.; Fedin, M. V.; Houtepen, A. J.; van der Veen, M. A.; Kapteijn, F.; Walsh, A.; Gascon, J., Electronic origins of photocatalytic activity in d0 metal organic frameworks. *Sci Rep* **2016**, *6*, 23676.
40. Sun, D.; Ye, L.; Li, Z., Visible-light-assisted aerobic photocatalytic oxidation of amines to imines over NH₂-MIL-125(Ti). *Applied Catalysis B: Environmental* **2015**, *164*, 428-432.

Chapter 5: Direct evidence for heterometal incorporation and its participation in the photoinduced charge separated excited state of MIL125-NH₂

5.1 Introduction

Hybrid materials, such as metal-organic frameworks (MOFs), offer new opportunities as photocatalysts through their rich chemical and structural diversity that allows incorporating accessible catalytic sites and tailoring optoelectronic properties. MOFs are porous solid state networks composed of self-assembled metal ions or clusters connected through coordination bonds with organic or organometallic linkers.¹⁻⁵ Photocatalytic behavior in MOFs can be promoted through inclusion of transition metal centers with multiple stable oxidation states and linker sites that can accommodate stable radical entities in the excited state. MIL-125 is a titanium-based MOF, containing octameric Ti-oxo clusters connected in three dimensions by terephthalate linkers.⁶ Reversible Ti⁴⁺/Ti³⁺ redox conversion at the metal node sites within the framework is accessible through photoinduced linker-to-cluster charge transfer (LCCT).⁶⁻⁷ This redox event has been explored for reactions such as photocatalytic reduction of carbon dioxide, although UV-wavelength light irradiation is required to access the LCCT transition. Consequently, it is also desirable to tune the photoredox properties and extend the range of usable absorption wavelengths further into the visible region without simultaneously introducing high rates of photogenerated charge recombination. Typically, modification of the linker or the metal node can offer greater visible light absorption. Functionalization of the linker, such as been reported for UiO-66, showed that upon amination of the terephthalic acid (1,4-benzenedicarboxylic acid) linker, caused a bathochromic shift in the absorption spectrum⁸. This method of linker functionalization has been applied to MIL-125, extending the LCCT absorption band to just over 550 nm⁹. As a result, the newly

functionalized framework has been promising for many photocatalytic applications such as CO₂ reduction⁹ and oxidation of amines¹⁰. More recent investigation has continued to reduce the fast electron-hole recombination rate that is detrimental to photocatalytic efficiency. Borrowing from the heteroatom doping strategies used in traditional inorganic semiconductors like TiO₂¹¹⁻¹⁴, analogous modifications of MIL-125(Ti) and other Ti-based MOFs have been explored for this purpose¹⁵⁻¹⁹ through direct metal site incorporation/substitution. One of the first reports of this type of modification was Cu-incorporated MIL-125NH₂(Ti) frameworks with up to 5% loading through direct synthesis. This recent report found enhanced photocatalytic activity for CO₂ reduction in the Cu-loaded framework compared to the parent MIL-125NH₂(Ti) catalyst.^{16, 18}

Despite these promising first steps, the local coordination of the doped transition metal and their participation in the photoinduced charge separated excited state is not well understood. A theoretical investigation of metal doping in MIL-125-NH₂ and UiO-66-NH₂ examined the effect on the highest occupied crystal orbital (HOCO) and lowest unoccupied crystal orbital (LUCO) energy gap upon substituting different d⁰ metals into the metal-oxo core. Experimental and theoretical treatment found a red shift of the LCCT state upon addition of the dopant metals with acceptor orbitals below the LUCO of the parent framework, resulting in electron localization onto the heterometal²⁰.

In Chapter 4, a series of 3d transition metal dopants were introduced into MIL-125-NH₂(Ti) and the incorporation was evaluated using a variety of characterization techniques. This chapter explores in more detail the Fe-doped version, MIL-125-NH₂(Ti,Fe), as one of the doped MOF series where substitution of one Ti(IV) center per octameric cluster with Fe(III) was most evident. Previous reports have found that incorporation of Fe into

TiO₂ increases photoactivity by lowering the conduction band, and creating trap states that delays charge recombination²¹. Here, we explore the analogous Fe doping in MIL-125-NH₂, specifically the role of a directly incorporated octahedrally coordinated, d⁵ high spin Fe center on the MOF LCCT state, electronic structure, and dynamics. Based on the theoretical approach of Syzgantseva et. al, the relative energy levels of the dopant metal with respect to the parent MOF can be approximated by referring to the HOCO-LUCO positions of the corresponding metal oxide²⁰. Fe₂O₃ has a band gap of 2.20 eV and an electronegativity of 5.88 eV²², therefore, the high reducibility of Fe₂O₃, small band gap, and lower energy of the LUCO with respect to MIL-125-NH₂(Ti) should provide an electron sink for extending the charge recombination lifetime compared to that found in the parent MOF. Based on this hypothesis, we expected that upon population of the LUCO of MIL-125-NH₂, the photo-excited electron would localize onto the d⁵ Fe(III) site, generating a transient Fe²⁺ species.

Both steady state and time-resolved XAS are ideally suited for investigation of the Fe site coordination and electronic structure dynamics upon MOF LCCT state population. X-ray transient absorption (XTA) spectroscopy is a synchrotron-based pump-probe method requiring a laser-pump and an X-ray probe. Measurements can track structural and oxidation state changes induced by laser excitation, tuned to induce a specific electronic transition. Because of the element specificity, XTA has become an important tool for investigating the photochemistry of both molecular²³⁻³³ and solid-state³⁴⁻³⁷ metal-based systems, including the study on MIL-100, as shown in Chapter 3 of this thesis³⁸. Here Fe K-edge XTA is an important tool in investigating the nature of the LCCT which evades definitive assignment using more conventional methods such as optical transient

absorption (OTA) spectroscopy, which is used here as a supplemental method to characterize the dynamics of this electron transfer process.

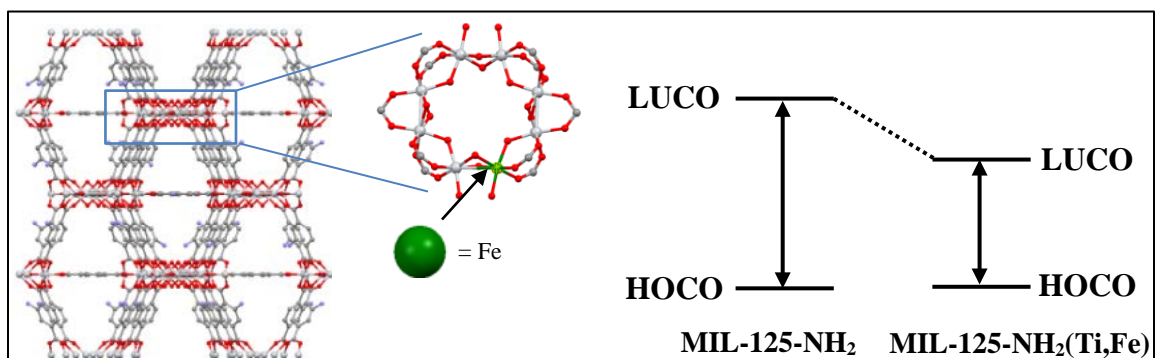


Figure 5.1 Left: Structure of MIL-125-NH₂, highlighting the octameric core containing the Fe(III) dopant. Right: Energy level diagram, representing the reduction in HOCO-LUCO gap after introduction of Fe center to the core.

5.2 Experimental Methods

5.2.1 Synthesis and Materials

5.2.1.1 Materials

Dry methanol, dry dimethylformamide (DMF), and anhydrous iron (III) chloride dissolved in dried solvents, were further dried over molecular sieves prior to use. Titanium (IV) tert-butoxide (Ti(OC₄H₉)₄), 2-aminoterephthalic acid (NH₂-BDC), and cetyltrimethylammoniumbromide, (CTMAB) were used without further purification.

5.2.1.2 Synthesis

MIL-125-NH₂(Ti) was synthesized according to literature precedent with a slight modification¹⁸. 0.26 mL of Ti(OC₄H₉)₄ was measured into a Schlenk flask in a glove box.

To the Schlenk flask, outside the glove box, 0.504 g of NH₂-BDC, 12.1 mL DMF and 1.4 mL methanol were added to the Schlenk flask under the flow of N₂. The solution was sonicated for 30 minutes and then a spatula tip full of CTMAB was added. The reaction mixture was then transferred to a Teflon-lined autoclave and heated to 150°C for 24 hours. The MOF was then centrifuged and resuspended with DMF and methanol 3 times. The supernatant was decanted after each washing.

MIL-125-NH₂(Ti,Fe) was synthesized using a similar procedure to the parent all Ti(IV) MOF, however, anhydrous iron (III) chloride was combined with the linker and the solvents. Similarly, 0.26 mL of Ti(OC₄H₉)₄ was measured into a Schlenk flask in a glove box. To the Schlenk flask, outside the glove box, a stoichiometric amount of anhydrous FeCl₃ dissolved in 12.1 mL DMF and 1.4 mL methanol was added, as well as, 0.504 g of NH₂-BDC, were added to under the flow of N₂. The solution was sonicated for 30 minutes and then a spatula tip full of CTMAB was added. The reaction mixture was then transferred to a Teflon-lined autoclave and heated to 150°C for 24 hours. The MOF was then centrifuged and resuspended with DMF and methanol 3 times. The supernatant was decanted after each washing.

5.2.2 Characterization

Powder XRD patterns were recorded using a Bruker D8 ADVANCE ECO Diffractometer. Steady-state electronic absorption spectra were collected using a Cary Varian UV–visible–near-infrared (NIR) spectrophotometer. Solid-state powder samples were ground thoroughly and measured undiluted using a diffuse reflectance (DR) accessory (Harrick Scientific). Solution and liquid samples were measured in a 2mm cuvette.

Samples were suspended in DMF and centrifuged at 2.5 krpm for 20 minutes. This washing procedure was repeated 4 times to ensure removal of residual linker was left.

5.2.3 Optical Transient Absorption Spectroscopy

Optical transient absorption spectra were measured using Light Conversion Inc. ultrafast spectroscopy system. The system consists of a *Harpia* pump-probe spectrometer, an adjustable repetition rate “one box” *Pharos-SP* laser with Yb:KGW pumped design and an Orpheus-F hybrid optical parametric amplifier used to generate the pump pulse and also the probe pulse through white light continuum generation from the idler.

Measurements were conducted using a 400 nm pump pulse wavelength and white light probe at 10 kHz repetition rate. Liquid samples were prepared by suspending 250 mg of MOF in dimethylformamide (DMF) and centrifuging at 2.5 krpm for 20 minutes. The supernatant containing the smallest suspended MOF nanoparticles was measured in a 2mm cuvette with concentration adjusted to achieve optical density of ~0.3-0.5. The UV/VIS of the suspensions were measured before and after OTA measurements.

5.2.4 Steady State X-Ray Absorption Spectroscopy

X-ray absorption data were collected at the Fe K-edge (7112 eV) at Beamline 8-ID (ISS) at the National Synchrotron Light Source II at Brookhaven National Laboratory using a damping wiggler source and Si(111) double crystal monochromator. The monochromatic beam spot size was 1 mm. A Fe metal foil was used as the reference for energy calibration. Powder MOF sample was measured undiluted in fluorescence mode using a PIPS detector with Mn Z-1 filtering. All data were collected at room temperature. Thirty continuous-scan spectra were collected, each with 1 min. total acquisition time, and averaged. No more

than 10 scans were collected on one spot to minimize x-ray damage. Negligible X-ray damage was observed with sequential scans within 10 scans per spot.

EXAFS data were processed and analyzed using the Demeter program package.³⁹ Fourier Transform spectra were obtained using k^2 weighting and a $\chi(k)$ range from 2.5 to 11 \AA^{-1} . Fitting was performed in R space over the range of 1 to 3.8 \AA using a fitting model derived from the reported crystal structure for MIL-125-NH₂⁴⁰ with 1 Ti site substituted with Fe. Theoretical scattering paths derived from this model and associated EXAFS fitting parameters are summarized in Table 5.1 along with the best fit values.

5.2.5 X-Ray Transient Absorption Spectroscopy

The X-ray transient absorption (XTA) measurements were performed at 11-ID-D, Advanced Photon Source (APS), at Argonne National Lab. The laser pump source was the second-harmonic output of a fs Ti:Sapphire regenerative amplified laser: 400 nm, 100 fs full width-half-maximum (fwhm) and 10 kHz repetition rate. The X-ray was Hybrid Fill RHB (Singlet) mode, where an intense X-ray pulse with 16% of the total average photon flux was separated in time from other weak X-ray pulses. The intense X-ray pulse with 118 ps fwhm and 271.5 kHz repetition rate was used as the probe.

Samples were prepared in acetonitrile. 250 mg of sample was suspended in acetonitrile and sonicated for 30 minutes. Samples were left undisturbed for at least 2 hours to allow unsuspended larger particles to settle and the supernatant was used for measurement. To minimize photodamage, the suspended sample was purged with acetonitrile-saturated nitrogen and circulated in a closed-loop jet flow assembly during data collection. The complete experimental setup has been described elsewhere⁴¹. In brief, the laser pump and

X-ray probe beams were spatially and temporally overlapped at the 600 μm diameter sample stream. The laser fluence used in the measurements is $\sim 40 \mu\text{J}/\text{mm}^2$. The X-ray fluorescence signal was detected by two avalanche photodiodes (APDs) positioned at 90° angle on both sides of the incident X-ray beam. A third APD detector, collecting upstream X-ray scattering, was used for the normalization. A Z-1 (Mn) filter/soller slit filter combination, which was custom-designed for the specific sample chamber configuration and the distance between the sample and the detector, was inserted between the sample fluid jet and the APD detectors to reduce the scattering background. Twenty-eight X-ray absorption spectra were collected and averaged at 100 ps (nominal time zero) delay time between the laser pulse and synchronized X-ray bunch. Spectra obtained using several X-ray bunches prior to the synchronized bunch were used to generate an average “pre-time zero” XTA spectrum. Spectra were also collected in the absence of laser light for comparison. Time scans were collected by monitoring the signal at 7.123 keV as a function of delay time ranging from -0.2 ns to 36 ns between the laser pulse and synchronized x-ray bunch. The XTA signal derived from the next two subsequent x-ray bunches separated by 3.68 microseconds from one another, were collected simultaneously, as well.

5.3 Results and Discussion

5.3.1 Synthesis and Characterization

The MIL-125-NH₂(Ti) and MIL-125-NH₂(Ti,Fe) frameworks were synthesized with modification to literature precedent¹⁸. In both syntheses, CTMAB was added as a surfactant to promote MOF nanoparticles formation and suspension. This method of surfactant-assisted nanoparticle synthesis has been previously reported for MIL-125-NH₂(Ti)⁴². For our studies, it was necessary to have a stable colloidal suspension so that

the sample was compatible with the flow jet assembly used for the XTA experiments. Additionally, the small particle size reduced the amount of light scattering in the optical measurements. The crystallinity of both nanoparticle MOF samples was verified using powder X-ray diffraction (PXRD), shown in Figure 5.2.

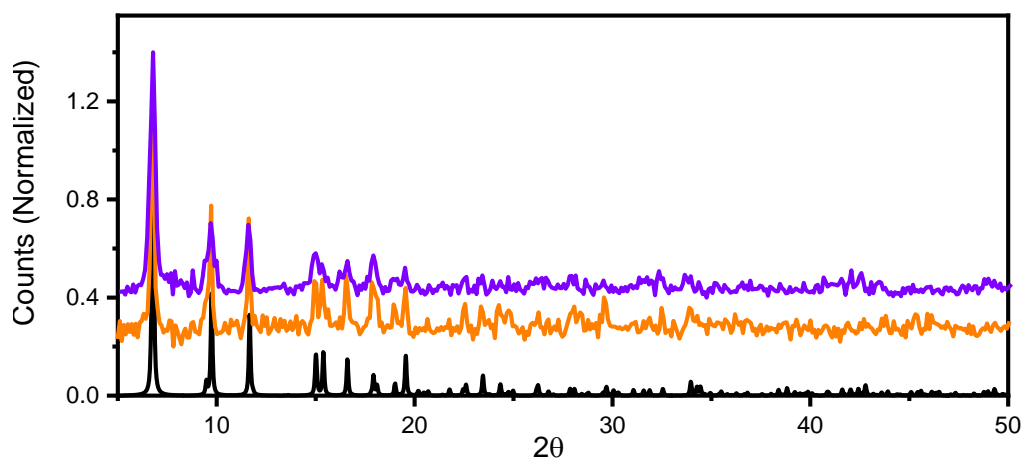


Figure 5.2 PXRD of MIL-125 simulated⁴³ (black), MIL-125-NH₂(Ti) (orange), MIL-125-NH₂(Ti,Fe) (purple)

5.3.2 Optical Electronic Absorption Spectroscopy

The optical electronic absorption spectra for the MOF materials were obtained through transmission absorption measurements of the colloidal nanoparticle suspensions and diffuse reflectance (DR) measurements of the solid-state powders. The transmission spectra for the NH₂-BDC linker, MIL-125-NH₂(Ti) and MIL-125-NH₂(Ti,Fe) framework suspensions in DMF are shown in Figure 5.3. The MOFs and linker all display an absorption spectrum exhibiting a feature in the near UV with a maximum between 350 and 400 nm. This main feature is attributed to a $n \rightarrow \pi^*$ transition localized on the aminated

linker. For the MOF systems, this band extends into the visible region and gains LCCT character upon linker incorporation with the metal-oxo clusters, as previously reported⁴⁴. The colloidal suspensions of both MOF samples produce scattering backgrounds, in their UV/VIS spectra that differ depending on the variations in particle size. Differences in scattering background may obscure low intensity features and make comparison of the electronic transitions in this wavelength region difficult. Therefore, we turned to UV/VIS diffuse reflectance spectra which have more consistent scattering background, to evaluate these valence transitions. As shown in Figure 5.4, the same dominant features are present as shown in the transmission UV/VIS spectra, however, a shoulder in the visible region is clearly absent from the linker spectrum and more pronounced in the Fe-doped MIL-125-NH₂ system; the appearance of this red shifted feature may indicate transitions involving lower energy “trap” states due to introduction of the Fe heterometal sites.

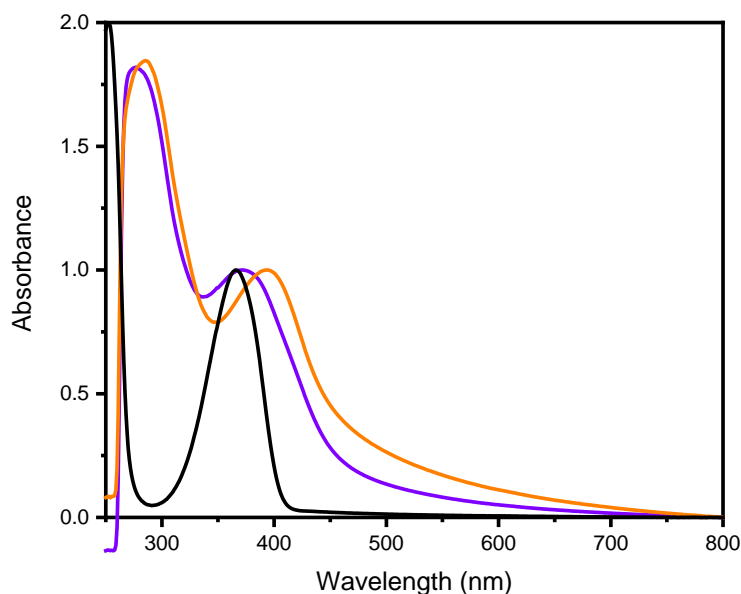


Figure 5.3 UV/VIS Spectra of MIL-125-NH₂ (Ti) (orange) and MIL-125-NH₂ (Ti,Fe) (purple) suspended in DMF and 2-aminoterephthalic acid in CH₃CN (black)

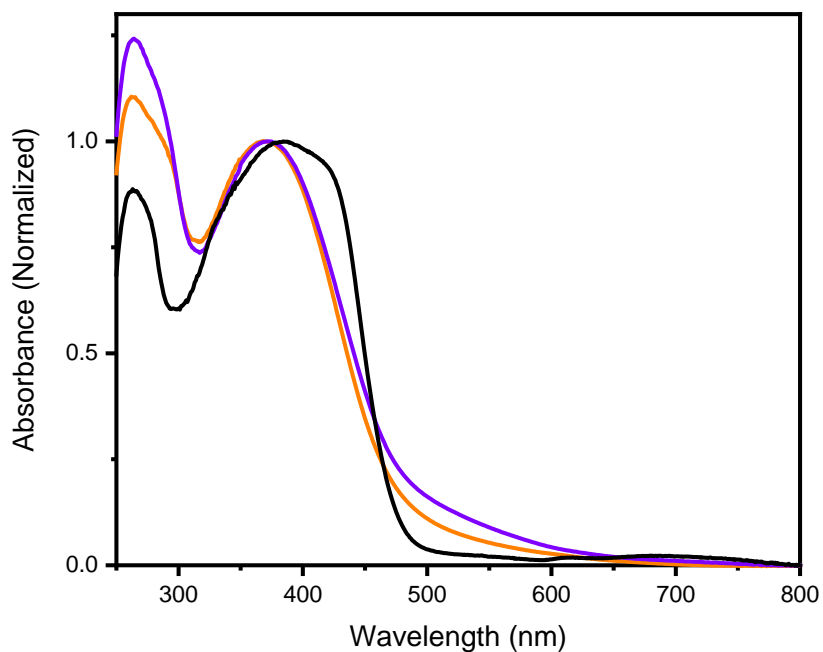


Figure 5.4 Diffuse reflectance spectra of 2-aminoterephthalic acid (black), MIL-125-NH₂(Ti) (orange) and MIL-125-NH₂(Ti,Fe) (purple)

5.3.3 Steady State X-ray Absorption Spectroscopy

To better understand how the iron is incorporated within the framework, steady state X-ray absorption measurements were conducted at the Fe K-edge. Both XANES and EXAFS spectra of MIL-125-NH₂(Ti,Fe) and several Fe references are depicted in Figure 5.5. As previously discussed in Chapter 4 of this thesis, comparison of the XANES edge shift confirms the Fe³⁺ oxidation state of the Fe species in the MIL-125-NH₂(Ti,Fe) while the overall shape indicates a distinct coordination devoid of metallic Fe, Fe₂O₃, or FeCl₃ impurities.

Comparison of the EXAFS spectra reveals that the Fe center in the MOF has a different coordination environment than that of Fe_2O_3 , FeCl_3 , or Fe foil. In the first coordination shell, Fe_2O_3 and the doped MOF have a feature at a similar scattering distance, however this peak has been attributed to the two inequivalent Fe-O scattering paths within the distorted octahedral coordination sphere⁴⁵. Because we expect Fe in the doped MOF to have a comparable coordination environment, this similarity was expected. Furthermore, the absence of Fe-Fe or Fe-Cl peaks⁴⁵⁻⁴⁶ at longer scattering distances indicates that the MIL-125- $\text{NH}_2(\text{Ti},\text{Fe})$ does not involve these types of Fe speciation or impurities.

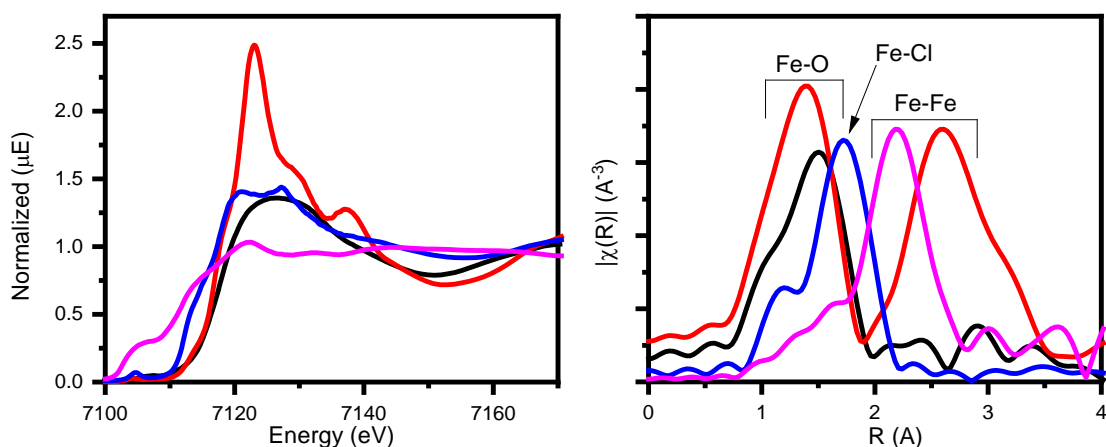


Figure 5.5 Left: Experimental Fe K-Edge XAS and Right: EXAFS plotted in R space of MIL-125- $\text{NH}_2(\text{Ti},\text{Fe})$ (black), Fe_2O_3 (red), FeCl_3 (blue), and Fe foil (pink).

Quantitative coordination information is provided by EXAFS fittings of MIL-125- $\text{NH}_2(\text{Ti},\text{Fe})$ spectrum in R space, as shown in Figure 5.5. along with a summary of the results listed in Table 5.1. Experimentally obtained EXAFS data were fit using a model derived from the reported crystal structure of MIL-125- $\text{NH}_2(\text{Ti})$ with one titanium site substituted by iron as depicted in Figure 5.6. In this fit, all scattering path degeneracies

were fixed according to this model. Mild restraints were applied to the variable parameters to ensure physically meaningful values were obtained.

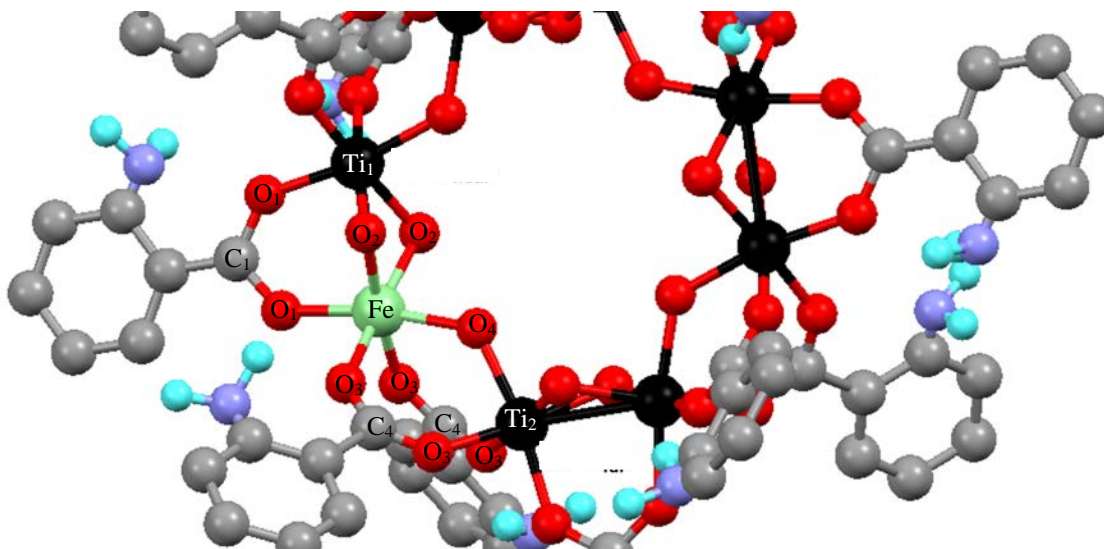


Figure 5.6 Local coordination environment of MIL-NH₂(Ti,Fe)

The six Fe-O single scattering paths, as defined and illustrated in the figure, were parameterized using a universal expansion/contraction multiplier variable and a single Debye-Waller factor (σ^2) to account for changes in the average first coordination sphere bond length and disorder during the fit. The two carbon single scattering paths (Fe-C₁ and Fe-C₄) were treated similarly to the oxygen paths, assigning one σ^2 and one expansion/contraction variable to both paths. The two single scattering paths involving the adjacent Ti sites (Ti₁ and Ti₂ in the model) as well as two distal oxygen scatterers (O1_2) and (O3_2) were each parameterized using separate distance and σ^2 variables. Four multiple scattering paths were included in the fit as defined in Table 5.1 and Figure 5.7, Using the assumption that the C-O distance of the carboxylate moiety is fixed and defined by the crystal structure, the multiple scattering paths were varied using

expansion/contraction terms based on the triangular scattering geometry involved and therefore only the variables associated with the corresponding Fe-O and Fe-C single scattering path distances.

This EXAFS fit is consistent with iron coordinated in a distorted octahedral environment, like that of the Ti sites in the parent MIL-125-NH₂(Ti) structure. The fit also includes contributions from scattering paths beyond the first shell including neighboring Ti sites. The main structural deviation of the fit from the starting point of the model is that the first shell Fe-O bond lengths are longer than those of the Ti sites found in the parent MOF. The longer coordination bond is expected based on the typical range of reported Fe-O bond lengths (1.94–2.12 Å)⁴⁷ compared to Ti-O bond lengths (1.94 Å).⁴⁸ Furthermore, the fit suggests the titanium and carbon paths also change, as a result of iron doping. The expanded Fe-O coordination shell is compensated by the contraction of the longer Fe-Ti (Ti_{far}) scattering path. Together with the XRD results, which show analogous single phase structure for the MIL-125-NH₂(Ti,Fe) and MIL-125-NH₂, this reasonable fit to the experimental MIL-125-NH₂(Ti,Fe) EXAFS spectrum using the modified MIL-125-NH₂(Ti) structure beyond just the first coordination shell, provides strong evidence that Fe is indeed incorporating into the octameric ring, substituting one of the Ti sites.

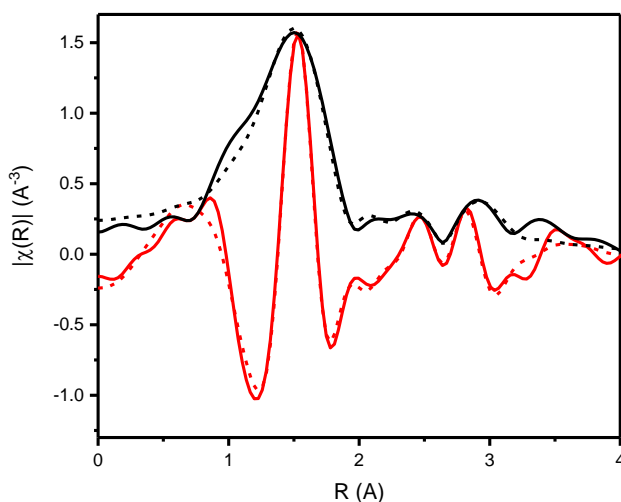


Figure 5.7 MIL-125-NH₂(Ti,Fe) EXAFS (solid) and corresponding EXAFS fit (dotted) with both magnitude (black) and real (red) spectrum shown.

Table 5.1 EXAFS Fitting Parameters and comparison with crystallographic data for MIL-125-NH₂(Ti,Fe)

Path	CN	R _{cryst} (Å) ^a	R _{fit} (Å)	Δ (Å)	σ ²
Fe-O ₃	2	1.89(9)	1.94(6) ± 0.017(2)	0.04(7) ± 0.017(2)	0.006 ± 0.001
Fe-O ₁	1	1.94(6)	1.99(4) ± 0.017(6)	0.04(8) ± 0.017(6)	0.006 ± 0.001
Fe-O ₂	2	1.98(7)	2.03(7) ± 0.018(0)	0.05(9) ± 0.018(0)	0.006 ± 0.001
Fe-O ₄	1	1.98(7)	2.03(7) ± 0.018(0)	0.05(0) ± 0.018(0)	0.006 ± 0.001
Fe-Ti	1	2.76(8)	2.93(8) ± 0.07(4)	0.17(0) ± 0.07(4)	0.005 ± 0.011
Fe-Ti ₂	1	3.55(2)	3.35(4) ± 0.01(7)	0.19(8) ± 0.01(7)	0.005 ± 0.012
Fe-C ₁	1	2.87(6)	3.03(5) ± 0.23(2)	0.15(9) ± 0.23(2)	0.003 ± 0.002
Fe-C ₄	1	3.00(1)	3.16(7) ± 0.24(2)	0.16(6) ± 0.24(2)	0.003 ± 0.002
Fe-O _{1_2}	1	3.12(9)	2.96(2) ± 0.28(0)	0.16(7) ± 0.28(0)	0.005 ± 0.000
Fe-O _{3_2}	2	3.35(9)	3.54(5) ± 0.16(9)	0.18(6) ± 0.16(9)	0.005 ± 0.000
Fe-O ₃ O ₂	4	3.88(5)	3.93(4) ± 0.00(0)	0.04(9) ± 0.00(0)	0.008 ± 0.002
Fe-O ₁ O ₄	2	3.92(7)	3.97(6) ± 0.00(0)	0.04(9) ± 0.00(0)	0.008 ± 0.002
Fe-C ₄ O ₃	4	2.98(4)	3.08(7) ± 0.00(0)	0.10(3) ± 0.00(0)	0.008 ± 0.002
Fe- C ₁ O ₁	2	3.13(0)	3.23(8) ± 0.00(0)	0.10(8) ± 0.00(0)	0.008 ± 0.002

^a Distances obtained from crystal structure of MIL125-NH₂(Ti) reported in ref 40, $S\sigma^2=1.00$ and E^0 was 1.7272 eV for all paths
 $R= 0.003$

5.3.4 Femtosecond Optical Transient Absorption Spectroscopy

Ultrafast TA data for MIL-125-NH₂(Ti) MIL-125-NH₂(Ti,Fe), and the NH₂-BDC linker are shown in Figure 5.8. The spectra of the linker exhibits a transient absorption band that appears within the instrument response time, at $\lambda_{\text{max}}=585$ nm and subsists well beyond the experimentally available delay range with more than 80% of the signal remaining at the end of collection after 1 ns delay time. This transient absorption band can be assigned to the hole on the amine upon photo excitation of the $n \rightarrow \pi^*$ transition. The early time spectra of MIL-125-NH₂(Ti,Fe) show a similar transient absorption feature that overlaps with an additional broad and unstructured TA band throughout the visible that extends into the NIR wavelength range. The all-Ti version of this MOF, MIL-125-NH₂(Ti) exhibits TA spectra that are dominated by this broad redshifted band. As discussed below, the TA kinetics for both MOFs have faster components that dominate the decay that are not observed for the linker itself. Spectroelectrochemical studies were conducted on aminoterephthalate dimethyl ester and Ti₈O₈[OOC(CH₃)₃]₁₆ molecular clusters, to identify the spectral signatures of the linker cation and reduced titanium-oxo cluster. The authors reported that an absorption feature, with $\lambda_{\text{max}}=530$ nm, is assigned to formation of the aminoterephthalatic radical cation. Additionally, they noted that the transient absorption feature would be red shifted, based on the overlap of this feature with the ground state bleach of the aminoterephthalate dimethyl ester. Furthermore, the spectra collected for the electrochemically generated radical anion of the Ti-oxo cluster showed a broad absorption band extending throughout the visible and IR range. In this study, which also focused on the excited state dynamics of MIL-125-NH₂(Ti), the TA data for the MOF was reported have nearly identical spectral shape and kinetics, as what we have observed for

the linker alone. In comparing our finding with this previous report, we believe the authors may have been observing loose linker contamination within their sample, which was responsible for the observed spectral shape and decay that they attributed to the MOF. Notably, the authors did not report the OTA data for the linker alone for comparison. In our work, we speculate that the feature around 585 nm in the spectrum of the Fe-doped MOF, that is mostly absent in the parent MOF may indicate a more localized hole on the linker associated with a charge separated state.

The kinetic traces obtained by monitoring TA signal at 585 nm are shown in Figure 5.8 along with fits to these decay signals. The multiexponential fitting results are summarized in Table 5.2. Comparing these kinetics in this ultrafast range reveals that transient absorption decay of MIL-125-NH₂(Ti) is dominated by shorter sub-200ps lifetime components while the decay of the transient absorption of MIL-125-NH₂(Ti,Fe) has a dominant lifetime component on the order of 3 ns. While the signal appears to have completely decayed for MIL-125-NH₂(Ti) by 1 ns, nearly half of the TA signal remained at this delay time for MIL-125-NH₂(Ti,Fe), indicating even longer lifetime components. The longer lifetimes may be attributed to the Fe dopant serving to delay electron-hole recombination and potentially acting as a “trap” site. However, this assignment of the nature of the LCCT state is not definitive, and further insight, particularly on the role of the Fe trap site, can be provided by element specific, time resolved techniques, such as X-ray transient absorption spectroscopy at the Fe K-edge.

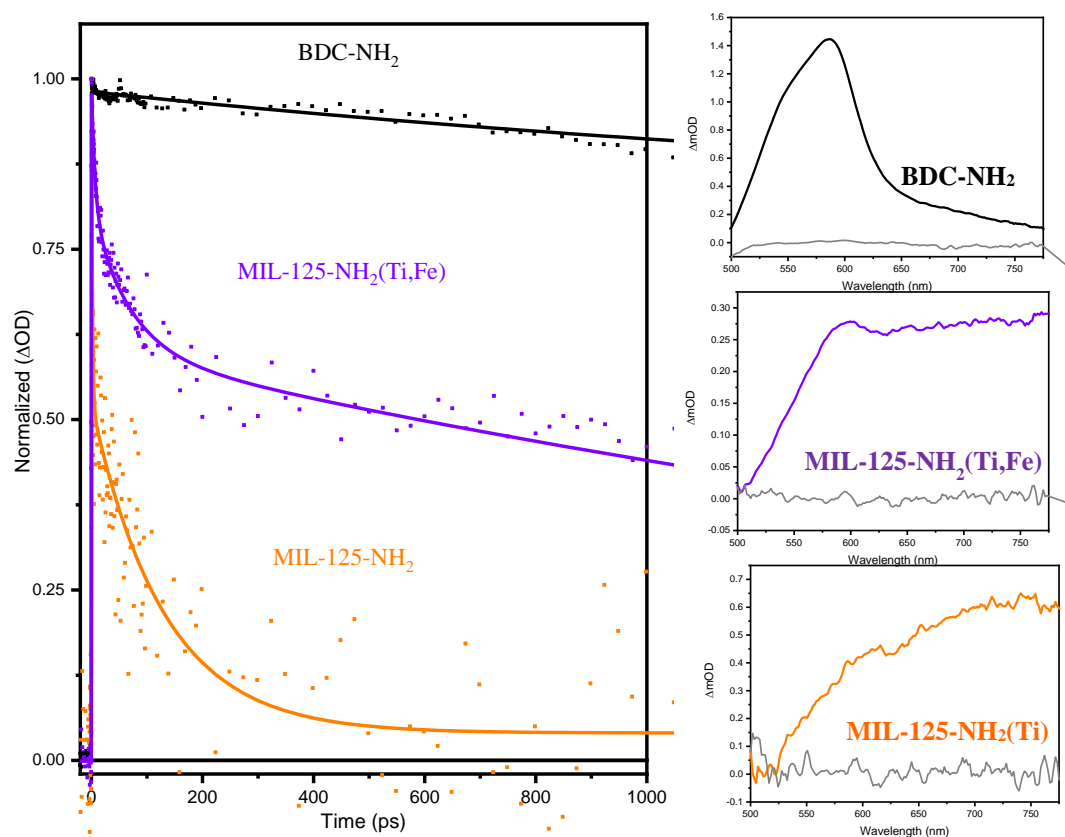


Figure 5.8 Optical transient absorption left: kinetics of the BDC-NH₂ linker (black), MIL-125-NH₂(Ti) (orange), and MIL-125-NH₂(Ti,Fe) (purple) collected at 585 nm and right: the corresponding OTA spectra collected at pre-time zero (gray) and 1 ± 0.5 ps. All samples were measured in DMF solution.

Table 5.2 Fitting Results of Optical Transient Absorption 585 nm kinetics^a

Parameter	2-aminoterephthalic acid	MIL-125-NH ₂	MIL-125-NH ₂ (Ti,Fe)
A1	0.18 ± 0.03	0.49 ± 0.07	0.18 ± 0.02
τ_1	2119 ± 448 ps	2 ± 0.4 ps	7 ± 2 ps
A2	---	0.48 ± 0.02	0.21 ± 0.02
τ_2	---	129 ± 17 ps	67 ± 15 ps
A3	---	---	0.56 ± 0.13
τ_3	----	---	2960 ± 1185 ps
Shelf	0.79 ± 0.03	0.01 ± 0	0.04 ± 0.14

a The IRF was set to 250 fs for all fits

5.3.5 Fe K-edge X-Ray Transient Absorption Spectroscopy

Fe K-edge X-ray transient absorption spectroscopy (XTA) was used to elucidate the nature and dynamics of the LCCT excited state, particularly the role of the Fe dopant, in MIL-125-NH₂(Ti,Fe). Figure 5.9 highlights the changes seen between the XTA spectra collected using the X-ray bunch synchronized with the laser pump pulse and those collected using pre-time zero X-ray bunches, referred to as “laser on” and “laser off” spectra, respectively. An edge shift to lower energy is observed for the “laser on” spectrum that indicates a reduction of the iron site from Fe(III) to Fe(II)⁴⁹. The difference spectra, depicted in the bottom of Figure 5.9, reveals a derivative-like feature emphasizing this transient edge shift to lower energy. These transient changes clearly indicate increased electron density at the iron site, associated with the population of charge-transfer excited state.

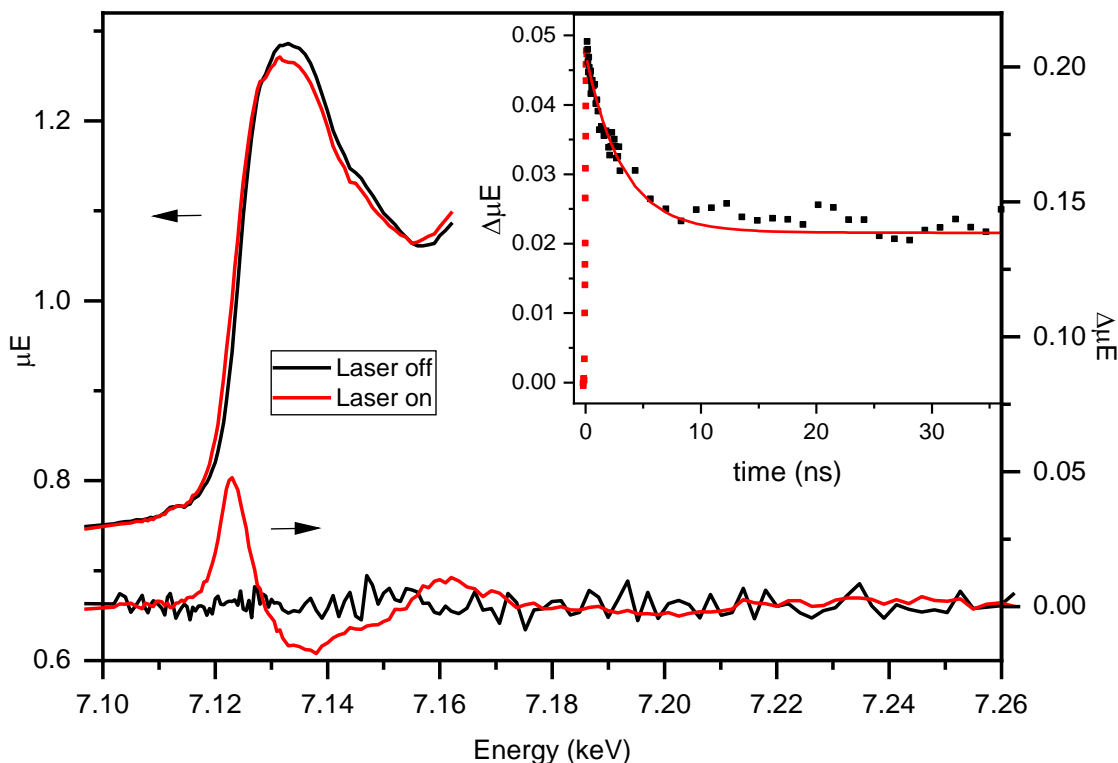


Figure 5.9 “laser on” (red) and “laser off” (black) Fe K-Edge XTA spectra of MIL-125-NH₂(Ti,Fe) . The difference spectra between the “laser off” and “laser on” spectra . The black difference spectra represents the difference generated with the laser blocked. Inset: The kinetics collected 7.123 keV and corresponding fit

Time scans collected by monitoring the XTA difference signal maximum at 7.123 keV produce the kinetic trace, shown in the inset of Figure 5.9. Successive X-ray bunches, after the synchronized bunch were simultaneously collected during these time scans to produce the extended kinetics depicted in Figure 5.10. Fitting these kinetics, as summarized in Table 5.3, reveals a fast component, approximately 2.3 ns, and at least two longer-lived components. The fast component is similar to the long lifetime measured by OTA, confirming the consistency and validity in combining the two methods in probing

these excited state dynamics that appear to be spread over a very large range of lifetimes. While too few data points on the microsecond time scale are available for accurate fitting of the lifetime, the decay trace clearly shows sustained electron reduction of the Fe sites site far beyond 7.3 microseconds. Furthermore, the different lifetime components may be associated with the probability of the electron-hole recombination, depending on the position of the Fe site relative to the linker containing the hole. This exceptionally long lifetime indicates that excitation into the LCCT band of MIL-125-NH₂(Ti,Fe) promotes localization of an electron that remains on the Fe site, preventing charge recombination.

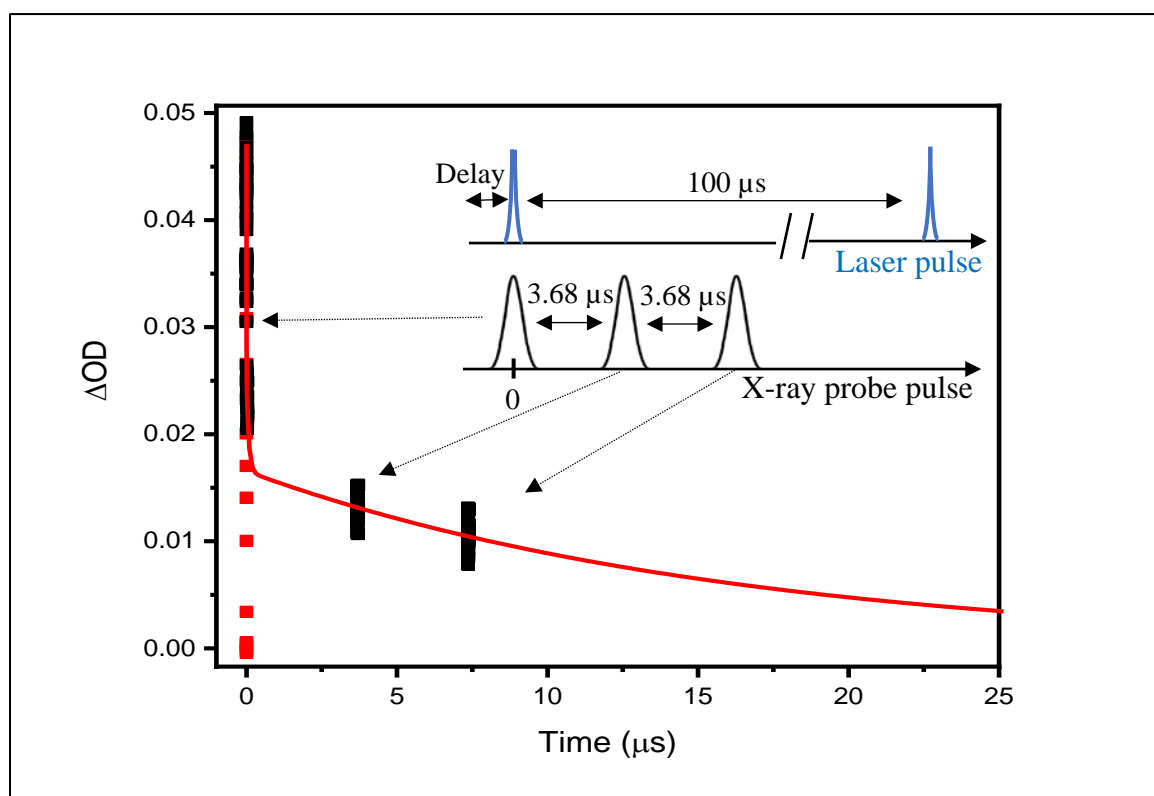


Figure 5.10 Extended XTA Kinetics monitored at 7.123 keV of 1Fe/cluster doped MIL-125-NH₂

Table 5.3 Fitting Parameters for the XTA Kinetics monitored at 7.123 keV for MIL-125-NH₂(Ti,Fe)

Parameter	Value
A1	0.023 ± 0.001
τ_1	2 ± 0.2 ns
A2	0.009 ± 0.001
τ_2	70 ± 20 ns
A3	0.02 ± 0.0004
τ_3	16 ± 1.1 μ s

5.4 Conclusion

In this chapter, a novel Fe-doped Ti-based MOF, MIL-125-NH₂(Ti, Fe) was successfully synthesized and characterized. While previous studies have also claimed to dope MIL-125-NH₂ cluster with a heterometal^{18, 20, 50}, careful analysis of the true coordination and position of the metal site was not formerly completed. In turn, we performed XANES and EXAFS studies, to gain insight on the coordination environment of the heterometal. Fitting of the EXAFS using a modified MIL-125-NH₂ structure confirmed that the coordination environment of the iron center is very similar to that of the Ti sites in the parent framework, with the exception of distortion of the local bonds surrounding the dopant. Given these results, we were able to reasonably conclude that the Fe metal was incorporated into the Ti-oxo ring.

Beyond confirming the location of the Fe dopant into framework, we explored the participation of the Fe center in the LCCT excited state. While MIL-125-NH₂ has been previously reported to undergo a charge transfer event upon visible light irradiation¹⁰, the electronic impact of a dopant on the LCCT state had not been investigated. The UV/VIS diffuse reflectance spectroscopy finding showed that the Fe-doped framework displays enhanced absorption in the visible region compared to the parent MIL-125-NH₂ MOF. To

untangle the nature of the underlying transitions in this broad absorption envelop, OTA studies suggest that the transient species corresponding to the hole on the linker has a longer lifetime in the Fe-doped MOF than that of the parent MIL-125-NH₂(Ti). However, due to the similarity, as well as, the broad and featureless nature of the TA spectrum found for both MOF samples, this excited state eludes definitive assignment. Therefore, we turned to the element specific technique, Fe K-edge XTA spectroscopy to provide evidence of participation of the Fe in the excited state. Transient changes in the XAS spectra indicate electron migration onto the Fe dopant. Monitoring the XTA kinetics confirmed the long-lived nature of the transient reduction. These results confirmed our hypothesis that the Fe dopant's incorporation within the MOF cluster can serve as trap sites to promote long-live charge separated excited states.

5.5 References

1. Furukawa, H.; Cordova, K. E.; O’Keeffe, M.; Yaghi, O. M., The Chemistry and Applications of Metal-Organic Frameworks. *Science* **2013**, *341* (6149), 1230444.
2. Kole, G. K.; Vittal, J. J., Solid-state reactivity and structural transformations involving coordination polymers. *Chemical Society Reviews* **2013**, *42* (4), 1755-1775.
3. Foo, M. L.; Matsuda, R.; Kitagawa, S., Functional Hybrid Porous Coordination Polymers. *Chemistry of Materials* **2014**, *26* (1), 310-322.
4. Wang, C.; Liu, D.; Lin, W., Metal–Organic Frameworks as A Tunable Platform for Designing Functional Molecular Materials. *Journal of the American Chemical Society* **2013**, *135* (36), 13222-13234.
5. Yuan, S.; Feng, L.; Wang, K.; Pang, J.; Bosch, M.; Lollar, C.; Sun, Y.; Qin, J.; Yang, X.; Zhang, P.; Wang, Q.; Zou, L.; Zhang, Y.; Zhang, L.; Fang, Y.; Li, J.; Zhou, H.-C., Stable Metal–Organic Frameworks: Design, Synthesis, and Applications. *Adv Mater* **2018**, *30* (37), 1704303.
6. Dan-Hardi, M.; Serre, C.; Frot, T.; Rozes, L.; Maurin, G.; Sanchez, C.; Férey, G., A New Photoactive Crystalline Highly Porous Titanium(IV) Dicarboxylate. *J. Am. Chem. Soc.* **2009**, *131* (31), 10857-10859.
7. Fu, Y.; Sun, D.; Chen, Y.; Huang, R.; Ding, Z.; Fu, X.; Li, Z., An Amine-Functionalized Titanium Metal–Organic Framework Photocatalyst with Visible-Light-Induced Activity for CO₂ Reduction. *Angewandte Chemie International Edition* **2012**, *51* (14), 3364-3367.
8. Gomes Silva, C.; Luz, I.; Llabrés i Xamena, F. X.; Corma, A.; García, H., Water Stable Zr–Benzenedicarboxylate Metal–Organic Frameworks as Photocatalysts for Hydrogen Generation. *Chemistry – A European Journal* **2010**, *16* (36), 11133-11138.
9. Fu, Y.; Sun, D.; Chen, Y.; Huang, R.; Ding, Z.; Fu, X.; Li, Z., An amine-functionalized titanium metal-organic framework photocatalyst with visible-light-induced activity for CO₂ reduction. *Angew Chem Int Ed Engl* **2012**, *51* (14), 3364-7.
10. Sun, D.; Ye, L.; Li, Z., Visible-light-assisted aerobic photocatalytic oxidation of amines to imines over NH₂-MIL-125(Ti). *Applied Catalysis B: Environmental* **2015**, *164*, 428-432.
11. Cong, Y.; Zhang, J.; Chen, F.; Anpo, M., Synthesis and Characterization of Nitrogen-Doped TiO₂ Nanophotocatalyst with High Visible Light Activity. *The Journal of Physical Chemistry C* **2007**, *111* (19), 6976-6982.
12. Di Paola, A.; García-López, E.; Ikeda, S.; Marci, G.; Ohtani, B.; Palmisano, L., Photocatalytic degradation of organic compounds in aqueous systems by transition metal doped polycrystalline TiO₂. *Catalysis Today* **2002**, *75* (1), 87-93.
13. Inturi, S. N. R.; Boningari, T.; Suidan, M.; Smirniotis, P. G., Visible-light-induced photodegradation of gas phase acetonitrile using aerosol-made transition metal (V, Cr, Fe, Co, Mn, Mo, Ni, Cu, Y, Ce, and Zr) doped TiO₂. *Applied Catalysis B: Environmental* **2014**, *144*, 333-342.
14. Matsumoto, Y.; Murakami, M.; Shono, T.; Hasegawa, T.; Fukumura, T.; Kawasaki, M.; Ahmet, P.; Chikyow, T.; Koshihara, S.-y.; Koinuma, H., Room-Temperature Ferromagnetism in Transparent Transition Metal-Doped Titanium Dioxide. *Science* **2001**, *291* (5505), 854-856.

15. Hendon, C. H.; Tiana, D.; Fontecave, M.; Sanchez, C.; D'arras, L.; Sassoye, C.; Rozes, L.; Mellot-Draznieks, C.; Walsh, A., Engineering the Optical Response of the Titanium-MIL-125 Metal–Organic Framework through Ligand Functionalization. *J. Am. Chem. Soc.* **2013**, *135* (30), 10942-10945.
16. Fu, Y.; Yang, H.; Du, R.; Tu, G.; Xu, C.; Zhang, F.; Fan, M.; Zhu, W., Enhanced photocatalytic CO₂ reduction over Co-doped NH₂-MIL-125(Ti) under visible light. *RSC Advances* **2017**, *7* (68), 42819-42825.
17. Logan, M. W.; Ayad, S.; Adamson, J. D.; Dilbeck, T.; Hanson, K.; Uribe-Romo, F. J., Systematic variation of the optical bandgap in titanium based isorecticular metal–organic frameworks for photocatalytic reduction of CO₂ under blue light. *J. Mat. Chem. A* **2017**, *5* (23), 11854-11863.
18. Ao, D.; Zhang, J.; Liu, H., Visible-light-driven photocatalytic degradation of pollutants over Cu-doped NH₂-MIL-125(Ti). *Journal of Photochemistry and Photobiology A: Chemistry* **2018**, *364*, 524-533.
19. Abdelhameed, R. M.; Simões, M. M. Q.; Silva, A. M. S.; Rocha, J., Enhanced Photocatalytic Activity of MIL-125 by Post-Synthetic Modification with CrIII and Ag Nanoparticles. *Chem. Eur. J.* **2015**, *21* (31), 11072-11081.
20. Syzgantseva, M. A.; Ireland, C. P.; Ebrahim, F. M.; Smit, B.; Syzgantseva, O. A., Metal Substitution as the Method of Modifying Electronic Structure of Metal-Organic Frameworks. *J Am Chem Soc* **2019**, *141* (15), 6271-6278.
21. Umebayashia, T. Y., Tetsuya; Itohb, Hisayoshi; Asai, Keisuke, Analysis of electronic structures of 3d transition metal-doped TiO₂ based on band calculations. *Journal of Physics and Chemistry of Solids* **2002**, *63*, 1909-1920.
22. Xu, Y. S., Martin A.A, The absolute energy positions of conduction and valence bands of selected semiconducting minerals. *American Mineralogist* **2000**, *85*, 543–556.
23. Bressler, C.; Milne, C.; Pham, V. T.; ElNahhas, A.; van der Veen, R. M.; Gawelda, W.; Johnson, S.; Beaud, P.; Grolimund, D.; Kaiser, M.; Borca, C. N.; Ingold, G.; Abela, R.; Chergui, M., Femtosecond XANES Study of the Light-Induced Spin Crossover Dynamics in an Iron(II) Complex. *Science* **2009**, *323* (5913), 489.
24. Cannizzo, A.; Milne, C. J.; Consani, C.; Gawelda, W.; Bressler, C.; van Mourik, F.; Chergui, M., Light-Induced Spin Crossover in Fe(II)-Based Complexes: The Full Photocycle Unraveled by Ultrafast Optical and X-Ray Spectroscopies. *Coordination Chemistry Reviews* **2010**, *254* (21), 2677-2686.
25. Chen, L. X.; Jager, W. J. H.; Jennings, G.; Gosztola, D. J.; Munkholm, A.; Hessler, J. P., Capturing a Photoexcited Molecular Structure Through Time-Domain X-ray Absorption Fine Structure. *Science* **2001**, *292* (5515), 262-264.
26. Chen, L. X.; Shaw, G. B.; Novozhilova, I.; Liu, T.; Jennings, G.; Attenkofer, K.; Meyer, G. J.; Coppens, P., MLCT State Structure and Dynamics of a Copper(I) Diimine Complex Characterized by Pump-Probe X-ray and Laser Spectroscopies and DFT Calculations. *Journal of the American Chemical Society* **2003**, *125* (23), 7022-7034.
27. Cho, H.; Strader, M. L.; Hong, K.; Jamula, L.; Gullikson, E. M.; Kim, T. K.; de Groot, F. M. F.; McCusker, J. K.; Schoenlein, R. W.; Huse, N., Ligand-Field Symmetry Effects in Fe(ii) Polypyridyl Compounds Probed by Transient X-ray Absorption Spectroscopy. *Faraday Discussions* **2012**, *157* (0), 463-474.
28. Gawelda, W.; Pham, V.-T.; Benfatto, M.; Zaushitsyn, Y.; Kaiser, M.; Grolimund, D.; Johnson, S. L.; Abela, R.; Hauser, A.; Bressler, C.; Chergui, M., Structural

- Determination of a Short-Lived Excited Iron(II) Complex by Picosecond X-Ray Absorption Spectroscopy. *Physical Review Letters* **2007**, 98 (5), 057401.
29. Lockard, J. V.; Rachford, A. A.; Smolentsev, G.; Stickrath, A. B.; Wang, X.; Zhang, X.; Atenkoffer, K.; Jennings, G.; Soldatov, A.; Rheingold, A. L.; Castellano, F. N.; Chen, L. X., Triplet Excited State Distortions in a Pyrazolate Bridged Platinum Dimer Measured by X-ray Transient Absorption Spectroscopy. *The Journal of Physical Chemistry A* **2010**, 114 (48), 12780-12787.
 30. Shelby, M. L.; Mara, M. W.; Chen, L. X., New Insight into Metalloporphyrin Excited State Structures and Axial Ligand Binding from X-ray Transient Absorption Spectroscopic Studies. *Coordination Chemistry Reviews* **2014**, 277–278, 291-299.
 31. Smolentsev, G.; Sundström, V., Time-resolved X-ray Absorption Spectroscopy for the Study of Molecular Systems Relevant for Artificial Photosynthesis. *Coordination Chemistry Reviews* **2015**, 304–305, 117-132.
 32. van der Veen, R. M.; Milne, C. J.; El Nahhas, A.; Lima, F. A.; Pham, V.-T.; Best, J.; Weinstein, J. A.; Borca, C. N.; Abela, R.; Bressler, C.; Chergui, M., Structural Determination of a Photochemically Active Diplatinum Molecule by Time-Resolved EXAFS Spectroscopy. *Angewandte Chemie International Edition* **2009**, 48 (15), 2711-2714.
 33. Chen, L. X., Taking Snapshots of Photoexcited Molecules in Disordered Media by Using Pulsed Synchrotron X-rays. *Angewandte Chemie-International Edition* **2004**, 43 (22), 2886-2905.
 34. Huang, J.; Buyukcakir, O.; Mara, M. W.; Coskun, A.; Dimitrijevic, N. M.; Barin, G.; Kokhan, O.; Stickrath, A. B.; Ruppert, R.; Tiede, D. M.; Stoddart, J. F.; Sauvage, J.-P.; Chen, L. X., Highly Efficient Ultrafast Electron Injection from the Singlet MLCT Excited State of Copper(I) Diimine Complexes to TiO₂ Nanoparticles. *Angewandte Chemie International Edition* **2012**, 51 (51), 12711-12715.
 35. Pattengale, B.; Yang, S.; Ludwig, J.; Huang, Z.; Zhang, X.; Huang, J., Exceptionally Long-Lived Charge Separated State in Zeolitic Imidazolate Framework: Implication for Photocatalytic Applications. *Journal of the American Chemical Society* **2016**, 138 (26), 8072-8075.
 36. Zamponi, F.; Penfold, T. J.; Nachtegaal, M.; Lubcke, A.; Rittmann, J.; Milne, C. J.; Chergui, M.; van Bokhoven, J. A., Probing the Dynamics of Plasmon-Excited Hexanethiol-Capped Gold Nanoparticles by Picosecond X-ray Absorption Spectroscopy. *Physical Chemistry Chemical Physics* **2014**, 16 (42), 23157-23163.
 37. Zhang, X.; Smolentsev, G.; Guo, J.; Attenkofer, K.; Kurtz, C.; Jennings, G.; Lockard, J. V.; Stickrath, A. B.; Chen, L. X., Visualizing Interfacial Charge Transfer in Ru-Dye-Sensitized TiO₂ Nanoparticles Using X-ray Transient Absorption Spectroscopy. *The Journal of Physical Chemistry Letters* **2011**, 2 (6), 628-632.
 38. Hanna, L.; Kucheryavy, P.; Liu, C.; Zhang, X.; Lockard, J. V., Long-Lived Photoinduced Charge Separation in a Trinuclear Iron- μ_3 -oxo-based Metal–Organic Framework. *The Journal of Physical Chemistry C* **2017**, 121 (25), 13570-13576.
 39. Ravel, B.; Newville, M., ATHENA, ARTEMIS, HEPHAESTUS: Data Analysis for X-ray Absorption Spectroscopy Using IFEFFIT. *Journal of Synchrotron Radiation* **2005**, 12 (4), 537-541.

40. Smalley, A. P.; Reid, D. G.; Tan, J. C.; Lloyd, G. O., Alternative synthetic methodology for amide formation in the post-synthetic modification of Ti-MIL125-NH₂. *CrystEngComm* **2013**, *15* (45), 9368-9371.
41. Chen, L. X.; Zhang, X., Photochemical Processes Revealed by X-ray Transient Absorption Spectroscopy. *The Journal of Physical Chemistry Letters* **2013**, *4* (22), 4000-4013.
42. Abedi, S.; Morsali, A., Improved photocatalytic activity in a surfactant-assisted synthesized Ti-containing MOF photocatalyst under blue LED irradiation. *New Journal of Chemistry* **2015**, *39* (2), 931-937.
43. Dan-Hardi, M.; Serre, C.; Frot, T.; Rozes, L.; Maurin, G.; Sanchez, C.; Férey, G., A New Photoactive Crystalline Highly Porous Titanium(IV) Dicarboxylate. *Journal of the American Chemical Society* **2009**, *131* (31), 10857-10859.
44. Nasalevich, M. A.; Hendon, C. H.; Santaclara, J. G.; Svane, K.; van der Linden, B.; Veber, S. L.; Fedin, M. V.; Houtepen, A. J.; van der Veen, M. A.; Kapteijn, F.; Walsh, A.; Gascon, J., Electronic origins of photocatalytic activity in d0 metal organic frameworks. *Sci Rep* **2016**, *6*, 23676.
45. Boubnov, A.; Roppertz, A.; Kundrat, M. D.; Mangold, S.; Reznik, B.; Jacob, C. R.; Kureti, S.; Grunwaldt, J.-D., Towards advanced structural analysis of iron oxide clusters on the surface of γ -Al₂O₃ using EXAFS. *Applied Surface Science* **2016**, *386*, 234-246.
46. Carroll, K.; Hudgins, D.; Spurgeon, S.; Kemner, K.; Mishra, B.; Boyanov, M.; Brown, L.; Taheri, M.; Carpenter, E., One-Pot Aqueous Synthesis of Fe and Ag Core/Shell Nanoparticles. *Chemistry of Materials* **2010**, *22*, 6291-6296.
47. Tanwar, K. S.; Petitto, S. C.; Ghose, S. K.; Eng, P. J.; Trainor, T. P., Fe(II) adsorption on hematite (0001). *Geochimica et Cosmochimica Acta* **2009**, *73* (15), 4346-4365.
48. Naicker, P. K.; Cummings, P. T.; Zhang, H.; Banfield, J. F., Characterization of Titanium Dioxide Nanoparticles Using Molecular Dynamics Simulations. *The Journal of Physical Chemistry B* **2005**, *109* (32), 15243-15249.
49. Grunes, L. A., Study of the K edges of 3d transition metals in pure and oxide form by x-ray-absorption spectroscopy. *Physical Review B* **1983**, *27* (4), 2111-2131.
50. Zhang, F.; Zhang, B.; Feng, J.; Tan, X.; Liu, L.; Liu, L.; Han, B.; Zheng, L.; Zhang, J.; Tai, J.; Zhang, J., Highly Mesoporous Ru-MIL-125-NH₂ Produced by Supercritical Fluid for Efficient Photocatalytic Hydrogen Production. *ACS Applied Energy Materials* **2019**, *2* (7), 4964-4970.